이학박사 학위논문

구조제어된 반도체 나노재료의 제조 및 특성평가와

응용성에 대한 연구

Preparation, Characterization, and Application of Structure-Controlled

Semiconductor Nanomaterials

2013 년 2 월

서울대학교 대학원

화학부 물리화학 전공

김 종 엽

A Ph. D. Dissertation

Preparation, Characterization, and Application of Structure-Controlled

Semiconductor Nanomaterials

By Jong-Yeob Kim

Supervisor: Professor Du-Jeon Jang

Major: Physical Chemistry

School of Chemistry

Graduate School of Seoul National University

January 2013

Abstract of Dissertation

ZnSe·N$_2$H$_4$ or ZnO one-demensional nanostructures having unique opical properties and TiO$_2$ nanopopcorns having photocatalytic and photovoltaic properties as well as CdTe@CdS@ZnS quantum dots have been synthesized hydrothermally and their structural and optical properties have also characterized by analyzing electron microscopic images, electron diffraction patterns, and UV/vis absorption, photoluminescence, X-ray photoelectron, and Raman spectra. The optical properties and fabrication methods of the nanomaterials are dealt with in Chapter 1. Substantial efforts have been devoted to the preparation of nanoparticles, having unique optical properties controlled by the morphology and composition of nanoparticles, to make them potential candidates successfully for application in UV lasers, photocatalytic devices, and solar cells.

Chapter 2 reports a hydrazine-hydrate-assisted hydrothermal process to synthesize the inorganic-organic hybrid nanobelts of the hexagonal wurtzite ZnSe·N$_2$H$_4$. Although the preparation of ZnSe·(diethylenetriamine)$_{0.5}$ hybrid nanobelts and the synthesis of ZnSe·N$_2$H$_4$ microrods were reported, the synthesis of ZnSe·N$_2$H$_4$ hybrid nanobelts has not been reported yet. Length-to-width and width-to-thickness ratios of ZnSe·N$_2$H$_4$ nanobelts have been well controlled by adjusting [Se]-to-[ZnCl$_2$] ratios as well as reaction time and temperature. The mean lifetime of photoluminescence kinetics having three decay components of 18 ps, 85 ps, and 1300 ps increases concomitantly with the length-to-width ratio of the ZnSe·N$_2$H$_4$ nanobelt structure.

In Chapter 3, well-ordered arrays of hexagonal wurtzite ZnO nanowires have been faciley grown directly on Zn foil and employed for room temperature UV nanolasers. It has not been reported that arrayed 1D ZnO nanowires are synthesized hydrothermally on Zn foil for the direct application in UV laser. The UV lasing action of arrayed ZnO Nanowires was observed at 370–400 nm with I_{th} of 25 kW cm^{-2}, which was much lower than reported values for ZnO nanorod arrays. Photoluminescence decays biexponentially: the fast component is attributed to free-exciton decay, and the slow one is to bound-exciton decay. The amplitude of the fast component increases whereas its lifetime decreases with the increment of I_{ex}, suggesting that ZnO nanowire arrays undergo a change in the lasing mechanism from exciton–exciton scattering to electron–hole plasma recombination.

Chapter 4 presents that tetragonal anatase TiO$_2$ nanopopcorns have been facilely grown on Ti foil via a hydrothermal method to be employed for photocatalytic and photovoltaic materials directly without being treated via any annealing process. Although anatase TiO$_2$ nanocrystals with being treated via a high-temperature post-annealing process have been employed as photocatalytic or photovoltaic materials, the hydrothermal synthesis of anatase TiO$_2$ nanostructures on Ti foil without being treated via any post-annealing process has been hardly reported yet. In addition, the direct photocatalytic and photovoltaic applications of anatase TiO$_2$ nanopopcorns on Ti foil have not been reported although ZnO nanowires grown on FTO glass or TiO$_2$ nanowires grown on Ti foil have been utilized in DSSCs. The morphology of TiO$_2$ nanostructures on Ti foil has been controlled well by adjusting the volume ratio of H$_2$O$_2$: HF: H$_2$O, VR(H$_2$O$_2$:HF:H$_2$O). TiO$_2$ nanopopcorns grown at

VR(H_2O_2:HF:H_2O) of 1:1:1000 have the best-defined –Ti–O– network of the tetragonal anatase TiO_2 structure with a minimal amount of trap sites and oxygen vacancies. The enhanced photocatalytic activity of our anatase TiO_2 nanopopcorns grown at VR(H_2O_2:HF:H_2O) of 1:1:1000 arises from their 3D hierarchical nanostructures and exposed {001} facets. The highest power conversion efficiency of 3.98% using TiO_2 nanopopcorns grown on Ti foil at VR(H_2O_2:HF:H_2O) of 1:1:1000 as the working electrode of DSSC results from their largest surface area to absorb dye molecules and their best-defined anatase crystallinity to reduce recombination losses.

In Chapter 5, Core-shell-shell quantum dots (QDs) of CdTe/CdS/ZnS having an average diameter of 4.2 nm and exhibiting type-II behaviors have been facilely synthesized in water by injecting Zn^{2+}(aq) simply into an aqueous colloidal solution of CdTe/CdS core-shell QDs having an average diameter of 3.8 nm. We have introduced a CdS inner shell, whose lattice constant is between those of CdTe and ZnS, between the CdTe core and the ZnS outer shell to reduce strain inside a nanocrystal considerably. The optical properties of CdTe/CdS/ZnS QDs have been controlled by adjusting reaction time as well as pH, reaction temperature, and Zn^{2+} amount. The photoluminescence quantum yield of the aqueous colloidal solution of CdTe/CdS/ZnS core-shell-shell QDs has been found to be as large as 15% whereas that of CdTe/CdS core-shell QDs has been observed as 4%.

Keywords: Core-shell-shell, Hydrothermal, Nanobelts, Nanolasers, Nanowires, Photoluminescence, Quantum dots, Solovothermal, Time-resolved spectroscopy

Student Number: 2006-20364

Table of Contents

Appendices

A. Preferentially Linear Connection of Gold Nanoparticles in Derivatization with
   Phosphorothioate Oligonucleotides

B. Electrophoretic Separation of Gold Nanoparticles According to Bifunctional
   Molecules-Induced Charge and Size

List of Figures and Tables

Figure 1-9 Sol-gel processing to make nanostructured layers and coatings as well as nanoporous membranes.

Figure 1-10 Reaction of gases in the reaction chamber causes deposition of the reaction product as a layer that can be of nano thickness.

Figure 2-1 TEM (left) and SEM images (right) of ZnSe·N_2H_4 nanobelts grown at 180 $^{\circ}$C for 6 h using [Se]-to-[$ZnCl_2$] ratios of 2.3 (a), 1.0 (b), and 0.43 (c). Each scale bar indicates 500 nm.

Figure 2-2 TEM images of ZnSe·N_2H_4 nanobelts grown at 180 °C for 6 h using [Se]-to-[$ZnCl_2$] ratios of 1.5 (a) and 0.67 (b). Each scale bar indicates 500 nm.

Figure 2-3 HRXRD patterns of ZnSe·N_2H_4 nanobelts grown at 180 $^{\circ}$C for 6 h. The employed ratios of [Se]-to-[$ZnCl_2$] are indicated inside.

Figure 2-4 HRTEM image (a), showing lattice plane distances, and FFT pattern (b), showing lattice planes, of a hexagonal wurtzite ZnSe·N_2H_4 nanobelt grown at 180 $^{\circ}$C for 6 h with a [Se]-to-[$ZnCl_2$] ratio of 1.0.

Figure 2-5 Survey (a), Se $3d_{5/2}$ (b), Zn $2p_{5/2}$ (c), Zn 3p (d), Zn LMM (e), and N 1s (f) XPS spectra of ZnSe·N_2H_4 nanobelts grown at 180 $^{\circ}$C for 6 h with a [Se]-to-[$ZnCl_2$] ratio of 1.0.

Figure 2-6 Maximum-normalized photoluminescence spectra of ZnSe·N_2H_4 nanobelts grown at 180 $^{\circ}$C for 6 h with [Se]-to-[$ZnCl_2$] ratios of 0.43 (black), 1.0 (green), and 2.3 (red). Nanobelts were suspended in water and excited at 266 nm.

Figure 2-7 Maximum-normalized photoluminescence decay kinetic profiles, monitored at 400 nm after excitation at 266 nm, of ZnSe·N$_2$H$_4$ nanobelts grown at 180 $^{\circ}$C for 6 h with [Se]-to-[ZnCl$_2$] ratios of 0.43 (black), 1.0 (green), and 2.3 (red) and suspended in water.

Figure 2-8 TEM (left) and SEM images (right) of ZnSe·N$_2$H$_4$ nanobelts grown at 180 $^{\circ}$C for 0.5 h (a), 1.5 h (b), 3.0 h (c), and 6.0 h (d) with a [Se]-to-[ZnCl$_2$] ratio of 1.0. Each scale bar indicates 500 nm.

Figure 2-9 TEM images and SAED patterns (insets) of ZnSe·N$_2$H$_4$ nanobelts grown for 6 h at 100 °C (a), 140 °C (b), and 180 °C (c) with a [Se]-to-[ZnCl$_2$] ratio of 1.0. Each scale bar indicates 200 nm.

Table 2-1 Spectral Data and Decay Kinetic Constants of ZnSe·N$_2$H$_4$ Photoluminescence[a]

Figure 3-1 (a) SEM image of arrayed ZnO nanowires on Zn foil. (b) TEM image, (c) HRTEM image, showing the most preferred growth orientation and a lattice plane distance, and (d) FFT pattern, showing lattice planes, of a hexagonal wurtzite ZnO nanowire.

Figure 3-2 EDX profile of a ZnO nanowire grown on Zn foil.

Figure 3-3 Raman spectrum of ordered ZnO nanowire arrays grown on Zn foil.

Figure 3-4 SEM images of ZnO nanostructures grown on Zn foil at 180 °C for (a) 1 h, (b) 2 h, (c) 3 h, and (d) 6 h. Each scale bar indicates 1 μm.

Figure 3-5 SEM images of ZnO nanostructures grown on Zn foil at 180 °C for 6 h using V(H_2O)/ V($N_2H_4 \cdot H_2O$) ratios of (a) 0.25, (b) 0.5, (c) 1.0, and (d) 2.0. Each scale bar indicates 1 μm.

Figure 3-6 HRXRD pattern of (black) ordered ZnO nanowire arrays grown on Zn foil, (red) reference hexagonal wurtzite ZnO, and (green) reference hexagonal Zn.

Figure 3-7 (a) Survey, (b) O 1s, (c) Zn $2p_{3/2}$, and (d) Zn LMM XPS spectra of ordered ZnO nanowire arrays grown on Zn foil.

Figure 3-8 (blue) Absorption and (red) photoluminescence (with excitation at 266 nm) spectra of ordered ZnO nanowire arrays grown on Zn foil.

Figure 3-9 Photoluminescence spectra of (red) ordered ZnO nanowire arrays on Zn foil and (green) bare Zn foil, with excitation at 266 nm.

Figure 3-10 (a) I_{ex}–dependent photoluminescence spectra, excited at 266 nm and dispersed with a grating of 150 grooves mm^{-1}, of ordered ZnO nanowire arrays grown on Zn foil. Excitation irradiances are indicated inside in units of kW cm^{-2}. The fitted solid line of the inset shows that photoluminescence increases nonlinearly above I_{th} of 25 kW cm^{-2}. (b) Photoluminescence spectrum, excited at 266 nm and dispersed with a grating of 1200 grooves mm^{-1}, of ordered ZnO nanowire arrays grown on Zn foil at I_{ex} of 100 kW cm^{-2}.

Figure 3-11 Maximum-normalized I_{ex}–dependent photoluminescence decay kinetic profiles monitored at 380 nm after excitation at 266 nm, of ordered ZnO nanowire arrays grown on Zn foil.

Table 3-1 Photoluminescence decay kinetic constants of ordered ZnO nanowire arrays on Zn foil.

Figure 4-1 (a) TEM image of TiO_2 nanopopcorns. (b) HRTEM image, showing a lattice-plane distance, and (c) SAED pattern, with indication of a (101) lattice plane, of an anatase TiO_2 nanopopcorn.

Figure 4-2 SEM images of TiO_2 nanopopcorns grown on Ti foil with VR(H_2O_2:HF:H_2O) of (a) 1:0.5:1000, (b) 1:1:1000, (c) 1:2.5:1000, and (d) 1:5:1000. Each scale bar indicates 500 nm.

Figure 4-3 SEM images of TiO_2 nanopopcorns grown on Ti foil with VR(H_2O_2:HF:H_2O) of (a) 0.5:1:1000, (b) 1:1:1000, (c) 2.5:1:1000, and (d) 5:1:1000. Each scale bar indicates 500 nm.

Figure 4-4 HRXRD patterns of TiO_2 nanopopcorns grown on Ti foil with VR(H_2O_2:HF:H_2O) of (a) 1:0.5:1000, (b) 1:1:1000, (c) 1:2.5:1000, and (d) 1:5:1000. The standard diffraction lines of anatase TiO_2 and rutile TiO_2 are also shown for comparison.

Figure 4-5 XRD patterns of TiO_2 nanopopcorns grown on Ti foil at VR(H_2O_2:HF:H_2O) of (a) 0.5:1:1000, (b) 1:1:1000, (c) 1:2.5:1000, and (d) 5:1:1000. The standard diffraction lines of anatase TiO_2 and rutile TiO_2 are also shown for comparison.

Figure 4-6 Raman spectra of TiO_2 nanopopcorns grown on Ti foil with $VR(H_2O_2:HF:H_2O)$ of (a) 1:0.5:1000, (b) 1:1:1000, (c) 1:2.5:1000, and (d) 1:5:1000.

Figure 4-7 XPS spectra of the O1s of TiO_2 nanopopcorns grown on Ti foil with $VR(H_2O_2:HF:H_2O)$ of (a) 1:0.5:1000, (b) 1:1:1000, (c) 1:2.5:1000, and (d) 1:5:1000.

Figure 4-8 Maximum-normalized photoluminescence spectra of TiO_2 nanopopcorns grown on Ti foil with $VR(H_2O_2:HF:H_2O)$ of (a) 1:1:1000, (b) 1:2.5:1000, and (c) 2.5:1:1000. Samples were suspended in water and excited at 266 nm.

Figure 4-9 Photoluminescence spectra of TiO_2 nanopopcorns grown on Ti foil. $VR(H_2O_2:HF:H_2O)$ were (*blue*) 1:1:1000, (*green*) 1:2.5:1000, (*red*) 2.5:1:1000, and samples were suspended in water and excited at 266 nm.

Figure 4-10 Pseudo-first-order kinetic rate plots for the photocatalytic degradation of MB (360 ppm) at different concentraions of TiO_2 nanopopcorns grown at $VR(H_2O_2:HF:H_2O)$ of 1:1:1000 on Ti foil. The suspended masses of nanopopcorns in 2 mL of water were (squares) 0.0, (circles) 1.2, (diamonds) 2.4, and (triangles) 4.8 mg. The rate constants obtained from the best-fitted lines with the nanopopcorns of 0.0, 1.2, 2.4, and 4.8 mg are 0.11, 0.96, 1.8, and 3.0 h^{-1}, respectively.

Figure 4-11 (a) Photocatalytic degradation kinetic profiles of MB (360 ppm) in 2 mL water in the (open) absence and (closed) presence of 4.8 mg TiO_2 nanopopcorns grown at $VR(H_2O_2:HF:H_2O)$ of (triangles) 1:1:1000, (diamonds) 1:2.5:1000, and (circles) 2.5:1:1000

and (b) their pseudo-first-order kinetic rate plots. The rate constants obtained from the best-fitted lines of squares, circles, diamonds, and triangles are 0.11, 0.66, 1.3, and 3.0 h^{-1}, respectively.

Figure 4-12 Current density-voltage characteristics of DSSCs based on TiO_2 nanopopcorns grown on Ti foil atVR(H_2O_2:HF:H_2O) of (a) 1:1:1000, (b) 1:2.5:1000, and (c) 2.5:1:1000.

Table 4-1 Photovoltaic operation parameters of DSSCs produced with anatase TiO_2 nanopopcorns grown on Ti foil electrodes grown at variation of VR(H_2O_2:HF:H_2O)

Scheme 5-1 Schematic representation of the energy-level alignment of a bulk CdTe/CdS/ZnS core-shell-shell system.

Figure 5-1 HRTEM images (a,b) and SAED pattern (c) of CdTe/CdS/ZnS core-shell-shell QDs grown for 6 h with V_{Zn} of 60 at pH 10.6 and 100 $^{\circ}$C.

Figure 5-2 HRTEM images (a,b) and SAED pattern (c) of CdTe/CdS QDs grown at pH 9.0 and 100 $^{\circ}$C.

Figure 5-3 EDX profiles of CdTe/CdS/ZnS core-shell-shell QDs grown with V_{Zn} of 0 (a) and 60 (b) at pH 10.6 and 100 $^{\circ}$C. The molar ratios of Cd/Te/S/Zn were found to be 2.1/1.0/1.3/0.0 in the profile *a* and 1.8/1.0/2.1/2.2 in the profile *b*.

Figure 5-4 HRXRD patterns of CdTe/CdS/ZnS core-shell-shell QDs grown with V_{Zn} of 0 (black), 30 (red), 60 (green), and 90 (blue) at pH 10.6 and 100 $^{\circ}$C. The standard diffraction lines of cubic CdTe, cubic CdS, and cubic ZnS are also shown for comparison.

Figure 5-5 XPS spectra of CdTe/CdS/ZnS core-shell-shell QDs grown with V_{Zn} of 0 (black), 30 (red) and 60 (green) at pH 10.6 and 100 $^{\circ}$C.

Figure 5-6 Absorption spectra of the aqueous colloidal solutions of CdTe/CdS/ZnS core-shell-shell QDs grown with V_{Zn} of 60 at pH 10.6 and 100 $^{\circ}$C for indicated reaction times in units of min.

Figure 5-7 Maximum-normalized photoluminescence spectra of the aqueous colloidal solutions of CdTe/CdS/ZnS core-shell-shell QDs grown with V_{Zn} of 60 at pH 10.6 and 100 $^{\circ}$C for indicated reaction times in units of min.

Figure 5-8 Photoluminescence spectra of the aqueous colloidal solutions of CdTe/CdS/ZnS core-shell-shell QDs grown with V_{Zn} of 60 for indicated reaction times in units of min at pH 10.6 and 100 $^{\circ}$C.

Figure 5-9 Absorption spectra (a) and photoluminescence spectra (b) of the aqueous colloidal solutions of CdTe/CdS/ZnS core-shell-shell QDs grown for 6 h with indicated V_{Zn} at pH 10.6 and 100 $^{\circ}$C.

Figure 5-10 Extinction spectra (a) and photoluminescence spectra (b) of the aqueous colloidal solutions of CdTe/CdS/ZnS core-shell-shell QDs grown for 6 h with V_{Zn} of 60 at 100 $^{\circ}$C and indicated pHs.

Figure 5-11 Photoluminescence spectra of the aqueous colloidal solutions of CdTe/CdS/ZnS core-shell-shell QDs grown for 6 h with V_{Zn} of 60 at pH 10.6 and indicated temperatures in units of $^{\circ}$C.

Figure 5-12 Absorption spectra (a) and photoluminescence spectra (b) of the aqueous colloidal solutions of CdTe/CdS/ZnS core-shell-shell QDs grown for 6 h with V_{Zn} of 60 at 100 $^{\circ}$C and indicated pHs.

Chapter 1. General Introduction

1.1 Abstract

Optical properties and preparation methods of nanoparticles are described briefly. The effect of the size and the shape on the optical properties of a semiconductor nanocrystal is very interesting. In order to understand the size-dependent optical properties of semiconductor nanoparticles, it is important to know the physics behind, taking place at the nano level. The optical properties of metal nanoparticles have also been of interest in physical chemistry, starting with Faraday's investigations of gold colloid. Compared with bulk metals, Colloidal nanoparticles of noble metals exhibit characteristic optical and physical properties. For applications of these semiconductor and metal nanoparticles, a variety of preparation methods have been expanded continuously. Considerable efforts have been devoted to the fabrication of the nanoparticles to make them potential candidates successfully for diverse applications.

1.2 Optical Properties of Nanostructured Materials

The spectroscopic, electronic, and chemical properties of nanomaterials are of great interest in both basic and applied researches.[1] In the case of semiconductor bulk materials, if an incident photon has energy greater than the band gap of the material, an electron may be excited from the valence band to the unfilled conduction band. The photon is absorbed while a hole is left in the valence band when the electron jumps to the conduction band (Figure 1-1). If an electron in the conduction band returns to the valence band and recombines with a hole, a photon is released with energy equal to the band gap of the semiconductor (Figure 1-2). Also, semiconductor nanoscaled materials have been studied both experimentally and theoretically.[2,3] The binding between the electron and the hole arises from the differe nce in electrical charge between the electron (negative) and the hole (positive), leading to a
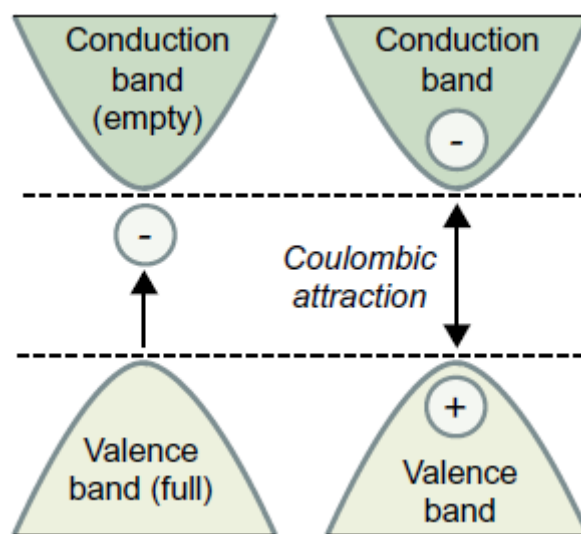
Figure 1-1 Schematic representation of an electron and a hole in the band-gap of a bulk semiconductor material.

Coulombic attractive force across the two particles, which can be written as:[4]

$$F_C = \frac{-e^2}{4\pi\varepsilon_0 r^2} \tag{1}$$

where e is the electron charge, ε_0 is the dielectric constant of free space and r is the separation distance between the electron and the hole. This electrostatic interaction reduces the energy required for exciton formation, with respect to the unbound electron and hole energy, bringing the energy levels closer to the conduction band. Optical emission may also occur if the electron and the hole recombine, leading to the generation of a photon. The emission of visible light that is can be tuned by varying the nanoscale dimensions because of the quantum confinement in nanomaterials.[5] The exciton radius has nanoscale dimensions. Therefore, for a nanomaterial, the exciton radius may be confined. The effects of nanoscale on optical absorption are associated with the density of states in the valence and conduction band, the quantized energy levels of thenanostructure, and the influence of excitonic effects. As the nanomaterial changes from 3-D to 0-D and quantum confinement is more severe, the density
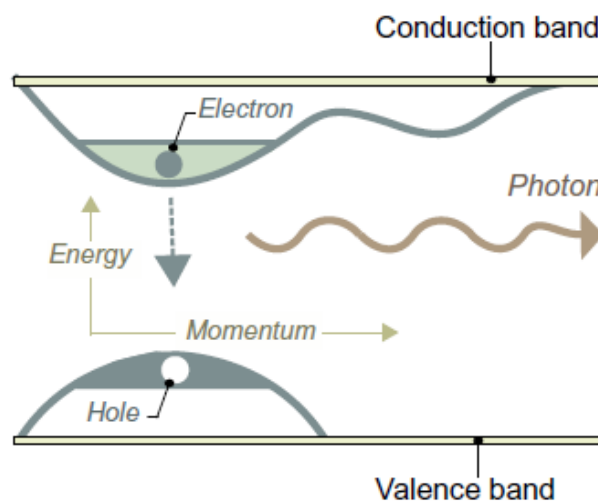
Figure 1-2 Emission of a photon upon recombination of an electron-hole pair.

of states becomes more quantized and the band gap of the material shifts toward higher energies. A blue shift is expected in the absorption spectrum as the size of the nanomaterial decreases, whereas a red shift occurs for an increase in size. Figure 1-3 shows the size tunability of the interband absorption spectra of PbSe nanocrystals.[6] The interband features are sharp enough to show not only the first, but the second and often the third exciton features. The first exciton peaks, which are quite narrow indicative of a size distribution of a nanoparticle, at 0.587, 0.688, and 0.865 eV have determined the average diameters of 8.1, 7.1, and 5.8 nm, respectively. The confinement energies are then extracted by subtracting the band gap energy taken at the appropriate temperature.[7] The highest energy absorption region, called the absorption edge, is shifted toward the blue as the confinement dimension is reduced. The higher absorbance peaks shown in Figure 1-3 are associated with the formation of excitons, which shift to higher energies with the decreasing of the size of a nanocrystal.
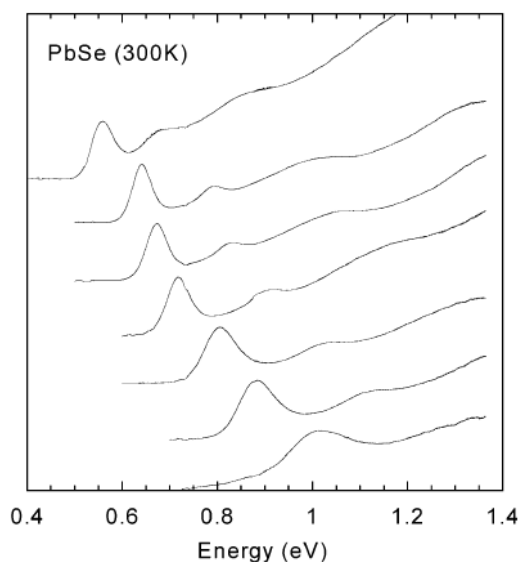
Figure 1-3 Absorption spectra of PbSe quantum dot samples of different sizes. Samples are at room temperature in chloroform solvent.

A higher degree of confinement leads to an increase of the exciton binding energy, which should be visible in the absorption spectrum. When the dimensions of the nanomaterial are smaller than the exciton radius, the electron and hole wave functions are uncorrelated and thus their motion becomes independent.[8] Strong excitonic states appear in the absorption spectra of nanomaterials at room temperature. The typical trend is the shift of the emission peak toward shorter wavelengths as the size of the nanocrystal decreases. Figure 1-4 shows the photoluminescence spectra of CdSe-ZnS quantum dots with different sizes.[9] The smaller the size of the quantum dot, the shorter the wavelength of the maximum-normalized photoluminescence spectra.
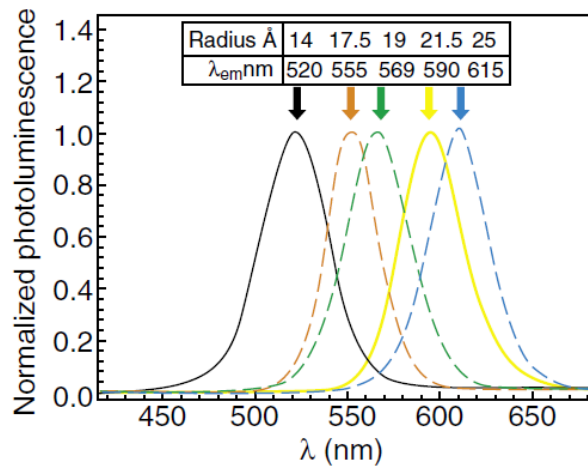
Figure 1-4 Maximum-normalized photoluminescence spectra of CdSe-ZnS quantum dots with different sizes of the quantum dots.

Figure 1-5 shows the absorption spectra and photoluminescence spectra under a 365 nm excitation wavelength of the three different core-shell samples. Quantum yields of the green-, yellow-, and red-emitting CdSe@ZnS QDs are 64.2%, 47.7%, and 28.3% with PL λmax of 524, 574, and 619 nm, respectively.[10] Figure 1-6 shows three monolith samples with different emission wavelengths under a room light (top) or a UV light (bottom).[10] The

samples were transparent without apparent inhomogeneity in color and showed strong photoluminescence emissions. Figure 1-5 shows the photoluminescence effect of CdSe nanoparticles of various sizes, which covers the entire visible spectrum. Due to quantum confinement, the shift from the blue to the red shown in Figure 1-5 corresponds to an increase in nanoparticle size. In this regard, an issue of importance is the use of a homogeneous distribution of nanoparticles, because fluctuations in size and composition can lead to an inhomogeneous spreading of the optical spectra.
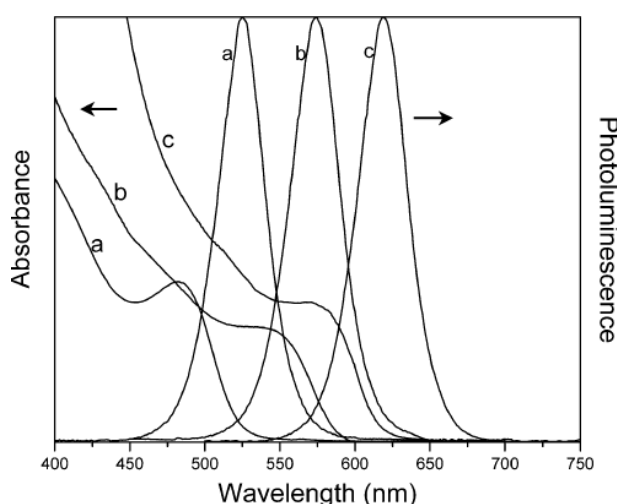
Figure 1-5 Absorption and photoluminescence spectra of the MPS-capped CdSe@ZnS quantum dots in methanol. The core particles for the samples a-c were prepared at 70, 120, and 190 °C, respectively. A 365 nm UV light was used for the excitation of the samples.

Figure 1-6 Silica monoliths embedded with the three different CdSe@ZnS QD products under a room light (top) and a 365 nm UV light (bottom).

16

Luminescent colloidal semiconductors attract considerable attention because they can be employed for the development of fluorescent dyes, light-emitted diodes, and solar cells.[11] Core–shell or core– shel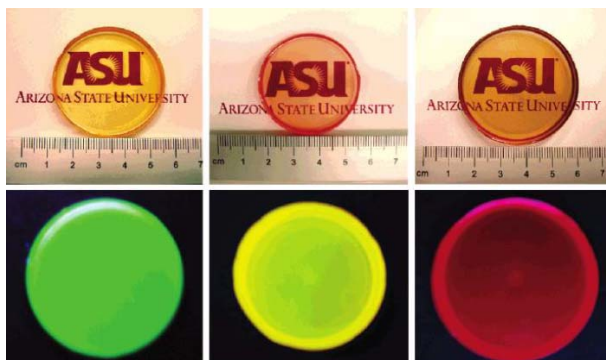l–shell QDs are known to exhibit unique physical and chemical properties distinctly different from those of individual componentsIn core–shell QDs of type-II structures, such as ZnSe/CdS, CdTe/CdSe, and CdSe/CdTe, the shell material having a wider band-gap is grown onto the core material to reduce the nonradiative recombination effectively by confining the wave function of an electron–hole pair to the interior of the core material.[12] The absorption spectrum of the QDs shifts to the longer wavelength and their band-gap energy decreases with shell thickness. Also, Inorganic–organic hybrid nanocomposites receive much attention because of their tremendous potential in providing enhanced material properties that are not easily achievable with either organic or inorganic materials alone.[13] These nanomaterials exhibit significantly enhanced electronic and optical properties including band-gap tunability and high band-edge absorption.[14] Hybrid nanocomposite materials also have additional advantage of perfectly ordered crystal structures, thus allowing high carrier mobility. In addition, one-dimensional nanostructured arrays of GaN, ZnSe, ZnS, and ZnO have attracted considerable interest in applications to ultraviolet laser devices due to their wide direct band-gaps. Substantial efforts have been devoted to the fabrication of high-quality 1D ZnO nanowire arrays to make them promising candidates for applications in UV lasers, light-emitting diodes, solar cells, photocatalytic devices, and field-emission displays.

The optical properties of metallic nanomaterials are also affected by nanosize.[15] Gold

has a yellowish color in bulk whereas a gold colloidal solution has a ruby-red, purple, or even blue color, depending on the gold nanoparticle size. Plasmons are quantized waves propagating in materials through a collection of mobile electrons that are generated when a large number of these electrons are altered from their equilibrium positions. Surface plasmons have lower frequencies than bulk plasmons and thus can interact with photons.[16] In other words, surface-plasmon resonances are essentially light waves that are trapped on the surface of the material, as a result of interactions between the incident wave and the existing free electrons.

A necessary condition for localized surface plasmons to exist is that the wavelength of the incident light must be larger than the size of the nanoparticle.[17] The electric field of the incident light can induce an electric dipole in the metallic nanoparticle. The wavelength of light required to induce the generation of localized surface plasmons depends on the size of the nanoparticle as well as shape and composition. Typically, as the particle size decreases, the plasmon resonance frequency increases, leading to a blue shift in the spectrum. By tuning the size, different colors can be achieved. Nanoparticles with different shapes are required although nonspherical geometries are much more difficult to attain. For a 1-D nanomaterial, there is a longitudinal plasmon along the long axis, whereas transverse plasmons exist across the diameter of the material. In the case of 0-D nanomaterials, the production of well-defined nonspherical shapes is usually quite challenging but of great interest. Another optical plasmon effect associated with metallic nanoparticles occurs when agglomeration takes place. Under these conditions, a shift toward lower plasmon frequencies occurs, leading to a red shift.

1.3 Facile Syntheses and Applications of Nanopaticles

Many processes of producing nanoscaled materials and structures have been investigated extensively. Diverse methods such as inert-gas condensation, sonochemical processing, sol-gel deposition, molecular self-assembly, electrodeposition, chemical vapor deposition, and hydrothermal synthesis have been establisched to synthesize nanostructures successfully.[5,14] In inert-gas condensation (Figure 1-7), inorganic materiasl are vaporized inside a vacuum chamber into which Ar(g) or He(g) are periodically admitted.[18] The source of vapor can be an evaporation boat, a sputtering target, or a laser-ablation target. Once the atoms boil off, they quickly lose their energy by colliding with the inert gas. The vapor cools rapidly and supersaturates to form nanoparticles with sizes in the range 2–100 nm. The main problem with this method is that as the particles form, they tend to cluster and increase their size, defeating the original objective.
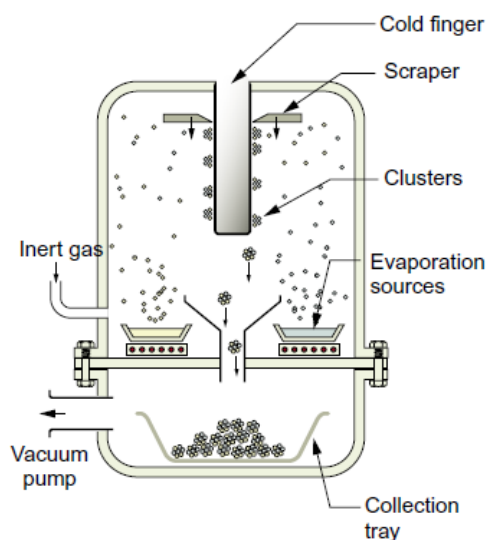
Figure 1-7 The nanoclusters that form on the cold finger are harvested by the scraper and collector and subsequently consolidated to make products.

Ultrasound spans the frequencies in the range 15 kHz to 1 GHz. A magnetostrictive or piezoelectric transducer is used to generate ultrasonic waves with a wavelength of 1–10,000 microns in a liquid-filled reaction vessel (Figure 1-8). These are not molecular dimensions, so there is no direct coupling of the acoustic field with the chemical species.[19] The tensile part of the wave is intense enough to pull the liquid apart and form a tiny cavity. The next tensile wave re-expands the bubble, which oscillates in volume at the frequency of the sound waves, pumping it up as more vapor enters during the expansion part of the cycle. When the bubble reaches a critical size, it collapses.[20] The collapse is adiabatic because the very fast collapse rate leaves no time for heat flow, generating a tiny, localized hot spot. The temperatures are very high (about 5000°C) and so too are the pressures (around 2000 atmospheres), triggering reactions that create a nanoparticle within the spot. The technique can be used to produce a large volume of material for industrial applications.
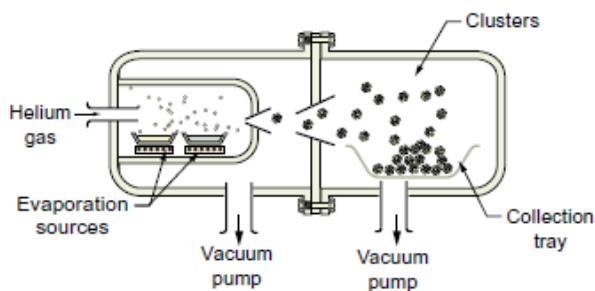
Figure 1-8 Cluster formation by vapor phase expansion from an oven source.

Ultrafine particles, nanothickness films, and nanoporous membranes can be made by sol-gel processing (Figure 1-9). The starting point is a solution of precursors in an appropriate solvent. The precursors are usually inorganic metal salts or metal-organic compounds such as alkoxides-metal ions with an organic ligand such as Ti $(OC_4H_9)_4$. The precursor is subjected

to a polymerization reaction to form a colloidal suspension of discrete, finely dispersed particles kept in suspension by adding a surfactant.[21] The suspension can be treated to extract the particles for further processing, or it can be cast or spin-coated onto a substrate. There it is converted to a gel by chemical treatment to disable the surfactant to create an extended network of connected particles throughout the solution, making a kind of superpolymer, one enormous molecule in the form of an open 3-D network.
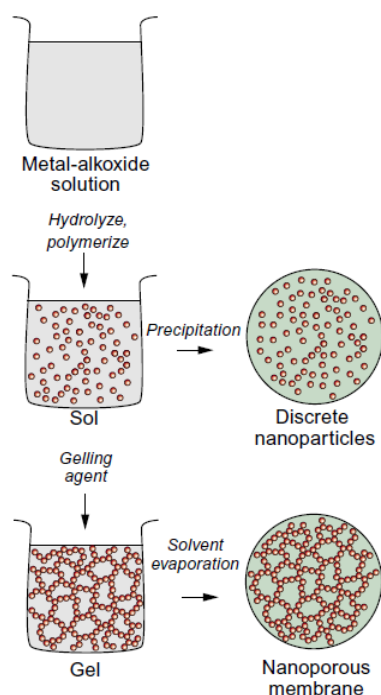
Figure 1-9 Sol-gel processing to make nanostructured layers and coatings as well as nanoporous membranes.

Molecular self-assembly methods rely on the self-organization of organic molecules. The most remarkable of all is the self-assembly of DNA that passes genetic information from cell to cell, instructing them how to self-assemble.[22] The idea is to create the conditions under which atoms or molecules will selfassemble into useful structures, driven by the minimization of their energy. Typically, the aggregates formed by self-assembly tend to be

bonded by relatively weak bonds with binding energies only a few times larger than kT, the thermal energy per atom.

Electrodeposition is a long-established way to deposit metal layers on a conducting substrate.[23] Ions in solution are deposited onto the negatively charged cathode, carrying charge at a rate that is measured as a current in the external circuit. The layer thickness simply depends on the current density and the time for which the current flows. The deposit can be detached if the substrate is chosen to be soluble by dissolving it away. Most electrodeposits grow in a columnar manner: metal crystals nucleate on the bare substrate when the current is switched on and grow outward as interlocking pillars. To make nanoparticles or layers, it is necessary is to stop each crystal's growth while it is still tiny and to nucleate more. For example, ZnO nanowire arrays have been electrodeposited in a single step on ordered anodic alumina membranes.[24]

In chemical vapor deposition processing, a reactant gas mixture is brought into contact with the surfaces to be coated, where it decomposes, depositing a dense pure layer of a metal or compound (Figure 1-10).[17] The deposit can be formed by a reaction between precursor gases in the vapor phase or by a reaction between a vapor and the surface of the substrate itself. A difficulty with the process is that it frequently requires high temperatures, 800°C or more. When the chemical reactions in the vapor phase are activated by the creation of plasma in the gas phase or by shining a laser beam into the gas mixture, deposition at an even lower temperature becomes possible. Coatings formed with CVD methods are typically nanocrystalline or amorphous because their formation is no longer dependent on equilibrium

22

thermodynamic constraints.
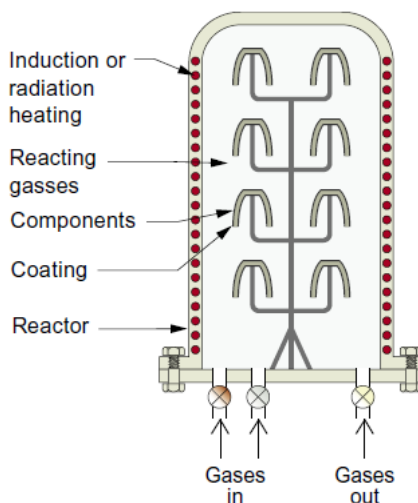
Figure 1-10 Reaction of gases in the reaction chamber causes deposition of the reaction product as a layer that can be of nano thickness.

Hydrothermal syntheses of nanostructures have been found to be quite advantageous particularly from viewpoints of environmental friendliness, easy upward scaling, and low production cost.[25] Hydrothermal synthesis can be defined as a method of synthesis of single crystals that depends on the solubility of minerals in hot water under high pressure.[26] The crystal growth is performed in an apparatus consisting of a steel pressure vessel called a Teflon-lined stainless-steel autoclave, in which a precursor is supplied along with water. A gradient of temperature is maintained at the opposite ends of the growth chamber so that the hotter end dissolves the presursor and the cooler end causes seeds to take additional growth. The advantages of the hydrothermal method over other types of crystal growth include the ability to create crystalline phases which are not stable at the melting point. The method is also particularly suitable for the growth of large good-quality nanocrystals from 0D to 3D while maintaining good control over their composition. For example, ZnO nanowire arrays

have been synthesized by the hydrothermal method although ZnO nanowires have been synthesized by thermal evaporation, gold-catalyzed vapor-phase transport, and vapor–liquid–solid growth in general.[27] ZnO nanowire arrays composed of the hexagonal wurtzite crystal structure were directly grown in a preferred [0001] direction on Zn foil by a hydrothermal process. In addition, considerable efforts have been devoted to the preparation of high-quality TiO_2 nanomaterials for applications in photocatalytic materials and photovoltaic cells. Diverse methods such as chemical vapor deposition, electrochemical syntheses, and sol-gel techniques have been successfully established to prepare anatase TiO_2 nanostructures.[28] In particular, hydrothermal syntheses of anatase TiO_2 nanostructures have been found to be quite advantageous particularly from viewpoints of environmental friendliness, easy upward scaling, and low production cost.[29] Although anatase TiO_2 nanocrystals with being treated via a high-temperature post-annealing process have been employed as photocatalytic or photovoltaic materials,[30] the hydrothermal synthesis of anatase TiO_2 nanostructures on Ti foil without being treated via any post-annealing process has been hardly reported yet. The direct photocatalytic and photovoltaic applications of anatase TiO_2 nanopopcorns on Ti foil have not been reported although ZnO nanowires grown on FTO glass[31] or TiO_2 nanowires grown on Ti foil[32] have been utilized in DSSCs. I report the facile one-pot hydrothermal preparation of anatase TiO_2 nanopopcorns on Ti foil to be employed for photocatalytic and photovoltaic materials directly without being treated via any annealing process. The growth of tetragonal anatase TiO_2 nanopopcorns on Ti foil has been controlled hydrothermally by changing the volume ratio of H_2O_2 : HF : H_2O.

24

1.4 References

[1] C. Burda, X.B. Chen, R. Narayanan, M.A. El-Sayed, *Chem. Rev.* **2005**, *105*, 1025.

[2] M. Nirmal, L. E. Brus, *Acc. Chem. Res.* **1999**, *32*, 407.

[3] A. L. Efros, M. Rosen, *Annu. Rev. Mater. Sci.* **2000**, 30, 475.

[4] C. Kittel, *Introduction to Solid State Physics*, *John Wiley & Sons*, **1953**.

[5] A. S. Edelstein, R. C. Cammarata, *Nanomaterials: Synthesis, Properties and Applications*, *Institute of Physics Publishing*, **2001**.

[6] B. L. Wehrenberg, C. J. Wang, P. Guyot-Sionnest, *J. Phys. Chem. B.* **2002**, *106*, 10634.

[7] Landolt-Bornstein, *Semiconductor: Physics of Nontetrahedrally Bonded Binary Compounds II*, *Springer-Verlag*, **1983**.

[8] T. J. Bukowski and J. H. Simmons, Quantum dot research: Current state and future prospects, Critical Reviews in Solid State and Materials Science, 2002, 27, 119.

[9] H. Mattoussi, L. H. Radzilowski, B. O. Dabbousi, E. L. Thomas, M. G. Bawendi, M. F. Rubner, *J. Appl. Phys.* **1998**, *83*, 7965.

[10] Q. B. Wang, N. Iancu, D.-K. Seo, *Chem. Mater.* **2005**, *17*, 4762.

[11] F.-Y. Liu, J.-S. Yu, *J. Colloid Interf. Sci.* **2010**, *315*, 1.

[12] H. Peng, L. J. Zhang, C. Soeller, J. Travas-Sejdic, *J. Lumin.* **2007**, *127*, 721.

[13] X.-Y. Huang, J. Li, Y. Zhang, A. Mascarenhas, *J. Am. Chem. Soc.* **2003**, *125*, 7049.

[14] M. H. Cao, I. Djerdj, Z. Jagličić, M. Antonietti, M. Niederberger, *Phys. Chem. Chem. Phys.* **2009**, *11*, 6166.

[15] K.-S. Lee, M. A. El-Sayed, *J. Phys. Chem. B.* **2006**, *110*, 19220.

[16] C. Dupas, P. Houdy, M. Lahmani, *Nanoscience: Nanotechnologies and Nanophysics*, *Springer-Verlag*, **2007**.

[17] C. P. Poole, F. J. Owen, *Introduction to Nanotechnology*, *John Wiley & Sons*, **2003**.

[18] R. Werner, T. Hoche, S. G. Mayr, *CrystEngComm*, **2011**, *13*, 3046.

[19] C. C. Koch, *Nano Structured Materials: Processing Properties and Applications*, *Noyes Publications*, **2002**.

[20] P. Jeevanandam, Y. Koltypin, A. Gedanken, *Nano Lett.* **2001**, *1*, 263.

[21] H. Cheraghi, M. Shahmiri, Z. Sadeghian, *Thin Solid Film.* **2012**, *522*, 289.

[22] J.-Y. Kim, D. H. Lee, S. J. Kim, D.-J. Jang, *J. Colloid Interface Sci.* **2008**, *326*, 387.

[23] S. Menzies, D. P. Anderson, *J. Electrochem. Soc.* **1990**, *138*, 440.

[24] M. J. Zheng, L. D. Zhang, G. H. Li, W. Z. Shen, *Chem. Phys. Lett.* **2002**, *363*, 123.

[25] J.-Y. Kim, H. Jeong, D.-J. Jang, *J. Nanopart. Res.* **2011**, *13*, 6699.

[26] M. O'Donoghue, *A Guide to Man-Made Gemstones*. **1983**, 40.

[27] M. H. Huang, S. Mao, H. Feick, H. Q. Yan, Y. Y. Wu, H. Kind, E. Weber, R. Russo, P. D. Yang, *Science* **2001**, *292*, 1897.

[28] J. W. Hou, X. C. Yang, X. Y. Lv, M. Huang, Q. Y. Wang, J. Wang, *J. Alloy. Compd.* **2012**, *511*, 202.

[29] X. H. Yang, Z. Li, C. H. Sun, H. G. Yang, C. Z. Li, *Chem. Mater.* **2011**, *23*, 3486.

[30] N. K. Allam, C. A. Grimes, *Langmuir* **2009**, *25*, 7234.

[31] M. Law, J. C. Johnson, R. Saykally, P. D. Yang, *Nature Mater.* **2005**, *4*, 455.

[32] J.-Y. Liao, H.-Y. Chen, D.-B. Kuang, C.-Y. Su, *Energy Environ. Sci.* **2012**, *5*, 5750.

Chapter 2. Hydrothermal Growth Control of ZnSe·N$_2$H$_4$ Nanobelts[†]

2. 1. Abstract

Uniform and well-defined inorganic-organic hybrid nanobelts of the hexagonal wurtzite $ZnSe \cdot N_2H_4$ having an average width of 200 nm, a mean thickness of 25 nm, and a typical length of a few micrometers have been grown facilely in an aqueous solution, and characterized by measuring photoluminescence spectra and kinetic profiles as well as diffraction patterns and electron microscopic images. The length-to-width and width-to-thickness ratios of $ZnSe \cdot N_2H_4$ nanobelts have been controlled well by adjusting [Se]-to-[$ZnCl_2$] ratios as well as reaction time and temperature in hydrazine-hydrate-assisted hydrothermal reactions. The sufficient amount of the selenium precursor has been found to be essential for the one-dimensional growth of crystalline $ZnSe \cdot N_2H_4$ nanobelts. Photoluminescence from $ZnSe \cdot N_2H_4$ nanobelts shifts to the red by 16 nm and increases 3.5 times with the increase of the [Se]-to-[$ZnCl_2$] ratio. The mean lifetime of photoluminescence kinetics having three decay components of 18 ps, 85 ps, and 1300 ps increases with the length-to-width ratios of $ZnSe \cdot N_2H_4$ nanobelts.

2. 2. Introduction

The spectroscopic, electronic, and chemical properties of nanostructured materials are of great interest in both basic and applied research.[1–6] In particular, one-dimensional nanostructures based on rods, wires, belts, and ribbons, as well as their related three-dimensional organizations, have become the focus of intensive research.[7–11] Studies on these materials aim both to assess the foundations of physical laws at the nanoscale and to pave the way to practical applications.[11] A nanobelt, as a representative of quasi-one-dimensional nanostructures, has attracted considerable attention because of their proven potential use as both interconnects and functional units in electronic, optoelectronic, electrochemical, and electromechanical devices.[7–9,12–16] Compared to common nanowires having round cross sections, a nanobelt provides a large interface area when deposited on an electrode, thus facilitating the fabrication of devices with improved electrical contact.[15] Nanobelts having ribbon shapes with rectangular cross sections can be easily synthesized without using any templates.[12,16]

Among the II–VI semiconductors, ZnSe-based nanostructures with a room temperature bulk band gap of 2.7 eV (460 nm) have been the subject of intense interest in view of their wide-ranging applications in light-emitting diodes, blue-light-emitting lasers, and photodetectors.[13,17–20] One-dimensional ZnSe nanostructures have been prepared by using various methods such as laser ablation, thermal evaporation, metal-organic chemical vapor deposition, and molecular beam epitaxy.[21–24] In addition, there has been

a hydrothermal process to represent a simple and economical method for the fabrication of one-dimensional ZnSe nanostructures.[25] However, there are few reports on the synthesis of ZnSe nanobelts via a hydrothermal process. This may be due to the fact that it is generally difficult to control the nucleation and growth of ZnSe for the fabrication of well-controlled one-dimensional nanostructures.

In this paper, we report a hydrazine-hydrate-assisted hydrothermal process to synthesize inorganic-organic hybrid $ZnSe \cdot N_2H_4$ nanobelts having controlled length-to-width and width-to-thickness ratios. Inorganic–organic hybrid nanocomposite materials receive much attention because of their tremendous potential in providing enhanced material properties that are not easily achievable with either organic or inorganic materials alone.[26–30] These nanomaterials exhibit significantly enhanced electronic and optical properties including band-gap tunability and high band-edge absorption.[27–29] Hybrid nanocomposite materials also have additional advantage of perfectly ordered crystal structures, thus allowing high carrier mobility. Although the preparation of $ZnSe \cdot (diethylenetriamine)_{0.5}$ hybrid nanobelts[30] and the synthesis of $ZnSe \cdot N_2H_4$ microrods[31] were reported, the synthesis of $ZnSe \cdot N_2H_4$ hybrid nanobelts has not been reported yet. The application of $ZnSe \cdot N_2H_4$ has hardly been reported although $ZnSe \cdot N_2H_4$ has been often employed as the precursor of ZnSe nanostructures.[30–33] The growth of hexagonal wurtzite $ZnSe \cdot N_2H_4$ nanobelts has been controlled hydrothermally by changing reaction conditions diversely. We have found that the length-to-width ratio of $ZnSe \cdot N_2H_4$ nanobelts increases sensitively with the increment of the $[Se]$-to-$[ZnCl_2]$ ratio.

2. 3. Experimental Details

The analytical grade chemicals of $ZnCl_2$(s), Se(s), and $N_2H_4 \cdot H_2O$(l) were used as purchased from Sigma-Aldrich. Deionized water with a resistivity of greater than 18 MΩ cm, from a Millipore Milli-Q system, was used throughout the experiments. For the typical preparation of $ZnSe \cdot N_2H_4$ nanobelts using a [Se]-to-[$ZnCl_2$] ratio of x, 15 mL of 6.7(x) mM Se in $N_2H_4 \cdot H_2O$ was added to 15 mL of 6.7 mM $ZnCl_2$ in deionized water and stirred vigorously for 1 h. The mixture solution was then loaded into a Teflon-lined stainless-steel autoclave of 50 mL capacity, placed in an oven at 180 $^{\circ}$C for 6 h, and then cooled to room temperature. A white precipitate produced in the reaction mixture was washed three times with deionized water and ethanol to remove residual impurities. Colloidal samples were prepared by redispersing $ZnSe \cdot N_2H_4$ nanobelts in deionized water immediately prior to use in order to avoid the precipitation and the decomposition of nanobelts in water. We have found the above optimal conditions for the synthesis of $ZnSe \cdot N_2H_4$ nanobelts after we tried diverse reaction conditions such as reaction temperature, reaction time, precursor amounts, and reaction vessels.

While transmission electron microscopy (TEM) images and selected-area electron diffraction (SAED) patterns were obtained with a Hitachi H-7600 microscope, high-resolution transmission electron microscopy (HRTEM) and fast Fourier transformation (FFT) patterns were measured using a JEOL JEM-3000F microscope. Scanning electron microscopy (SEM) images and energy dispersive X-ray (EDX) analysis were recorded with a JEOL JSM-

6700F microscope, and high-resolution X-ray diffraction (HRXRD) patterns were obtained with a Bruker D8 DISCOVER diffractometer using $Cu_{\kappa\alpha}$ radiation ($\lambda = 0.15418$ nm). X-ray photoelectron spectroscopy (XPS) was monitored using a Sigma Probe ThermoVG spectrometer with an excitation source of $Mg_{\kappa\alpha} = 1253.60$ eV, and photoluminescence spectra were measured employing a Princeton Instruments ICCD576G CCD detector with excitation using 266 nm pulses from a Q-switched Quantel Brilliant Nd:YAG laser of 6 ns. Photoluminescence kinetic profiles were measured with a Hamamatsu C2830 streak camera of 10 ps attached with a Princeton Instruments RTE128H CCD detector after exciting samples using 266 nm pulses from a mode-locked Quantel YG501 Nd:YAG laser of 25 ps. Kinetic constants were extracted by fitting measured kinetic profiles to computer-simulated exponential curves convoluted with instrument response functions.

2. 4. Results and Discussion

The TEM and SEM images of Figure 2-1 show that $ZnSe \cdot N_2H_4$ nanobelts grown at 180 $^{\circ}$C for 6 h with various [Se]-to-[$ZnCl_2$] ratios are uniform in width and thickness along their entire lengths. $ZnSe \cdot N_2H_4$ nanobelts prepared with a [Se]-to-[$ZnCl_2$] ratio of 1.0 have an average width of 200 nm, a mean thickness of 25 nm with an average width-to-thickness ratio of 8, and a typical length of a few micrometers. Comparing Figure 2-1b with Figure 2-1a and 2-c and Figure 2-2, we note that the width, the width-to-thickness ratio, and the length of a

ZnSe·N$_2$H$_4$ nanobelt increase whereas the thickness of the nanobelt decreases with the increment of the [Se]-to-[ZnCl$_2$] ratio. This suggests that the sufficient amount of precursor selenium is essential for the growth of thin, long, and uniform ZnSe·N$_2$H$_4$ nanobelts. In particular, ZnSe·N$_2$H$_4$ nanobelts grown with a [Se]-to-[ZnCl$_2$] ratio of 0.43 are similar to rectangular nanoplates in shape because of their short lengths.
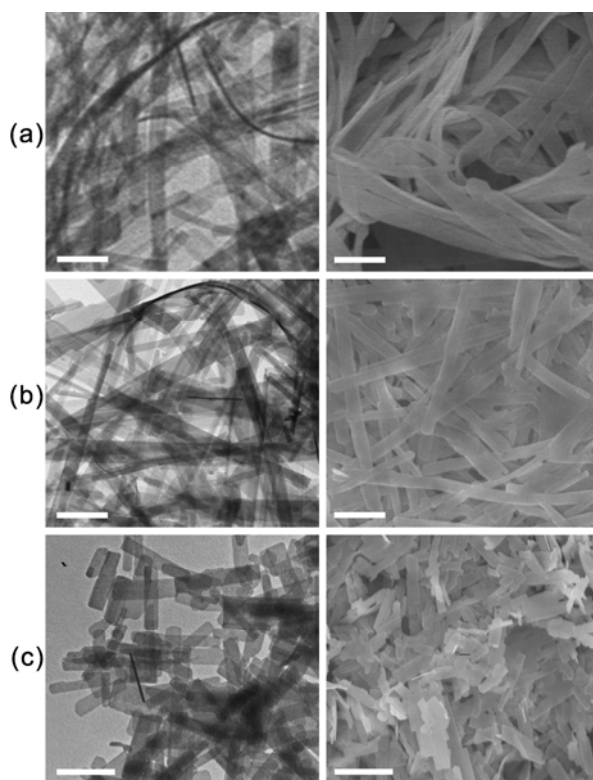

Figure 2-1 TEM (left) and SEM images (right) of ZnSe·N$_2$H$_4$ nanobelts grown at 180 °C for 6 h using [Se]-to-[ZnCl$_2$] ratios of 2.3 (a), 1.0 (b), and 0.43 (c). Each scale bar indicates 500 nm.
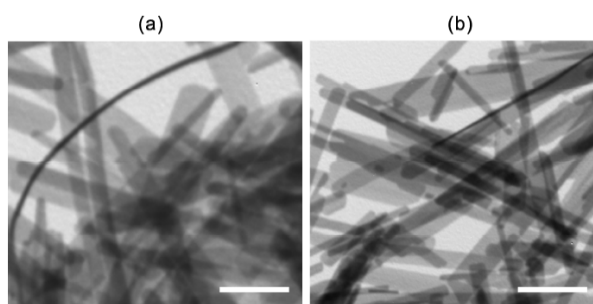

Figure 2-2 TEM images of ZnSe·N$_2$H$_4$ nanobelts grown at 180 °C for 6 h using [Se]-to-[ZnCl$_2$] ratios of 1.5 (a) and 0.67 (b). Each scale bar indicates 500 nm.

The HRXRD patterns of Figure 2-3 show that our fabricated nanobelts have polycrystalline structures of the hexagonal wurtzite $ZnSe·N_2H_4$ with lattice constants of a = 16.546 Å and c = 11.145 Å (JCPDS Card No. 00-037-0619). The mean crystallite diameter, d, of the small nanocrystals can be determined from the line width of a HRXRD spectrum by the Scherrer's formula $<d> = 0.94 \lambda / (B \cos \theta_B)$, where λ is the X-ray wavelength, B is the full width at the half maximum of the diffraction peak (radian), and θ_B is the half angle of the diffraction peak on the 2θ scale.[34–36] The mean crystallite diameter of small nanoparticles in $ZnSe·N_2H_4$ nanobelts grown with a [Se]-to-[$ZnCl_2$] ratio of 1.0 has been estimated to be 10.7 nm by using the (132) peak at 2θ of 27.6°. The mean crystallite diameter becomes 12.7 nm in $ZnSe·N_2H_4$ nanobelts grown with a [Se]-to-[$ZnCl_2$] ratio of 2.3 and 8.4 nm in nanobelts grown with a [Se]-to-[$ZnCl_2$] ratio of 0.43. This, together with the HRXRD pattern shapes of Figure 2-3, designates that the crystallinity of $ZnSe·N_2H_4$ nanobelts enhances highly with the increase of the [Se]-to-[$ZnCl_2$] ratio. This also suggests that the sufficient amount of precursor selenium is indispensable for the growth of uniform $ZnSe·N_2H_4$ nanobelts.

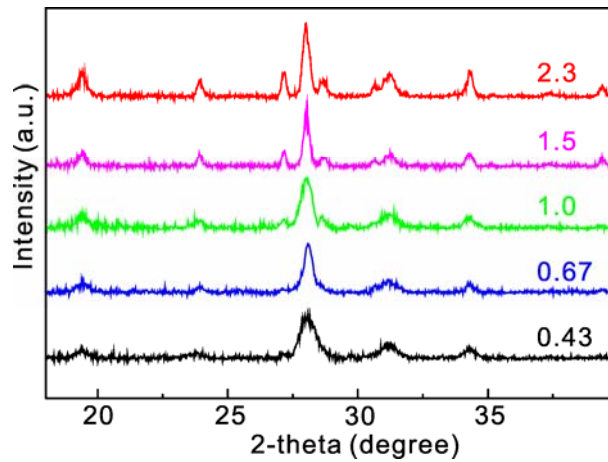**Figure 2-3** HRXRD patterns of $ZnSe·N_2H_4$ nanobelts grown at 180 °C for 6 h. The employed ratios of [Se]-to-[$ZnCl_2$] are indicated inside.

The microstructural details of a ZnSe·N$_2$H$_4$ nanobelt have been further provided by measuring the HRTEM image and the fast Fourier transformation (FFT) pattern of Figure 2-4. The HRTEM image of Figure 2-4a monitored on a central area of a nanobelt grown with a [Se]-to-[ZnCl$_2$] ratio of 1.0 shows indeed that the nanobelt consists of small ZnSe·N$_2$H$_4$ nanocrystals ranging from 10 nm to 22 nm in size. The observed lattice-fringe distances of ZnSe·N$_2$H$_4$ nanocrystals are 0.33, 0.32, and 0.30 nm, which correspond to the spacing lengths of the (222), the (132), and the (110) planes of the hexagonal wurtzite ZnSe·N$_2$H$_4$, respectively. The HRXRD patterns of Figure 2-3 have also indicated that nanobelts are composed of hexagonal wurtzite ZnSe·N$_2$H$_4$ nanocrystals having an average diameter of 10.7 nm. The typical FFT pattern of Figure 2-4b, recorded from the same nanobelt of Figure 2-4a, also suggests that the nanobelt has the crystalline structure of the hexagonal wurtzite ZnSe·N$_2$H$_4$. All the average d-spacing values calculated from the FFT diffraction spots of Figure 2-4b agree well with the individual standard interplanar distances of the hexagonal wurtzite ZnSe·N$_2$H$_4$ crystal. Consequently, both the HRTEM image and the FFT pattern of Figure 2-4 suggest that the nanobelt has been well fabricated hydrothermally to show the well-defined crystalline structure of the hexagonal wurtzite ZnSe·N$_2$H$_4$.
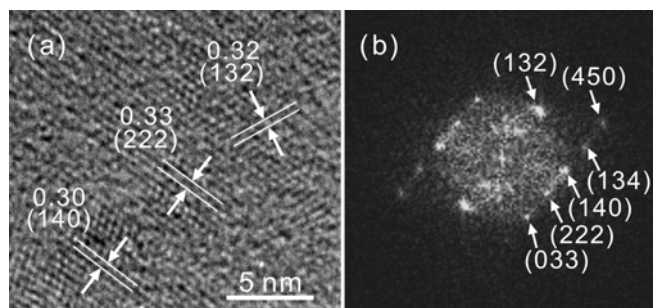

Figure 2-4 HRTEM image (a), showing lattice plane distances, and FFT pattern (b), showing lattice planes, of a hexagonal wurtzite ZnSe·N$_2$H$_4$ nanobelt grown at 180 $^\circ$C for 6 h with a [Se]-to-[ZnCl$_2$] ratio of 1.0.

The XPS spectra of Figure 2-5 can provide further significant information about the quality and surface composition of the products. The binding energies obtained in the XPS analysis were corrected for specimen charging, through referencing the C 1s to 285.60 eV. The main peak in Se $3d_{5/2}$ has an asymmetric line shape, characteristic of a metallic system. The binding energies of Se $3d_{5/2}$ and Zn $2p_{3/2}$ were identified at 53.61 eV and 1023.77 eV, respectively. The signals at 10.0 eV and 997.83 eV can be attributed to the binding energy of Zn 3p and the kinetic energy of Zn LMN, respectively. The signal of Zn $2p_{3/2}$, which was easily affected by the chemical environment, was much stronger than that of Zn 3p. This result implies that Zn was not exposed to air due to binding to hydrazine.[19] The Auger parameter, which was derived from the binding energy of Zn $2p_{3/2}$ and the kinetic energy of Zn LMN, is approximately 2019.60 eV, and can be used to compare the results of different XPS studies reliably because it is independent of the calibration accuracy of the binding energy scale. The Auger parameter is 5.6 eV higher than the reported average value of 2014.0 eV for elemental Zn.[19,37,38] This large blue shift suggests that Zn is also bound to a very electronegative element such as N. The Gaussian fitting of the N 1s XPS spectrum yields two distinct forms. The binding energies 398.04 eV and 400.45 eV of N 1s could be attributed to N-Zn and N-H bonds, respectively.[39] The binding energy of the N-Zn bond was derived from a zinc-hydrazine complex, $[Zn(N_2H_4)]^{2+}$. Quantitative analysis of XPS spectra reveals that the atomic ratio of Zn:Se is 1:1.42. Because the XPS analysis just shows the elemental composition on the surface in general, we have also carried out EDX elemental analysis, which has indicated the atomic ratio of Zn:Se to be 1:1.08. Both elemental analysis results have shown that the Se content is greater than that of Zn. This suggests that largely excessive selenium ions give kinetic forces for the anisotropic growth of wurtzite ZnSe·N_2H_4 nanobelts. The weak high-resolution XPS spectrum of the O 1s region indicates that only one oxygen

contribution exists at 532 eV due to the core level of the small amount of physically absorbed H_2O.[40] This further demonstrates that the as-obtained product is pure $ZnSe·N_2H_4$.
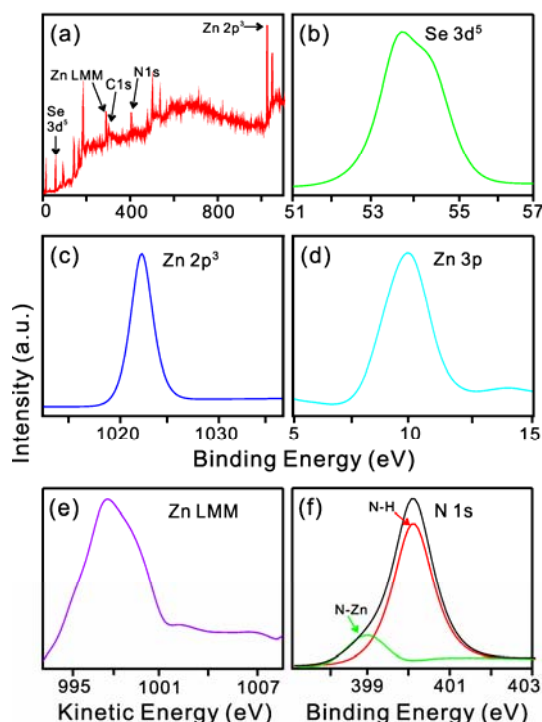
Figure 2-5 Survey (a), Se $3d_{5/2}$ (b), Zn $2p_{5/2}$ (c), Zn 3p (d), Zn LMM (e), and N 1s (f) XPS spectra of $ZnSe·N_2H_4$ nanobelts grown at 180 °C for 6 h with a [Se]-to-[$ZnCl_2$] ratio of 1.0.

Figure 2-6 shows that the photoluminescence spectra of $ZnSe·N_2H_4$ nanobelts are blue-shifted largely by 30 nm from that of bulk ZnSe(s) at 460 nm due to the quantum confinement effect of the nanobelts.[6,11,27,30] The spectra then shift gradually to the red by 16 nm with the increase of the [Se]-to-[$ZnCl_2$] ratio. The red shift has been attributed to the size increase of $ZnSe·N_2H_4$ nanobelts with the increase of the [Se]-to-[$ZnCl_2$] ratio as seen in Figure 2-1. The photoluminescence intensity of $ZnSe·N_2H_4$ nanobelts increases steadily 3.5 times with the increase of the [Se]-to-[$ZnCl_2$] ratio (Table 2-1). The intensity increase has been attributed to the decrease of defect sites owing to crystallinity increase

as discussed with Figure 2-3, as well as the decrease of surface states owing to size increase as shown in Figure 2-1, with the increase of the [Se]-to-[ZnCl$_2$] ratio.
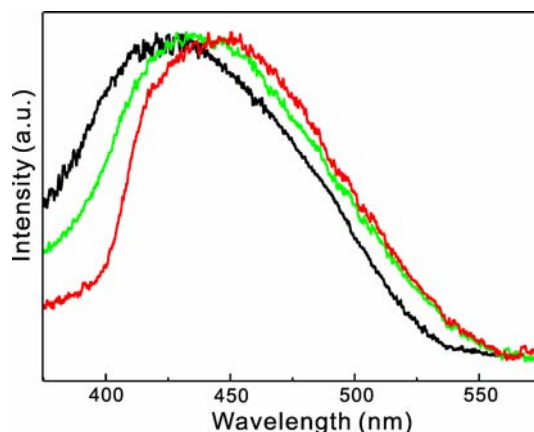
Figure 2-6 Maximum-normalized photoluminescence spectra of ZnSe·N$_2$H$_4$ nanobelts grown at 180 $^{\circ}$C for 6 h with [Se]-to-[ZnCl$_2$] ratios of 0.43 (black), 1.0 (green), and 2.3 (red). Nanobelts were suspended in water and excited at 266 nm.

Figure 2-7 reveals that the photoluminescence kinetic profiles of ZnSe·N$_2$H$_4$ nanobelts look similar to one another with having three decay components although their mean emission lifetimes increase with the increase of the [Se]-to-[ZnCl$_2$] ratio (Table 2-1). The fast decay time of 18 ps has been attributed to arise from the trapping time of electrons in the conduction band of ZnSe·N$_2$H$_4$ nanobelts while the medium decay time of 85 ps has been assigned to the relaxation of electrons at trap sites via trapping into surface states. We have then attributed the slow decay time of 1300 ps to the hole recombination time of electrons at surface states. The amplitude decrease of the fast decay component with the increase of the [Se]-to-[ZnCl$_2$] ratio can be attributed to the decrease of defect sites owing to crystallinity increase as discussed with Figure 2-3.[41,42]

The increase of the mean emission lifetime with the increment of the [Se]-to-[ZnCl$_2$] ratio also matches with the intensity increase of photoluminescence in Figure 2-7.
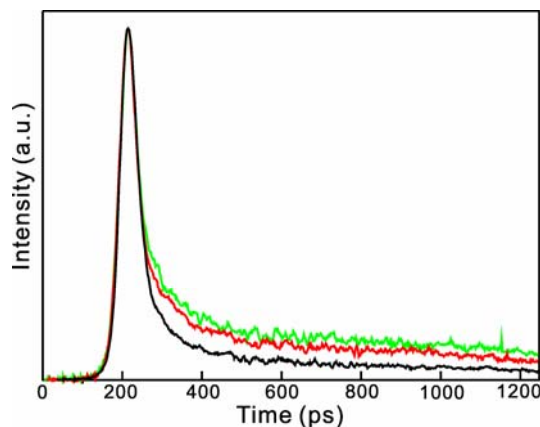
Figure 2-7 Maximum-normalized photoluminescence decay kinetic profiles, monitored at 400 nm after excitation at 266 nm, of ZnSe·N$_2$H$_4$ nanobelts grown at 180 °C for 6 h with [Se]-to-[ZnCl$_2$] ratios of 0.43 (black), 1.0 (green), and 2.3 (red) and suspended in water.

The TEM and SEM images of Figure 2-8 display the time-dependent growth of ZnSe·N$_2$H$_4$ nanobelts well. Once leaflike ZnSe·N$_2$H$_4$ nanoflakes were formed kinetically (Figure 2-8a), they were suggested to undergo intraparticle ripening to form elongated rectangular nanoplates (Figure 2-8b) and short nanobelts subsequently (Figure 2-8c). Further aging has induced Ostwald ripening to form smooth, well-defined, crystalline, and elongated ZnSe·N$_2$H$_4$ nanobelts finally (Figure 2-8d).[43] The temperature-dependent TEM images and SAED patterns of Figure 2-9 show indeed that growth kinetics with sufficient thermal energy plays a key role in determining the morphology of ZnSe·N$_2$H$_4$ nanobelts.[44] High temperature as 180 °C has offered a suitable kinetic growth condition along the *c* axis of the hexagonal wurtzite ZnSe·N$_2$H$_4$ structure. According to the viewpoint of the free energy, the growth of the existing nucleus is energetically more

favorable than the formation of new nuclei. This may explain that the long-time reaction

has induced increment in the lengths of ZnSe·N$_2$H$_4$ nanobelts.

Table 2-1 Spectral Data and Decay Kinetic Constants of ZnSe·N$_2$H$_4$ Photoluminescence[a]

[Se]/[ZnCl$_2$]	λ_{max} (nm)[b]	Intensity[c]	Mean lifetime (ps)	Lifetime (ps)
0.43	430	0.37	50	18 (89%) + 85 (9%) + 1300 (2%)[d]
1.0	438	1.0	66	18 (83%) + 85 (14%) + 1300 (3%)
2.3	446	1.3	65	18 (85%) + 85 (12%) + 1300 (3%)

[a] Obtained from Figures 2-5 and 2-6. [b] Wavelength at the emission maximum. [c] Relative peak intensity. [d] Initial intensity percentage of each component.
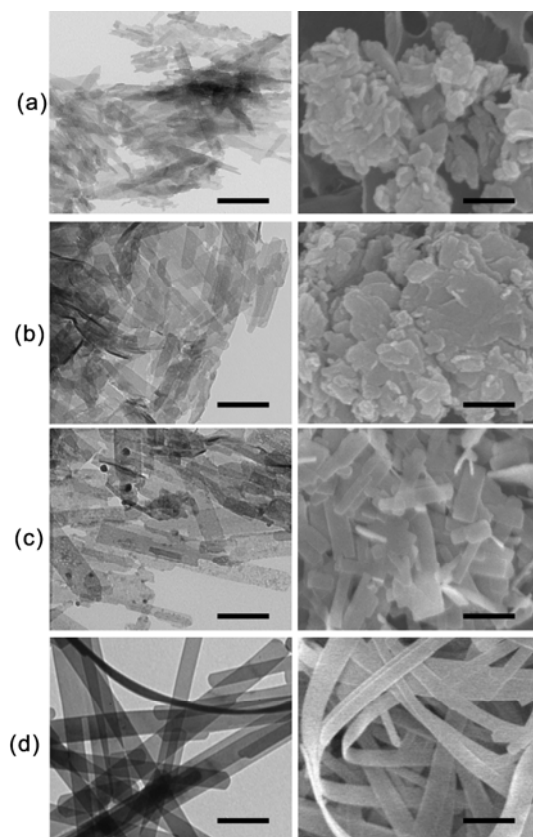
Figure 2-8 TEM (left) and SEM images (right) of ZnSe·N$_2$H$_4$ nanobelts grown at 180 °C for 0.5 h (a), 1.5 h (b), 3.0 h (c), and 6.0 h (d) with a [Se]-to-[ZnCl$_2$] ratio of 1.0. Each scale bar indicates 500 nm.
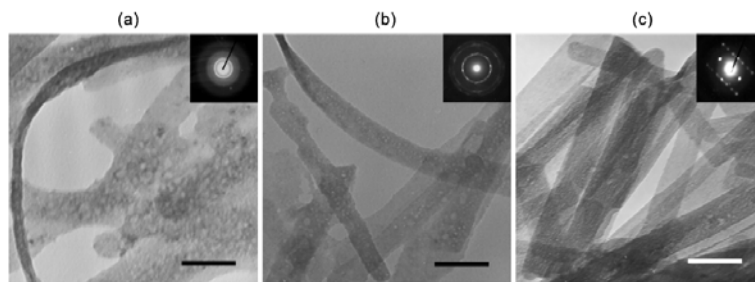
Figure 2-9 TEM images and SAED patterns (insets) of ZnSe·N$_2$H$_4$ nanobelts grown for 6 h at 100 °C (a), 140 °C (b), and 180 °C (c) with a [Se]-to-[ZnCl$_2$] ratio of 1.0. Each scale bar indicates 200 nm.

The formation mechanism of hexagonal wurtzite ZnSe·N$_2$H$_4$ nanobelts can be proposed as follows. Hydrazine hydrate is considered to play a crucial role.[31–33,45–52] First, hydrazine hydrate dissolves selenium powder to produce a brown solution.[45–50] Moreover, it acts as a strong reducing agent of selenium to form selenium ions. If the experiment was conducted in an aqueous solution without having hydrazine hydrate, no reaction took place because of the low solubility of selenium powder and the absence of a reducing agent. Hydrazine hydrate is a base slightly weaker than ammonium hydroxide and dissociates according to the following equilibrium in an aqueous solution:[32,33,46,47]

$$N_2H_4 \cdot H_2O \leftrightarrows N_2H_5^+ + OH^- \tag{1}$$

Elemental selenium powder is soluble in hydrazine hydrate, and hydrazinium (N$_2$H$_5^+$) ions can reduce Se to Se^{2-}.[33,45,46] The overall reaction can be expressed as follows:[33,46]

$$N_2H_5^+ + 2Se + 5OH^- \rightarrow N_2 + 2Se^{2-} + 5H_2O \tag{2}$$
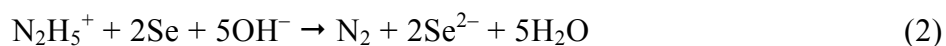
Hydrazine also has a strong coordination ability to zinc that favors the growth of one-dimensional nanocrystals.[32,49,50] A hydrazine molecule coordinates a zinc ion to generate a zinc-hydrazine complex, [Zn(N$_2$H$_4$)]$^{2+}$,[46–50] which then combines with a selenium ion to

form $ZnSe \cdot N_2H_4$. The newly produced $ZnSe \cdot N_2H_4$ finally undergoes heterogeneous nucleation in the solution with a preferential direction along the *c* axis to produce one-dimensional $ZnSe \cdot N_2H_4$ nanostructures. Driving forces for the growth of one-dimensional nanostructures are suggested to come from excessive selenium ions existing in the solution. It has been reported that if two precursors are employed to synthesize semiconductor nanocrystals, an excess of the relatively less reactive precursor often generates elongated nanoparticles with high aspect ratios.[45,52] Thus, we consider that largely excessive selenium ions have given kinetic forces for anisotropic growth along the *c* axis of the hexagonal wurtzite hydrazinozinc selenide.[33] Controlled experiments have indicated indeed that a relatively high selenium concentration is essential for the production of $ZnSe \cdot N_2H_4$ nanobelts having high length-to-width ratios. Wang *et al.* have attributed the exceptional wurtzite-structural stability to the particular nanobelt morphology.[53] The wurtzite nanobelt represents a structure with a lower surface energy than the sphalerite nanoparticle does, because the lowest-energy plane in the wurtzite structure corresponds to the largest surfaces (top and bottom) of the nanobelt in direct contrast to the sphalerite structure.[12,53]

2. 5. Conclusions

A facile hydrothermal approach has been developed for the controlled growth of crystalline, uniform, and well-defined inorganic-organic hybrid nanobelts having the hexagonal wurtzite structure of hydrazinozinc selenide. Although typical ZnSe·N$_2$H$_4$ nanobelts have an average width of 200 nm, a mean thickness of 25 nm, and an average length of a few micrometers, their length-to-width and width-to-thickness ratios have been well controlled by adjusting [Se]-to-[ZnCl$_2$] ratios as well as reaction time and temperature in hydrazine-hydrate-assisted hydrothermal reactions. Both the length-to-width ratio and the width-to-thickness ratio of a ZnSe·N$_2$H$_4$ nanobelt increase with the increment of the [Se]-to-[ZnCl$_2$] ratio. The crystallinity and the mean crystallite diameter of a ZnSe·N$_2$H$_4$ nanobelt were also found to increase with the [Se]-to-[ZnCl$_2$] ratio. These indicate that the sufficient amount of the selenium precursor is essential for the growth of thin, long, uniform, well-defined, and crystalline ZnSe·N$_2$H$_4$ nanobelts. XPS spectra have also suggested that largely excessive selenium ions give kinetic forces for the anisotropic growth of wurtzite ZnSe·N$_2$H$_4$ nanobelts. Photoluminescence from ZnSe·N$_2$H$_4$ nanobelts shifts to the red by 16 nm and its intensity increases 3.5 times with the increase of the [Se]-to-[ZnCl$_2$] ratio. The mean lifetime of photoluminescence kinetics having three decay components of 18 ps, 85 ps, and 1300 ps increases concomitantly with the length-to-width ratio of the ZnSe·N$_2$H$_4$ nanobelt structure.

43

2. 6. Acknowledgments

2. 7. References

[1] W. Ki, J. Li, *J. Am. Chem. Soc.* **2008**, *130*, 8114.

[2] S. J. Kim, C. S. Ah, D.-J. Jang, *Adv. Mater.* **2007**, *19*, 1064.

[3] Y. H. Gao and Y. Bando, *Nature* **2002**, *415*, 599.

[4] J.-Y. Kim, S. Lee, K. Yoo, D.-J. Jang, *Appl. Phys. Lett.* **2009**, *94*, 153301.

[5] B. Kang, G. Ceder, *Nature* **2009**, *458*, 190.

[6] H. B. Shen, H. Z. Wang, Z. J. Tang, J. Z. Niu, S. Y. Lou, Z. L. Du, L. S. Li, *CrystEngComm* **2009**, *11*, 1733.

[7] Z. W. Pan, Z. R. Dai, Z. L. Wang, *Science* **2001**, *291*, 1947.

[8] Y. K. Che, A. Datar, K. Balakrishnan, L. Zang, *J. Am. Chem. Soc.* **2007**, *129*, 7234.

[9] J. Joo, J. S. Son, S. G. Kwon, J. H. Yu, T. Hyeon, *J. Am. Chem. Soc.* **2006**, *128*, 5632.

[10] K.-B. Tang, Y. T. Qian, J.-H. Zeng, X.-G. Yang, *Adv. Mater.* **2003**, *15*, 448.

[11] P. D. Cozzoli, L. Manna, M. L. Curri, S. Kudera, C. Giannini, M. Striccoli, A. Agostiano, *Chem. Mater.* **2005**, *17*, 1296.

[12] L. W. Yin, Y. Bando, *Nature Mater.* **2005**, *4*, 883.

[13] S. L. Xiong, B. J. Xi, C. M. Wang, G. C. Xi, X. Y. Liu, Y. T. Qian, *Chem. Eur. J.* **2007**, *13*, 7926.

[14] J. F. Gong, S. G. Yang, J. H. Duan, R. Zhang, Y. W. Du, *Chem. Commun.* **2005**, 351.

[15] Y. K. Che, A. Datar, X. M. Yang, T. Naddo, J. C. Zhao, L. Zang, *J. Am. Chem. Soc.* **2007**, *129*, 6354.

[16] G. C. Li, K. Chao, H. R. Peng and K. Z. Chen, *J. Phys. Chem. C* **2008**, *112*, 6228.

[17] J. F. Suyver, S. F. Wuister, J. J. Kelly and A. Meijerink, *Phys. Chem. Chem. Phys.* **2000**, *2*, 5445.

[18] S. L. Xiong, J. M. Shen, Q. Xie, Y. Q. Gao, Q. Tang, Y. T. Qian, *Adv. Funct. Mater.* **2005**, *15*, 1787.

[19] W. T. Yao, S.-H. Yu, J. Jiang, L. Zhang, *Chem. Eur. J.* **2006**, *12*, 2066.

[20] B. Hou, Y. J. Li, Y. J. Liu, B. Yuan, M. F. Jia, F. Z. Jiang, *CrystEngComm* **2009**, *11*, 1789.

[21] Y. Jiang, X.-M. Meng, W.-C. Yiu, J. Liu, J.-X. Ding, C.-S. Lee, S.-T. Lee, *J. Phys. Chem. B* **2004**, *108*, 2784.

[22] Y.-C. Zhu, Y. Bando, *Chem. Phys. Lett.* **2003**, *377*, 367.

[23] O. S. Kumar, S. Soundeswaran, R. Dhanasekaran, *Cryst. Growth Des.* **2002**, *2*, 585.

[24] H. Wang, K. S. Wong, B. A. Foreman, Z. Y. Yang, G. K. L. Wong, *J. Appl. Phys.* **1998**, *83*, 4773.

[25] B. J. Xi, S. L. Xiong, D. C. Xu, J. F. Li, H. Y. Zhou, J. Pan, J. Y. Li, Y. T. Qian, *Chem. Eur. J.* **2008**, *14*, 9786.

[26] J. Bisquert, *Phys. Chem. Chem. Phys.* **2008**, *10*, 3175.

[27] X.-Y. Huang, J. Li, Y. Zhang, A. Mascarenhas, *J. Am. Chem. Soc.* **2003**, *125*, 7049.

[28] Y. Zhang, G. M. Dalpian, B. Fluegel, S.-H. Wei, A. Mascarenhas, X.-Y. Huang, J. Li, L.-W. Wang, *Phys. Rev. Lett.* **2006**, *96*, 026405.

[29] M. H. Cao, I. Djerdj, Z. Jagličić, M. Antonietti, M. Niederberger, *Phys. Chem. Chem. Phys.* **2009**, *11*, 6166.

[30] W. T. Yao, S.-H. Yu, X. Y. Huang, J. Jiang, L. Q. Zhao, L. Pan, J. Li, *Adv. Mater.* **2005**, *17*, 2799.

[31] Y. H. Ni, L. Zhang, L. Zhang, X. W. Wei, *Cryst. Res. Technol.* **2008**, *10*, 1030.

[32] Y. J. Dong, Q. Peng, Y. D. Li, *Inorg. Chem. Commun.* **2004**, *7*, 370.

[33] W. C. Benzing, J. B. Conn, J. V. Magee, E. J. Sheehan, *J. Am. Chem. Soc.* **1958**, *80*, 2657.

[34] M. R. Kim, D.-J. Jang, *Chem. Comm.* **2008**, 521.

[35] R. J. Bandaranayake, G. W. Wen, L. Y. Lin, H. X. Jiang, C. M. Sorensen, *Appl. Phys. Lett.* **1995**, *67*, 831.

[36] D. Routkevitch, T. Bigioni, M. Moskovits, J. M. Xu, *J. Phys. Chem.* **1996**, *100*, 14037.

[37] G. Qian, M. Nikl, J. F. Bei, J. Pejchal, S. Baccaro, R. Giorgi, A. Cecilia, G. R. Chen, *Opt. Mater.* **2007**, *30*, 91.

[38] A. Nayak, H. D. Banerjee, *Appl. Surf. Sci.* **1999**, *148*, 205.

[39] P. Cao, D. X. Zhao, J. Y. Zhang, D. Z. Shen, Y. M. Lu, B. Yao, B. H. Li, Y. Bai, X. W. Fan, *Appl. Surf. Sci.* **2008**, *254*, 2900.

[40] M. Futsuhara, K. Yoshioka, O. Takai, *Thin Solid Films* **1998**, *322*, 274.

[41] J. E. Kroeze, T. J. Savenije, J. M. Warman, *J. Am. Chem. Soc.* **2004**, *126*, 7608.

[42] M. R. Kim, J. H. Chung, D.-J. Jang, *Phys. Chem. Chem. Phys.* **2009**, *11*, 1003.

[43] J. H. Yu, J. Joo, H. M. Park, S.-I. Baik, Y. W. Kim, S. C. Kim, T. Hyeon, *J. Am. Chem. Soc.* **2005**, *127*, 5662.

[44] Z. L. Wang, J. H. Song, *Science* **2006**, *312*, 242.

[45] L. A. Shi, Y. M. Xu, Q. Li, *J. Phys. Chem. C* **2009**, *113*, 1795.

[46] J. Du, L. Q. Xu, G. F. Zou, L. L. Chai, Y. T. Qian, *Mater. Chem. Phys.* **2007**, *103*, 441.

[47] Y. D. Li, Y. Ding, Z. Y. Wang, *Adv. Mater.* **1999**, *11*, 847.

[48] Y. F. Liu, J. B. Cao, C. Li, J. H. Zeng, K. B. Tang, Y. T. Qian, W. Q. Zhang, *J. Cryst. Growth* **2004**, *261*, 508.

[49] H. T. Wang, T. Tian, S. C. Yan, N. P. Huang, Z. D. Xiao, *J. Cryst. Growth.* **2009**, *311*, 3787.

[50] L. L. Chai, J. Du, S. L. Xiong, H. B. Li, Y. C. Zhu, Y. T. Qian, *J. Phys. Chem. C*, **2007**, *111*, 12658.

[51] L. H. Zhang, H. Q. Yang, L. Li, R. G. Zhang, R. N. Liu, J. H. Ma, X. L. Xie, F. Gao, *Inorg. Chem.* **2008**, *47*, 11950.

[52] X. G. Peng, *Adv. Mater.* **2003**, *15*, 459.

[53] Z. W. Wang, L. L. Daemen, Y. S. Zhao, C. S. Zha, R. T. Downs, X. D. Wang, Z. L. Wang, R. J. Hemley, *Nature Mater.* **2005**, *4*, 922.

Chapter 3. Hydrothermal Fabrication of Well-Ordered ZnO Nanowire Arrays on Zn Foil: Room-Temperature Ultraviolet Nanolaser [†]

3. 1. Abstract

Well-ordered nanowires of the hexagonal wurtzite ZnO having an average diameter of 80 nm, a typical length of 12 lm, and a mean packing density of 7.5 nanowires μm^{-2} have been directly grown on Zn foil in a preferred [0001] direction by a hydrothermal process and employed for room temperature ultraviolet nanolasers. The lasing action of arrayed ZnO nanowires has been observed from 370 to 400 nm with threshold irradiance of 25 kW cm^{-2}. Photoluminescence decays biexponentially: the fast component is attributed to free-exciton decay, and the slow one is to bound-exciton decay. The amplitude of the fast component increases whereas its lifetime decreases with the increment of threshold irradiance, suggesting that ZnO nanowire arrays undergo a change in the lasing mechanism from exciton–exciton scattering to electron–hole plasma recombination.

3. 2. Introduction

Nanostructured materials having functional properties have been extensively investigated to assess the foundations of physical laws at the nanoscale and to pave the way to practical applications.[1–5] In particular, one-dimensional (1D) nanostructured semiconductor arrays of GaN, ZnSe, ZnS, and ZnO have attracted considerable interest in applications to ultraviolet (UV) laser devices due to their wide direct band-gaps ($\Delta E_g \geq 3.0$ eV).[6–14] Among them, ZnO ($\Delta E_g = 3.37$ eV) is considered as the most suitable material for UV laser devices because of its large exciton-binding energy (60 meV) compared with thermal energy (26 meV) at room temperature. Substantial efforts have been devoted to the fabrication of high-quality 1D ZnO nanowire arrays to make them promising candidates for applications in UV lasers, light-emitting diodes, solar cells, photocatalytic devices, and field-emission displays.[6–20] Although arrayed 1D ZnO nanowires have been synthesized by thermal evaporation, gold-catalyzed vapor-phase transport, and vapor-liquid-solid growth in general,[10–12] their hydrothermal synthesis has been found to be quite advantageous particularly from viewpoints of environmental friendliness, easy upward scaling, and low production cost.[7,14,17,21] In the present study, ZnO nanowire arrays composed of the hexagonal wurtzite crystal structure were directly grown in a preferred [0001] direction on Zn foil by a hydrothermal process. The lasing action of arrayed ZnO nanowires has been observed at UV wavelengths varying from 370 to 400 nm. The excitation irradiance (I_{ex})–dependent lasing action of well-ordered ZnO nanowire arrays on Zn foil has been found to

have threshold irradiance (I_{th}) of 25 kW cm^{-2}, which is lower than the value (70 kW cm^{-2}) reported for ZnO nanorod arrays on Si wafer.[14]

3. 3. Experimental Details

The analytical grade chemicals of Zn foil(s) and $N_2H_4 \cdot H_2O$(l) were used as purchased from Sigma-Aldrich. Deionized water with a resistivity of greater than 18 MΩ cm from a Millipore Milli-Q system was used throughout the experiments. For the typical preparation of ZnO nanowire arrays on Zn foil, 24 mL of deionized water, 6 mL of $N_2H_4 \cdot H_2O$, and Zn foil (10 mm x 10 mm x 0.25 mm) were loaded into a Teflon-lined stainless-steel autoclave of 50 mL capacity. The autoclave was placed in an oven at 180 $^{\circ}$C for 6 h and then cooled to room temperature. The Zn foil was removed from the solution and rinsed with deionized water to get rid of residual impurities. We have found the above described optimal conditions for the synthesis of well-ordered ZnO nanowire arrays on Zn foil after we tried diverse experimental conditions. $V(H_2O)/V(N_2H_4 \cdot H_2O)$ was 4.0 if not specified otherwise.

Transmission electron microscopy (TEM) images were obtained with a Hitachi H-7600 microscope, and high-resolution transmission electron microscopy (HRTEM) images and fast Fourier transformation (FFT) patterns were measured using a JEOL JEM-3000F microscope. Scanning electron microscopy (SEM) images and energy dispersive X–ray (EDX) profiles were recorded with a JEOL JSM-6700F microscope, and high-resolution X–ray diffraction

51

(HRXRD) patterns were obtained with a Bruker D8 DISCOVER diffractometer using Cu Kα

radiation (λ = 0.15418 nm). X–ray photoelectron spectroscopy (XPS) were monitored using a

Sigma Probe ThermoVG spectrometer with an excitation source of Al Kα = 1486.6 eV.

Absorption spectra were measured using a StellarNet EPP2000C UV-VIS reflectance

spectrometer, and Raman spectra were measured using an OLYMPUS BX41 confocal

microscope Raman system equipped with a Dynamic Laser LS300 Ar$^+$ laser as the excitation

source. Photoluminescence spectra were measured employing a Princeton Instruments

ICCD576G CCD detector with excitation using 266 nm pulses from a Q-switched Quantel

Brilliant Nd:YAG laser of 6 ns. Photoluminescence kinetic profiles were measured with a

Hamamatsu C2830 streak camera of 10 ps attached to a Princeton Instruments RTE128H

CCD detector after exciting samples using 266 nm pulses from a mode-locked Quantel

Pizzicato Nd:YAG laser of 25 ps. Photoluminescence kinetic constants were extracted by

fitting measured kinetic profiles to computer-simulated exponential decay curves convoluted

with instrument response functions.

3. 4. Results and Discussion

The SEM and TEM images of Figure 3-1 show that well-ordered ZnO nanowires

having an average diameter of 80 nm, a typical length of 12 μm, and a mean packing

density of 7.5 nanowires μm^{-2} have been well grown directly on Zn foil. The EDX profile

of Figure 3-2 reveals that the elemental components of a ZnO nanowire are Zn and O indeed

and that the atomic molar ratio of Zn:O is 1:1.2. The microstructural details of a ZnO nanowire have been further provided by measuring the HRTEM image and the FFT pattern of Figure 3-1. The HRTEM image of a ZnO nanowire in Figure 3-1c shows that the observed lattice-fringe distance of 0.26 nm corresponds to spacing between the (002)
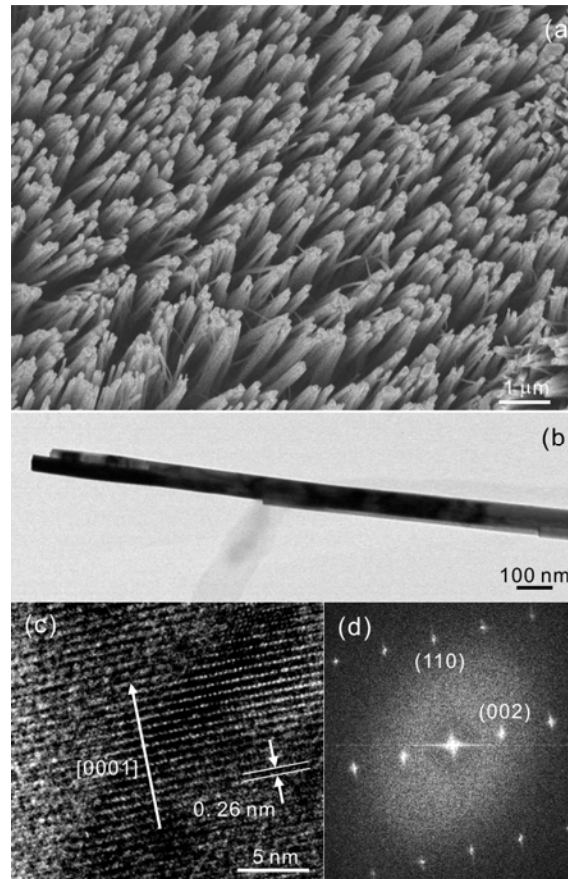
Figure 3-1 (a) SEM image of arrayed ZnO nanowires on Zn foil. (b) TEM image, (c) HRTEM image, showing the most preferred growth orientation and a lattice plane distance, and (d) FFT pattern, showing lattice planes, of a hexagonal wurtzite ZnO nanowire.
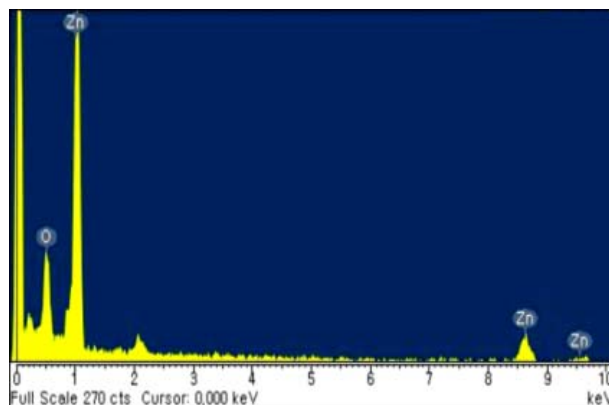
Figure 3-2 EDX profile of a ZnO nanowire grown on Zn foil.
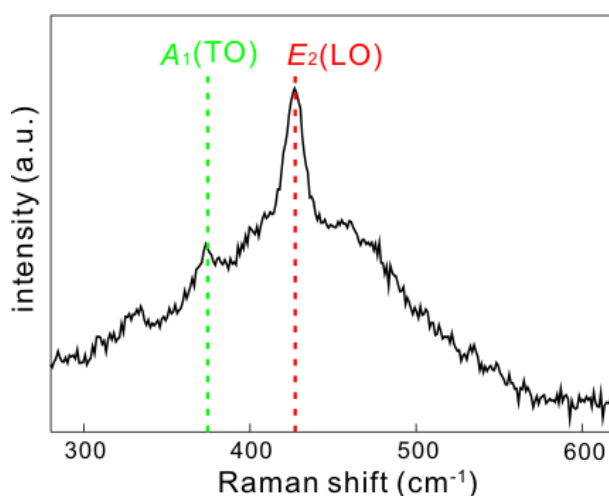
Figure 3-3 Raman spectrum of ordered ZnO nanowire arrays grown on Zn foil.

planes of the hexagonal wurtzite growth of a ZnO nanowire was along the [0001] direction.[7,14,22] This preferential [0001] growth of ZnO nanowires on Zn foil is also described with a HRXRD pattern (see below). The hexagonal wurtzite crystal structure of ZnO consists of polar (0001) and (000–1) planes and nonpolar (1000) planes with C_{6v} symmetry.[20] Due to its anisotropic crystal structure, the c-axis is the most preferred growth orientation, and growth velocities (V) in different directions under hydrothermal conditions are V [0001] > V [0110] > V [1000].[23,24] The Raman spectrum of Figure 3-3 also suggests that ZnO nanowires have been highly oriented to the c-axis because the

54

intensity of the E_2 LO mode at 438 cm^{-1} is much stronger than that of the A_1 TO mode at 378 cm^{-1}.[20,25] All the average *d*-spacing values calculated from the FFT diffraction spots in Figure 3-1d agree well with the individual standard interplanar distances of the hexagonal wurtzite ZnO crystal. Consequently, both the HRTEM image and the FFT pattern of Figure 3-1 suggest that the nanowire has been directly fabricated on Zn foil hydrothermally to show the single-crystalline structure of the hexagonal wurtzite ZnO. As shown in Figure 3-4, oriented structures of ZnO nanowires were not found in early stages of crystal growth. After 3 h, ZnO nanowires were observed although they were not well aligned yet. As randomly arrayed ZnO nanowires grew further, they began to align
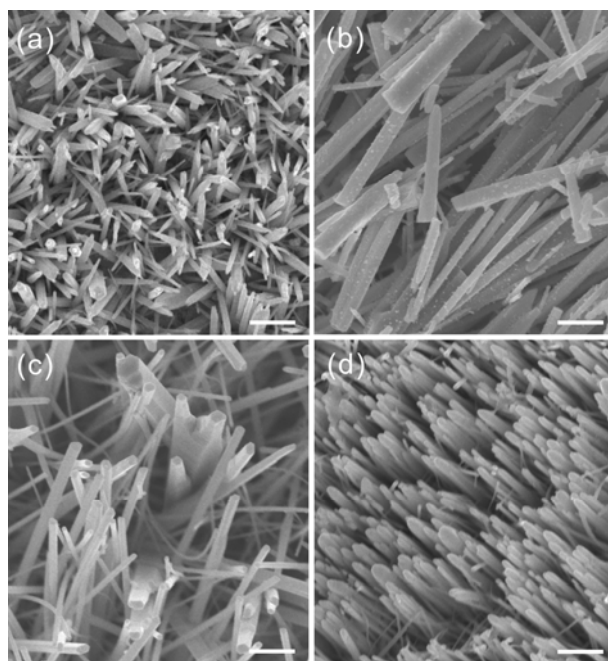
Figure 3-4 SEM images of ZnO nanostructures grown on Zn foil at 180 °C for (a) 1 h, (b) 2 h, (c) 3 h, and (d) 6 h. Each scale bar indicates 1 μm.

physically to yield well-ordered arrays on Zn foil. Comparing Figure 3-1a with Figure 3-5, we note that the average diameter of ZnO nanowires decreased with the increment of

V(H_2O)/V($N_2H_4 \cdot H_2O$), whereas the mean length of ZnO nanowires increased with the increment of V(H_2O)/V($N_2H_4 \cdot H_2O$).
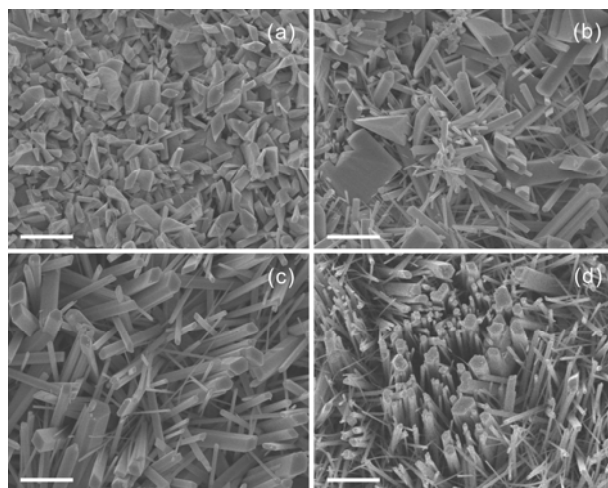
Figure 3-5 SEM images of ZnO nanostructures grown on Zn foil at 180 °C for 6 h using V(H_2O)/ V($N_2H_4 \cdot H_2O$) ratios of (a) 0.25, (b) 0.5, (c) 1.0, and (d) 2.0. Each scale bar indicates 1 μm.

The HRXRD patterns of Figure 3-6 show that our fabricated nanowires have single-crystalline structures of the hexagonal wurtzite ZnO with lattice constants of a = 3.249 Å and c = 5.207 Å (JCPDS Card No. 36–1451). The HRXRD pattern of Zn (JCPDS Card No. 04–0831) foil is also shown as a substrate for ZnO nanowire arrays. A strong diffraction peak corresponding to the (002) crystal plane of our ZnO nanowires reveals that the most preferred growth orientation of a ZnO nanowire is along the *c*-axis of the wurtzite ZnO crystal. The ZnO nanowires were well grown along the [0001] direction following the crystal orientation of the *c*-axis. The crystalline quality of ZnO can be evaluated by the full width at the half maximum (FWHM) of the (002) peak at 2θ of 34.5˚.

The FWHM is as small as 0.18°. The mean crystallite diameter, which can be determined from the line width of a HRXRD spectrum by the Scherrer's relation,[26–29] of small nanoparticles in a ZnO nanowire has been estimated to be 48 nm. The degree of orientation can be illustrated by the relative texture coefficient of TC_{002},[23,30,31] which is the relative texture coefficient of the (002) diffraction peak over the (100) diffraction peak. Although the TC_{002} of ZnO materials with random crystallographic orientation is 0.5, TC_{002} of our well-ordered ZnO nanowire arrays was measured to be 0.91. This suggests that our ZnO nanostructures are hexagonal wurtzite ZnO nanowires with preferable *c*-orientation.[23]
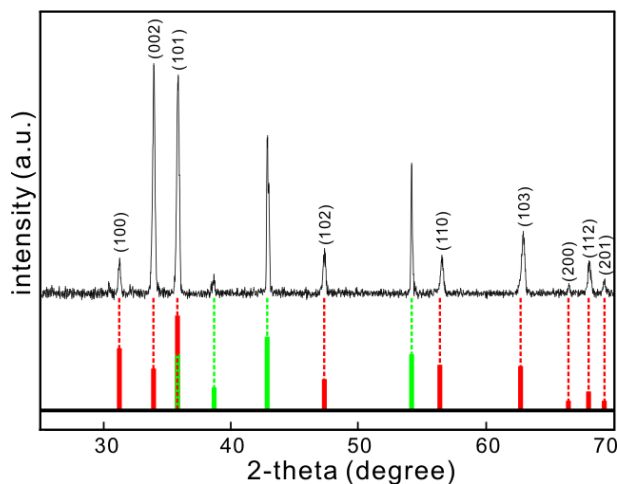
Figure 3-6 HRXRD pattern of (black) ordered ZnO nanowire arrays grown on Zn foil, (red) reference hexagonal wurtzite ZnO, and (green) reference hexagonal Zn.

The XPS spectra of Figure 3-7 can provide further significant information about the quality and surface composition of the nanowires. Binding were corrected for specimen charging, through referencing the C 1s to 285.0 eV. Although the main peak in O 1s has an asymmetric line shape, the binding energies of O 1s and Zn 2p$_{3/2}$ were identified at

57

531.5 and 1023.4 eV, respectively. The signal at 989.6 eV can be attributed to the kinetic energy of Zn LMM. The Auger parameter, which was derived from the binding energy of Zn $2p_{3/2}$ and the kinetic energy of Zn LMM, is approximately 2013.0 eV, and can be used to compare each other's results of different XPS studies reliably because it is independent of the calibration accuracy of the binding energy scale.[26,32] The Gaussian fitting of the O 1s XPS spectrum yields two distinct peaks at 529.8 and 531.4 eV. The dominant lower-energy peak arises from O–Zn bonds, related to O^{2-} ions in the wurtzite structure of the
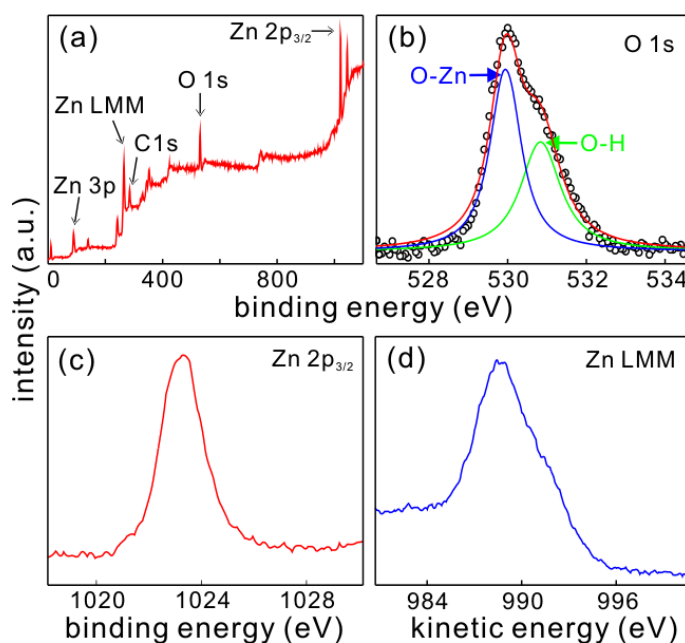
Figure 3-7 (a) Survey, (b) O 1s, (c) Zn $2p_{3/2}$, and (d) Zn LMM XPS spectra of ordered ZnO nanowire arrays grown on Zn foil.

hexagonal ZnO array, while the higher-energy peak, which is supported by the 1:1.2 atomic molar ratio of Zn:O from the EDX profile of Figure 3-2, originates from O–H bonds, related to $Zn(OH)_4^{2-}$ or OH^- ions on the surface of ZnO nanowire arrays.[33,34] Hydrazine hydrate in an aqueous solution dissociates according to the following reaction:[26,35]

$$N_2H_4 \cdot H_2O \rightarrow N_2H_5{}^+ + OH^- \tag{1}$$

and the growth of ZnO nanowires from Zn foil as a reactant can be also represented simply by the following reactions:[7,36]

$$Zn + 2H_2O + 2OH^- \rightarrow Zn(OH)_4{}^{2-} + H_2 \tag{2}$$

$$Zn(OH)_4{}^{2-} \rightarrow ZnO + H_2O + 2OH^- \tag{3}$$
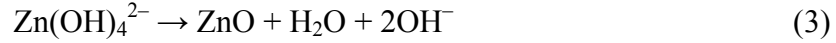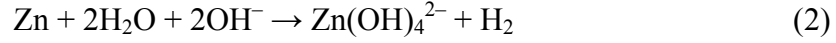
The formation of a hexagonal wurtzite ZnO nanowire may be due to the hydrothermal reaction of Zn^{2+} under an alkaline solution.[7] Particularly, a suitable concentration of $Zn(OH)_4{}^{2-}$ ions has been reported to play a key role in the fabrication of 1D ZnO nanostructures.[7,17,36] The primary ZnO nanoparticles begin to nucleate on Zn foil because the dissolution of Zn atoms into a solution causes a concentration gradient of Zn^{2+} from Zn foil. The intrinsic electric fields of the polar ZnO lattice could be responsible for the further growth of the ZnO crystals. The ZnO crystal lattice can be described as alternating planes composed of Zn^{2+} and O^{2-}, which are stacked along the c-axis. The oppositely charged ions produce positively charged Zn (0001) and negatively charged O (000-1) surfaces, resulting in polarization along the c-axis.[23,35–37] The preferred c-axis orientation of ZnO nanostructures is driven by electrostatic interactions between the polar charges to minimize the surface energy.

The UV–vis reflectance and the photoluminescence spectra of the as-prepared ZnO nanowire arrays on Zn foil (Figure 3-8) display band-gap absorption and emission bands, respectively. The maxima of the reflectance absorption and the photoluminescence spectra of arrayed ZnO nanowires are at 374.5 and 384.7 nm, respectively. Thus, the

band-gap energy of arrayed ZnO nanowires is very similar to that of bulk ZnO (3.37 eV) because the average diameter of ZnO nanowires is as large as 80 nm. The photoluminescence spectrum consists of a single spontaneous emission band with a FWHM of 14.0 nm. This spontaneous emission is generally ascribed to the recombination of excitons through an exciton-exciton scattering process.[12–14,22] Green emission from 450 nm to 600 nm was negligible, indicating that the crystal quality of our ZnO samples is high (Figure 3-9).[6,38] Figure 3-9 also indicates that photoluminescence arises totally from arrayed ZnO nanowires because the photoluminescence of Zn foil is completely absent.
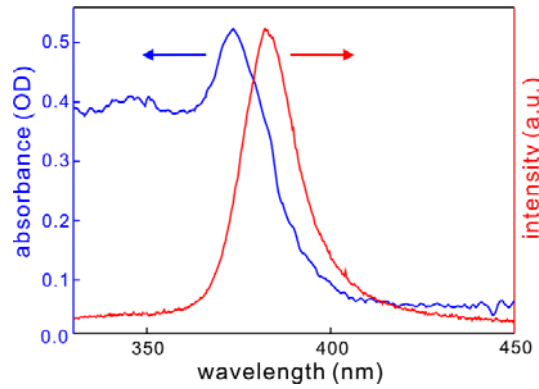
Figure 3-8 (blue) Absorption and (red) photoluminescence (with excitation at 266 nm) spectra of ordered ZnO nanowire arrays grown on Zn foil.
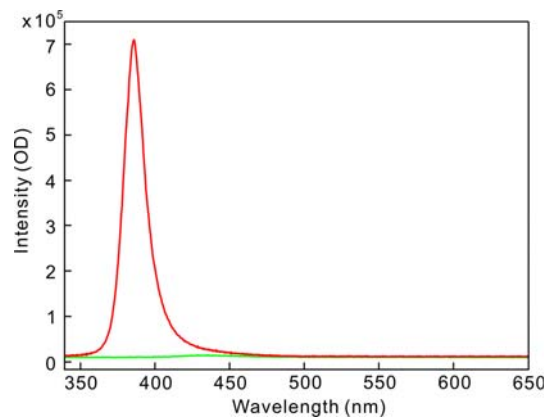
Figure 3-9 Photoluminescence spectra of (red) ordered ZnO nanowire arrays on Zn foil and (green) bare Zn foil, with excitation at 266 nm.

The I_{ex}–dependent photoluminescence of Figure 3-10 has been measured at room temperature to explore the stimulated emission of well-ordered ZnO nanowire arrays. As I_{ex} increased, the photoluminescence broadened due to the formation of electron-hole plasma and it shifted to the red with increasing intensity. As I_{ex} increased from 4 to 100 kW cm^{-2}, the photoluminescence increased dramatically (Figure 3-10a). According to the typical lasing behavior, photoluminescence intensity increases linearly below I_{th}, but increases nonlinearly beyond I_{th}.[11–14,38,39] The I_{th} of our well-ordered ZnO nanowire arrays has been determined as 25 kW cm^{-2}, indicating that the first stimulated emission due to the exciton-exciton scattering process could be generated beyond I_{th}. Our observed I_{th} is quite low compared with reported values for ZnO nanorod arrays,[12,14] while admitting that I_{th} also depends on the excitation source as well as on the size distribution of ZnO nanowires. The photoluminescence spectrum of Figure 3-10b at $4I_{th}$ (100 kW cm^{-2}) shows the second stimulated emission owing to the electron-hole plasma process.[12–,38]

Observed multiple peaks of stimulated emission with a mean FWHM of 0.08 nm, which is narrower 225 times than the peak of spontaneous emission of Figure 3-10a at 100 kW cm^{-2} with the FWHM of 18.0 nm, were generated by the superposition of stimulated emission. All observed peaks exhibit different lasing/cavity modes at 370–400 nm. Lasing in ZnO nanowire arrays is attributed to cavity effects or random resonance effects.[13,14,39] In the subwavelength region, larger diameters may lead to better confinement and better quality cavities. Stimulated emission at 388.5 nm is shifted by 1.9 nm to the red than spontaneous emission at 386.6 nm of Figure 3-10a at 100 kW cm^{-2}.
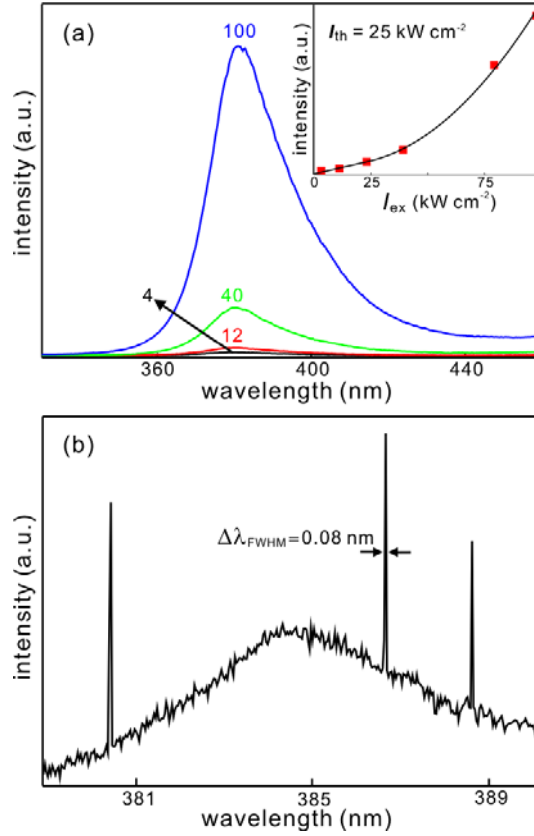
Figure 3-10 (a) I_{ex}–dependent photoluminescence spectra, excited at 266 nm and dispersed with a grating of 150 grooves mm^{-1}, of ordered ZnO nanowire arrays grown on Zn foil. Excitation irradiances are indicated inside in units of kW cm^{-2}. The fitted solid line of the inset shows that photoluminescence increases nonlinearly above I_{th} of 25 kW cm^{-2}. (b) Photoluminescence spectrum, excited at 266 nm and dispersed with a grating of 1200 grooves mm^{-1}, of ordered ZnO nanowire arrays grown on Zn foil at I_{ex} of 100 kW cm^{-2}.

This red shift could be induced by band-gap renormalization because of Coulomb interactions among amplified free carriers at the band edge through the electron-hole plasma process.[14] Light emission was collected in the direction normal to the end surface plane, along the c-axis of ZnO nanowire arrays. Excitons were generated by the round trips of transmitted light between the cleaved (0001) ends of ordered ZnO nanowires.[14] Thus, stimulated emission was finally emitted from the (0001) planes of ordered ZnO

nanowires. Optical coupling of stimulated emission could cause some complications if the packing density of ZnO nanowires was too high. Besides, stimulated emission induced from a randomly orientated ZnO medium could be interfered as a consequence of a broad FWHM of emission. Therefore, stimulated emission with a narrow FWHM should be favorable. This is why many attempts have been made to fabricate directionally grown well-defined 1D ZnO nanostructure arrays.
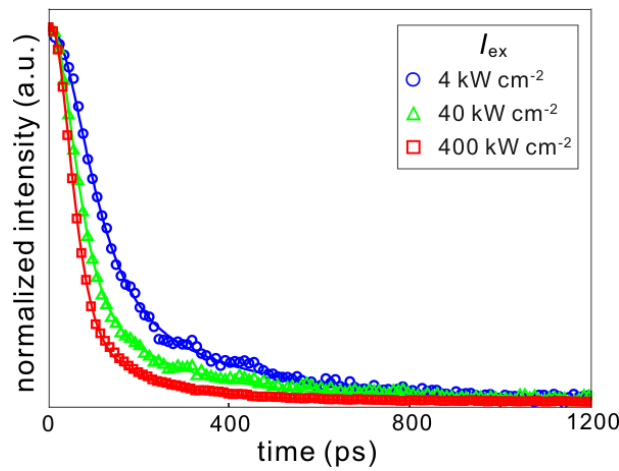
Figure 3-11 Maximum-normalized I_{ex}–dependent photoluminescence decay kinetic profiles monitored at 380 nm after excitation at 266 nm, of ordered ZnO nanowire arrays grown on Zn foil.

Figure 3-11 and Table 3-1 show that the photoluminescence of well-ordered ZnO nanowire arrays decays biexponentially and its mean lifetime decreases rapidly down to 48% with the increase of I_{ex} from 4 to 400 kW cm^{-2}. The fast decay component has been attributed to free-exciton decay while the slow one has been assigned to bound-exciton decay.[13,38] Both of these decays involve single-particle processes, thus their combination produces a two-component exponential decay. The decreased importance of the slow decay with the increase of I_{ex} is probably due to the saturation of binding sites with the increase of carrier density.[13]

The amplitude of the bound-exciton decay continues to decrease monotonically with carrier density. The slow decay time of 150 ps at 4 kW cm^{-2} decreases to 90 ps at 200 kW cm^{-2}. This decrease suggests that ZnO nanowire arrays undergo a change in the lasing mechanism from exciton-exciton scattering to electron-hole plasma recombination. Disparity between the fast lifetimes is attributed to the requirement of population inversion for stimulated emission to occur, which cannot be sustained after the initial cascade of electron-hole plasma recombination induced by the stimulated emission process.[13,39]

Table 3-1 Photoluminescence decay kinetic constants of ordered ZnO nanowire arrays on Zn foil.

I_{ex} /kW cm^{-2}	Lifetime/ps	Mean lifetime/ps
4	32 (85%) + 150 (15%)[a]	50
40	23 (91%) + 135 (9%)	33
200	20 (90%) + 90 (10%)	27
400	20 (94%) + 90 (6%)	24

[a] Initial intensity percentage of each component. Photoluminescence was monitored at 380 nm after excitation at 266 nm.

3. 5. Conclusions

In summary, well-ordered arrays of hexagonal wurtzite ZnO nanowires were hydrothermally grown directly on Zn foil and employed for room temperature UV nanolasers. The relative texture coefficient of the (002) diffraction peak over the (100) diffraction peak was measured to be 0.91, suggesting that ZnO nanowires were grown along the [0001] direction following the crystal orientation of the c-axis. A suitable concentration of $Zn(OH)_4^{2-}$ ions played a key role for the growth of 1D ZnO nanowire arrays on Zn foil. The UV lasing action of arrayed ZnO Nanowires was observed at 370–400 nm with I_{th} of 25 kW cm^{-2}, which was much lower than reported values for ZnO nanorod arrays. Observed peaks of stimulated emission had a narrow mean FWHM of 0.08 nm. Photoluminescence decays biexponentially: the fast component is attributed to free-exciton decay, and the slow one is to bound-exciton decay. The amplitude of the fast component increases whereas its lifetime decreases with the increment of Iex, suggesting that ZnO nanowire arrays undergo a change in the lasing mechanism from exciton–exciton scattering to electron–hole plasma recombination.

3. 6. Acknowledgment

3. 7. References

[1] Z. R. Tian, J. A. Voigt, J. Liu, B. McKenzie, M. J. McDermott, M. A. Rodriguez, H. Konishi, H. F. Xu, *Nat. Mater.* **2003**, *2*, 821.

[2] J.-Y. Kim, S. Lee, K.-H. Yoo, D.-J. Jang, *Appl. Phys. Lett.* **2009**, *94*, 153301.

[3] M. R. Kim, S.-Y. Park, D.-J. Jang, *Adv. Funct. Mater.* **2009**, *19*, 3910.

[4] C. F. Pan, J. Zhu, *J. Mater. Chem.* **2009**, *19*, 869.

[5] Y. N. Xia, P. D. Yang, Y. G. Sun, Y. Y. Wu, B. Mayers, B. Gates, Y. D. Yin, F. Kim, H. Q. Yan, *Adv. Mater.* **2003**, *15*, 353.

[6] E.-S. Jang, X. Y. Chen, J.-H. Won, J.-H. Chung, D.-J. Jang, Y.-W. Kim, J.-H. Choy, *Appl. Phys. Lett.* **2010**, *97*, 043109.

[7] J. Lee, M. Yoon, *J. Phys. Chem. C* **2009**, *113*, 11952.

[8] S. Nakamura, *Science* **1998**, *281*, 956.

[9] W.-S. Chae, J.-H. Yoon, H. Yu, D.-J. Jang, Y.-R. Kim, *J. Phys. Chem. B* **2004**, *108*, 11509.

[10] A. Mohanta, R. K. Thareja, *J. Appl. Phys.* **2008**, *104*, 044906.

[11] P. D. Yang, H. Q. Yan, S. Mao, R. Russo, J. Johnson, R. Saykally, N. Morris, J. Pham, R. R. He, H.-J. Choi, *Adv. Funct. Mater.* **2002**, *12*, 323.

[12] M. H. Huang, S. Mao, H. Feick, H. Q. Yan, Y. Y. Wu, H. Kind, E. Weber, R. Russo, P. D. Yang, *Science* **2001**, *292*, 1897.

[13] J. C. Johnson, K. P. Knutsen, H. Q. Yan, M. Law, Y. F. Zhang, P. D. Yang, R. J. Saykally, *Nano Lett.* **2004**, *4*, 197.

[14] J.-H. Choy, E.-S. Jang, J.-H. Won, J.-H. Chung, D.-J. Jang, Y.-W. Kim, *Adv. Mater.* **2003**, *15*, 1911.

[15] Z. T. Zhu, L. F. Zhang, J. Y. Howe, Y. L. Liao, J. T. Speidel, S. Smith, H. Fong, *Chem. Commun.* **2009**, 2568.

[16] X.-L. Yu, J.-G. Song, Y.-S. Fu, Y. Xie, X. Song, J. Sun, X.-W. Du, *J. Phys. Chem. C* **2010**, *114*, 2380.

[17] S. S. Warule, N. S. Chaudhari, B. B. Kale, M. A. More, *CrystEngComm* **2009**, *11*, 2776.

[18] Y.-Z. Zheng, X. Tao, L.-X. Wang, H. Xu, Q. Hou, W.-L. Zhou, J.-F. Chen, *Chem. Mater.* **2010**, *22*, 928.

[19] W. Z. Wang, B. Q. Zeng, J. Yang, B. Poudel, J. Y. Huang, M. J. Naughton, Z. F. Ren, *Adv. Mater.* **2006**, *18*, 3275.

[20] Y. Zhang, H. B. Jia, R. M. Wang, C. P. Chen, X. H. Luo, D. P. Yu, C. Lee, *Appl. Phys. Lett.* **2003**, *83*, 4631.

[21] L. Vayssieres, *Adv. Mater.* **2003**, *15*, 464.

[22] J.-H. Choy, E.-S. Jang, J.-H. Won, J.-H. Chung, D.-J. Jang, Y.-W. Kim, *Appl. Phys. Lett.* **2004**, *84*, 287.

[23] H. Q. Yang, Y. Z. Song, L. Li, J. H. Ma, D. C. Chen, S. L. Mai, H. Zhao, *Cryst. Growth Des.* **2008**, *8*, 1039.

[24] M. Wang, C.-H. Ye, Y. Zhang, G.-M. Hua, H.-X. Wang, M.-G. Kong, L.-D. Zhang, *J. Cryst. Growth.* **2006**, *291*, 334.

[25] M. Lucas, Z. L. Wang, E. Riedo, *Appl. Phys. Lett.* **2009**, *95*, 051904.

[26] J.-Y. Kim, M. R. Kim, S.-Y. Park, D.-J. Jang, *CrystEngComm* **2010**, *12*, 1803.

[27] D. Routkevitch, T. Bigioni, M. Moskovits, J. M. Xu, *J. Phys. Chem.* **1996**, *100*, 14037.

[28] Y. Ni, H. Hao, X. Cao, S. Su, Y. Zhang, X. Wei, *J. Phys. Chem. B* **2006**, *110*, 17347.

[29] M. R. Kim, D.-J. Jang, *Chem. Commun.* **2008**, 5218.

[30] J. G. Lu, Z. Z. Ye, J. Y. Huang, L. Wang, B. H. Zhao, *Appl. Surf. Sci.* **2003**, *207*, 295.

[31] H. Z. Zhang, X. C. Sun, R. M. Wang, D. P. Yu, *J. Cryst. Growth.* **2004**, *269*, 464.

[32] A. Nayak, H. D. Banerjee, *Appl. Surf. Sci.* **1999**, *148*, 205.

[33] K. Ogata, K. Koike, S. Sasa, M. Inoue, M. Yano, *Appl. Surf. Sci.* **2008**, *254*, 7708.

[34] M. Chen, X. Wang, Y. H. Yu, Z. L. Pei, X. D. Bai, C. Sun, R. F. Huang, L. S. Wen, *Appl. Surf. Sci.* **2000**, *158*, 134.

[35] J. Du, L. Q. Xu, G. F. Zou, L. L. Chai, Y. T. Qian, *Mater. Chem. Phys.* **2007**, *103*, 441.

[36] Z. H. Li, Y. X. Luan, Q. Z. Wang, G. S. Zhuang, Y. X. Qi, Y. Wang, C. G. Wang, *Chem. Commun.* **2009**, 6273.

[37] K. Ogata, K. Koike, S. Sasa, M. Inoue, M. Yano, *Semicond. Sci. Tech.* **2009**, *24*, 015006.

[38] X. H. Han, G. Z. Wang, Q. T. Wang, L. Cao, R. B. Liu, B. S. Zou, J. G. Hou, *Appl. Phys. Lett.* **2005**, *86*, 223106.

[39] H. J. Zhou, M. Wissinger, J. Fallert, R. Hauschild, F. Stelzl, C. Klingshirn, H. Kalt, *Appl. Phys. Lett.* **2007**, *91*, 181112.

Chapter 4. Annealing-Free Preparation of Anatase TiO$_2$ Nanopopcorns on Ti Foil via a Hydrothermal Process: Photocatalytic and Photovoltaic Applications

4. 1. Abstract

Uniform and well-defined nanopopcorns of the tetragonal anatase TiO_2 having an average diameter of 670 nm have been facilely grown on Ti foil via a hydrothermal method and characterized by analyzing electron microscopic images and electron diffraction patterns as well as X-ray photoelectron, photoluminescence, and Raman spectra. The morphology of TiO_2 nanostructures on Ti foil has been controlled well by adjusting the volume ratio of H_2O_2: HF: H_2O, $VR(H_2O_2:HF:H_2O)$. Truncated tetragonal pyramidal TiO_2 nanocrystals exposing the {001} and {101} facets have grown on the surface of TiO_2 nanostructures exposing the {001} facets to produce anatase TiO_2 nanopopcorns. Without being treated via any annealing process, our well-defined TiO_2 nanopopcorns on Ti foil have been directly employed for photocatalytic materials and dye-sensitized solar cells. Among our prepared samples, anatase TiO_2 nanopopcorns grown on Ti foil at $VR(H_2O_2:HF:H_2O)$ of 1:1:1000 have shown the most reduced oxygen vacancy luminescence, the highest photocatalytic activity for the degradation of methylene blue, and the highest photovoltaic conversion efficiency of 3.98% as the working electrode of a dye-sensitized solar cell.

4. 2. Introduction

Nanostructured semiconductors having unique spectroscopic, electronic, and chemical properties have been extensively investigated because of their applications in fields of catalysts, optoelectronics, and transistors.[1–4] In particular, titania (TiO_2) having a wide band gap (3.2 eV) has been received attention as a promising nanomaterial to generate electricity, produce renewable solar hydrogen, and remediate aqueous pollutants.[5–8] Although new catalytic materials working in the ultraviolet (UV) or visible light region have been studied remarkably, TiO_2-based nanomaterials are still considered to be one of superior photocatalysts.[9–12] The basic principle of semiconductor photocatalysis involves the absorption of a photon which leads to electron–hole pair formation.[2,11–14] The electron–hole pairs can migrate toward the catalyst surface and initiate redox reactions in which adsorbed organic molecules are oxidized, or they may undergo undesirable recombination. In order to prevent electron-hole recombination, a highly active photocatalyst should have a high degree of crystallinity.[5,15–18] TiO_2 nanostructures have also attracted great attention as nanomaterials employed to make an electrode of dye-sensitized solar cells (DSSCs) although the highest power conversion efficiency of DSSCs has been reported as about 12% due to poor utilization of near infrared light and high recombination of electron–hole pairs in the random network of TiO_2 nanomaterials.[19–23] Single-crystalline and hierarchical rutile TiO_2 nanostructures on fluorine-doped tin oxide (FTO) glass have been reported to show a power conversion efficiency of 1–4% in DSSC applications.[24,25] However, these nanowire or

hierarchical arrays were grown on rigid FTO glass substrates which limited applications in flexible electronic devices. Furthermore, it is well known that the rutile TiO_2 exhibits an inferior photovoltaic performance because of less dye loading and slower electron transport compared with anatase TiO_2 nanostructures.[8,23] Thus, it would be very desirable to synthesize anatase TiO_2 nanostructures facilely to enhance the photovoltaic performance of DSSCs.

Considerable efforts have been devoted to the preparation of high-quality TiO_2 nanomaterials for applications in photocatalytic materials and photovoltaic cells. Diverse methods such as chemical vapor deposition,[26] electrochemical syntheses,[27] and sol-gel techniques[15] have been successfully established to prepare anatase TiO_2 nanostructures in general. In particular, hydrothermal syntheses of anatase TiO_2 nanostructures have been found to be quite advantageous particularly from viewpoints of environmental friendliness, easy upward scaling, and low production cost.[28–30] Although anatase TiO_2 nanocrystals with being treated via a high-temperature post-annealing process have been employed as photocatalytic or photovoltaic materials,[15–17,31] the hydrothermal synthesis of anatase TiO_2 nanostructures on Ti foil without being treated via any post-annealing process has been hardly reported yet. In addition, the direct photocatalytic and photovoltaic applications of anatase TiO_2 nanopopcorns on Ti foil have not been reported although ZnO nanowires grown on FTO glass[4] or TiO_2 nanowires grown on Ti foil[21] have been utilized in DSSCs.

In this paper, we report the facile one-pot hydrothermal preparation of anatase TiO_2 nanopopcorns on Ti foil to be employed for photocatalytic and photovoltaic materials directly

72

without being treated via any additional annealing process. We have controlled the growth of tetragonal anatase TiO_2 nanopopcorns on Ti foil hydrothermally by changing the volume ratio of H_2O_2: HF: H_2O, VR(H_2O_2:HF:H_2O). The anatase TiO_2 has two low energy surfaces, (101) and (001), which are common for natural crystals.[2,32] Truncated tetragonal pyramidal TiO_2 nanocrystals exposing the {001} and {101} facets have been grown on the (001) surfaces of TiO_2 nanostructures to form anatase TiO_2 nanopopcorns. Anatase TiO_2 crystals exposing the {001} facets have been prepared by using various raw materials such as TiF_4,[33] $TiCl_4$,[34] $Ti[O(CH_2)_3CH_3]_4$,[30] and $Ti[OCH(CH_3)_2]_4$[35] to stabilize the {001} facets. However, the processes employing these raw materials require high temperature, interrupt scaled-up production, and induce hydrolysis.[18,29] Our well-defined TiO_2 nanopopcorns exposing the {001} facets grown on Ti foil have shown high photocatalytic activitity for the degradation of methylene blue (MB) dye under UV light irradiation. Anatase TiO_2 nanopopcorns grown on Ti foil at VR(H_2O_2:HF:H_2O) of 1:1:1000 have shown the most reduced oxygen vacancy luminescence and the highest photovoltaic power conversion efficiency of 3.98%.

4. 3. Experimental Details

The analytical grade chemicals of Ti foil(s), 30% H_2O_2(aq), 49% HF(aq), H_2PtCl_6(s), LiI(s), 1-butyl-3-methylimidazolium iodide(l), guanidinium thiocyanate(l), acetonitrile(l),

methylene blue(s, MB), 4-*tert*-butylpyridine(l), and valeronitrile(l) were used as purchased from Sigma-Aldrich. While N719 dye and Surlyn (SX1170-60) were used as purchased from Solaronix, Pt-coated fluorine-doped tin oxide (FTO) glass and were used as purchased from Pilkington. Deionized water with a resistivity of greater than 18 MΩ cm from a Millipore Milli-Q system was used throughout the experiments. For the typical annealing-free preparation of anatase TiO_2 nanopopcorns on Ti foil, 20 mL of deionized water, 20 µL of 30% H_2O_2(aq), 20 µL of 49% HF(aq), and Ti foil (10 x 20 x 0.25 mm^3) were loaded into a Teflon-lined stainless-steel autoclave of 50 mL capacity. The autoclave was placed in an oven at 180 ºC for 6 h and then cooled to room temperature. The Ti foil was removed from the solution and rinsed with deionized water to get rid of residual impurities. We have found the above described optimal conditions for the synthesis of anatase TiO_2 nanopopcorns on Ti foil after we tried diverse experimental conditions. The photocatalytic activities of various concentrations of anatase TiO_2 nanopopcorns were evaluated by performing MB degradation experiments under the irradiation of 75 W xenon lamp. For dye adsorption, the working electrode of TiO_2 nanopopcorns grown on Ti foil was immersed in anhydrous ethanol containing 0.5 mM N719 dye,[47] and kept at room temperature for 24 h. The counter electrode was prepared by dropping 60 µL of a 0.5 mM H_2PtCl_6 solution on an FTO glass (8 Ω/sq) followed by being heated at 400 ºC for 20 min in air. Then, the working electrode of TiO_2 nanopopcorns on Ti foil and the counter electrode were placed to face each other and the mutual distance was controlled to 60 µm by using Surlyn. The transmittance of Pt-coated FTO was 72% at 500 nm. The electrolyte consisted of 0.6 M 1-butyl-3-methylimidazolium

iodide, 0.03 M I_2, 0.1 M guanidinium thiocyanate, 0.4 M LiI, and 0.5 M *tert*-butylpyridine in (85:15 *v/v*) acetonitrile and valeronitrile.[22,48] The active area of the dye-coated TiO_2 film was 0.210 cm^2.

While transmission electron microscopy (TEM) images were obtained with a Hitachi H-7600 microscope, high-resolution transmission electron microscopy (HRTEM) images and selected-area electron diffraction (SAED) patterns were measured using a JEOL JEM-3000F microscope. Scanning electron microscopy (SEM) images was recorded with a JEOL JSM-6700F microscope, and high-resolution X-ray diffraction (HRXRD) patterns were obtained with a Bruker D8 DISCOVER diffractometer using Cu K radiation ($\lambda = 0.15418$ nm). X-ray photoelectron spectroscopy (XPS) was monitored using a Sigma Probe ThermoVG spectrometer with an excitation source of Al K = 1486.6 eV. Whereas Raman spectra were measured using a HORIABA Jobin Yvon T64000 equipped with an Ar^+ laser as the excitation source, photoluminescence spectra were measured employing a Princeton Instruments ICCD576G CCD detector with excitation of 266 nm pulses from a Q-switched Quantel Brilliant Nd:YAG laser of 6 ns. Photocurrent-voltage (*I–V*) measurements were performed using a Keithley model 2400 source measurement unit. A 300 W xenon lamp (Oriel Instruments) was used as the light source to irradiate the counter electrode side of the fabricated dye-sensitized solar cell. The light intensity was adjusted using an NREL-calibrated Si solar cell equipped with a KG-5 filter to be AM 1.5G one sun light intensity approximately.

4. 4. Results and Discussion

The TEM image of Figure 4-1a shows that TiO_2 nanopopcorns having an average diameter of 670 nm have been grown directly on Ti foil. Truncated tetragonal pyramidal TiO_2 nanocrystals have been grown on the surface of initial tetragonal bipyramidal TiO_2 nanoparticles to form TiO_2 nanopopcorns (see below). The microstructural details of the anatase TiO_2 nanopopcorn have been further provided by measuring the HRTEM image of Figure 4-1b and the SAED pattern of Figure 4-1c. The observed lattice-fringe distances of 0.352 and 0.238 nm in Figure 4-1b correspond to the spacings of 0.351 and 0.238 nm between the (101) planes and the (004) planes, respectively, of the tetragonal anatase TiO_2 (JCPDS Card No. 04-0477). The average d-spacing values of 0.352 and 0.240 nm observed from the SAED pattern of Figure 4-1c also agree reasonably with the standard spacings of 0.351 and 0.238 nm between the (101) planes and the (004) planes, respectively, of the tetragonal anatase TiO_2 crystal. Consequently, both the HRTEM image of Figure 4-1b and the SAED pattern of Figure 4-1c suggest that the nanopopcorn directly fabricated on Ti foil hydrothermally has the single-crystalline structure of the tetragonal anatase TiO_2. The observed (101) and (004) planes of the anatase TiO_2 nanopopcorn in Figure 4-1b are dominant in {101} and {001} facets, respectively. It has been reported that the {001} facets are especially reactive for anatase TiO_2 nanoparticles as the order of the average surface energies is $\gamma\{001\}$ (0.90 J m^{-2}) > $\gamma\{100\}$ (0.53 J m^{-2}) > $\gamma\{101\}$ (0.44 J m^{-2}).[28,36] Although anatase TiO_2 nanoparticles exposing (001) planes have hardly been observed due to the

minimization of the surface energy during a crystal growth process,[2,35] the TiO_2 nanopopcorn of Figure 4-1b and c displays the (004) planes as well.
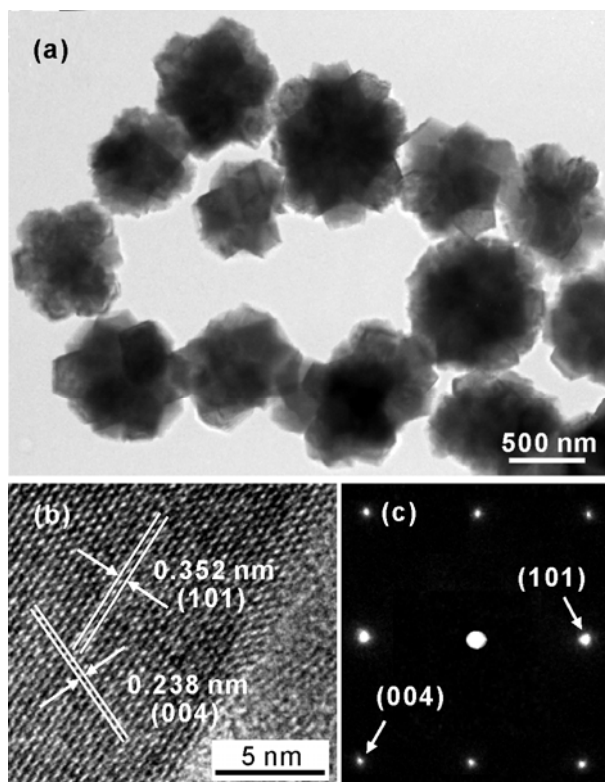
Figure 4-1 (a) TEM image of TiO_2 nanopopcorns. (b) HRTEM image, showing a lattice-plane distance, and (c) SAED pattern, with indication of a (101) lattice plane, of an anatase TiO_2 nanopopcorn.

The SEM images of Figure 4-2 show that the morphology of TiO_2 nanoparticles grown directly on Ti foil at 180 ºC for 6 h changes with the increase of the content of HF. Comparing the SEM images of Figure 4-2 each other, we note that truncated tetragonal pyramidal TiO_2 nanocrystals have grown hierarchically on the surface of initial tetragonal bipyramidal TiO_2 nanostructures gradually with the increase of the content of HF to form TiO_2 nanopopcorns without changing the sizes of the initial nanostructures largely. Typical TiO_2 nanopopcorns grown on Ti foil at $VR(H_2O_2:HF:H_2O)$ of 1:1:1000 have an average

diameter of 670 nm with the lengths of the truncated tetragonal pyramidal TiO_2 nanocrystals in the range of 30 to 70 nm. HF has been considered to play a crucial role in the formation of TiO_2 under hydrothermal conditions.[29,33,37] HF dissolves Ti foil to produce a Ti precursor, retards the hydrolysis of the Ti precursor, and reduces the surface energy of TiO_2 nanostructures. Theoretical calculations indicate that F^- ions can reduce the surface energy of the {001} facets of the anatase TiO_2 to a level lower than that of the {101} facets.[30,33] Ti^{4+}

Figure 4-2 SEM images of TiO_2 nanopopcorns grown on Ti foil with $VR(H_2O_2{:}HF{:}H_2O)$ of (a) 1:0.5:1000, (b) 1:1:1000, (c) 1:2.5:1000, and (d) 1:5:1000. Each scale bar indicates 500 nm.

ions can react with H_2O_2 to form a dinuclear complex, $Ti_2O_5(OH)_x^{(2-x)}$ (x = 1–6),[38,39] which

may further retard the hydrolysis of the Ti precursor. The comparatively slow hydrolysis rate could provide adequate time for the formation of the Ti–O chains to grow anatase single crystals and induce F$^-$ ions to absorb on the surface of the TiO$_2$ crystals, reducing the surface energy.[28–30,33,40] On the other hand, the SEM images of Figure 4-3 show that TiO$_2$ nanopopcorns grown directly on Ti foil at 180 ºC for 6 h are growth of truncated tetragonal pyramidal TiO$_2$ nanocrystals on the surface of initial uniform in size and morphology regardless of the content of H$_2$O$_2$. This suggests that the tetragonal bipyramidal TiO$_2$ nanostructures are more sensitive to the amount of HF than that of H$_2$O$_2$.
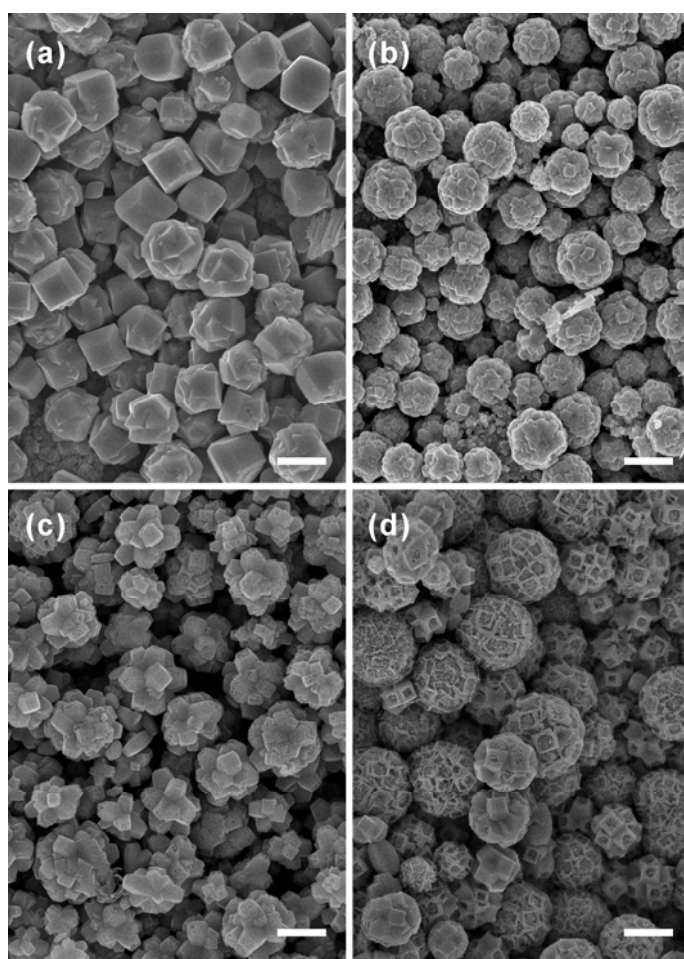

Figure 4-3 SEM images of TiO$_2$ nanopopcorns grown on Ti foil with VR(H$_2$O$_2$:HF:H$_2$O) of (a) 0.5:1:1000, (b) 1:1:1000, (c) 2.5:1:1000, and (d) 5:1:1000. Each scale bar indicates 500 nm.

The HRXRD patterns in Figure 4-4 of TiO$_2$ nanostructures grown directly on Ti foil at various VR(H$_2$O$_2$:HF:H$_2$O) values without being treated via any additional annealing process show tetragonal anatase TiO$_2$ structures with lattice constants of a = 3.783 Å, b = 3.783 Å,

and c = 9.510 Å (JCPDS Card No. 04-0477). Note that the HRXRD patterns hardly show any peaks of the Ti phase from Ti foil. All HRXRD peaks of TiO_2 nanostructures can be indexed to the standard peaks of the anatase TiO_2 phase with showing strong preferential orientation of the {101} facets. Figure 4-4 and Figure 4-5, as well as Figure 4-2, indicate that TiO_2 nanopopcorns grown at VR(H_2O_2:HF:H_2O) of 1:1:1000 have the best-defined tetragonal anatase structure. Enhanced (101) and (004) peaks in the HRXRD patterns indicate that the {101} and {001} facets are dominant in our TiO_2 nanopopcorns grown at VR(H_2O_2:HF:H_2O) of 1:1:1000. High photocatalytic efficiency is expected for our anatase TiO_2 nanopopcorns having the {001} facets preferentially because the {001} facets are more reactive for the dissociative adsorption of reactant molecules compared with the {101} facets (see below). The {101} facets that are most abundant on the surface of bipyramidal anatase nanocrystals have been reported[2,30] to have low photoactivity since a small amount of Ti atoms are undercoordinated. Note that a large amount of Ti atoms are undercoordinated in the reactive {001} facets. The mean crystallite diameter, *d*, of nanocrystals can be determined from the line width of a HRXRD peak by using the Scherrer's formula $<d> = 0.94 \, \lambda \, / \, (B \, cos \, \theta_B)$, where λ is the X–ray wavelength, B is the full width at the half maximum of the diffraction peak (radian), and θ_B is the half angle of the diffraction peak on the 2θ scale.[41,42] The mean crystallite diameter of TiO_2 nanopopcorns grown at VR(H_2O_2:HF:H_2O) of 1:1:1000 has been estimated to be 72.6 nm by using the (101) peak at 2θ of 25.4˚.
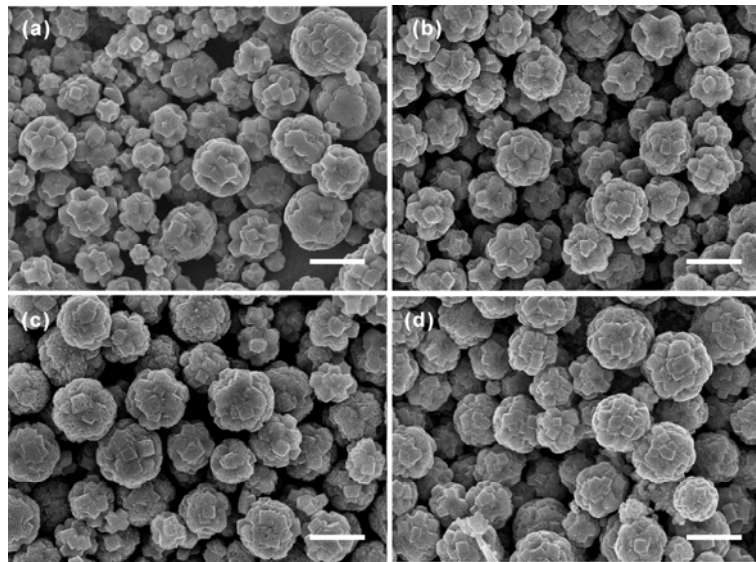
Figure 4-4 HRXRD patterns of TiO_2 nanopopcorns grown on Ti foil with $VR(H_2O_2:HF:H_2O)$ of (a) 1:0.5:1000, (b) 1:1:1000, (c) 1:2.5:1000, and (d) 1:5:1000. The standard diffraction lines of anatase TiO_2 and rutile TiO_2 are also shown for comparison.
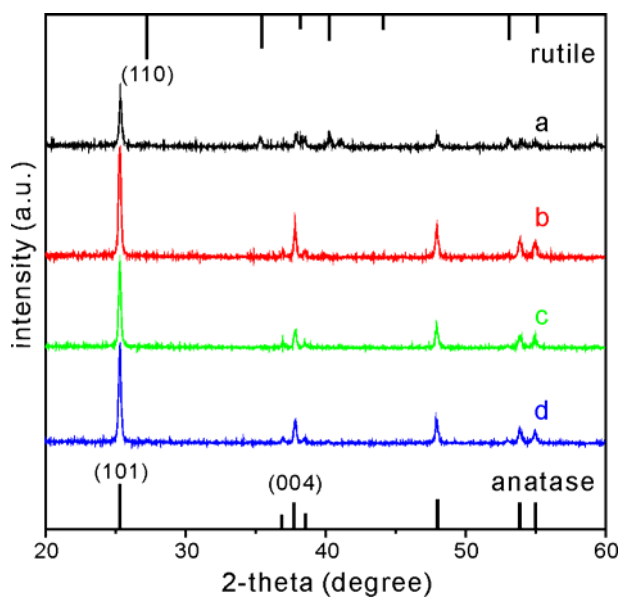
Figure 4-5 XRD patterns of TiO_2 nanopopcorns grown on Ti foil at $VR(H_2O_2:HF:H_2O)$ of (a) 0.5:1:1000, (b) 1:1:1000, (c) 1:2.5:1000, and (d) 5:1:1000. The standard diffraction lines of anatase TiO_2 and rutile TiO_2 are also shown for comparison.

Both the Raman spectra and the XPS spectra of Figure 4-6 and Figure 4-7, respectively, also support that our as- prepared TiO_2 nanopopcorns grown directly on Ti foil without being annealed have well-defined tetragonal anatase structures. All the observed six peaks arise from the standard basic Raman modes of the anatase TiO_2 phase and any peaks of the TiO_2 rutile phase could not be detected at all. It has been known[17,43] that the tetragonal anatase with two formula units per unit cell has six Raman active modes ($A_{1g}+2B_{1g}+3E_g$), whereas the tetragonal rutile with two formula units per unit cell has four Raman active modes ($A_{1g}+B_{1g}+B_{2g}+E_g$). The fact that the intensity of the $E_{g(1)}$ mode in Figure 4-6 is stronger than any other on Figure 4-6 also supports that TiO_2 nanopopcorns grown at $VR(H_2O_2:HF:H_2O)$ of 1:1:1000 have the best-defined tetragonal anatase structure. The XPS spectra can provide further significant information about the surface of TiO_2 nanopopcorns grown on Ti foil. The binding energies of the O 1s of TiO_2 nanopopcorns on Ti foil grown with $VR(H_2O_2:HF:H_2O)$ of 1:0.5:1000, 1:1:1000, 1:2.5:1000, and 1:5:1000 have been identified as 529.7, 529.2, 529.1, and 529.1 eV, respectively. The binding energy of O 1s shifts slightly to the lower energy, which is assigned to the crystal lattice oxygen in the Ti–O– of the anatase phase,[10,44] with the increase of the content of HF. However, the higher energy, which is attributed to the oxygen species of Ti–OH on the surface of TiO_2 nanostructures,[10,44,45] decreases with the increase of the content of HF. Thus, Figure 4-7 also suggests that our as-prepared TiO_2 nanopopcorns have well-defined anatase structures with a minimal amount of Ti–OH in their surface.
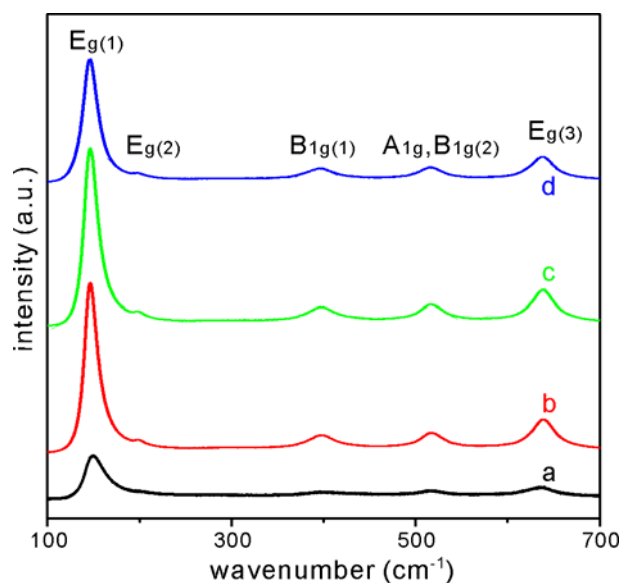
Figure 4-6 Raman spectra of TiO$_2$ nanopopcorns grown on Ti foil with VR(H$_2$O$_2$:HF:H$_2$O) of (a) 1:0.5:1000, (b) 1:1:1000, (c) 1:2.5:1000, and (d) 1:5:1000.
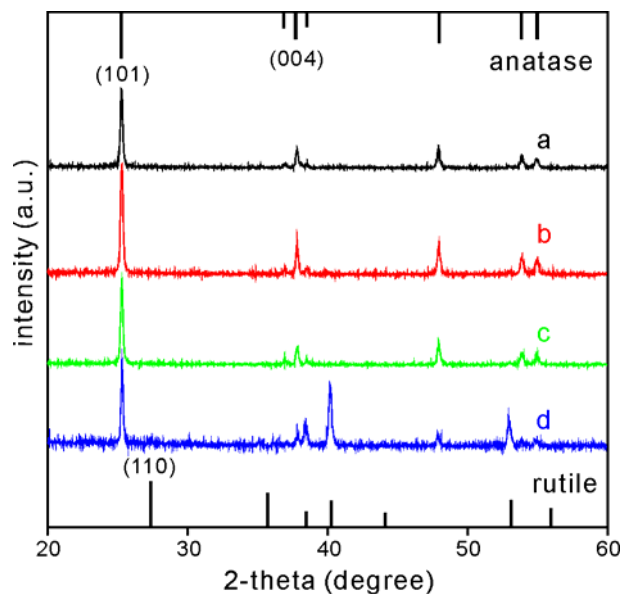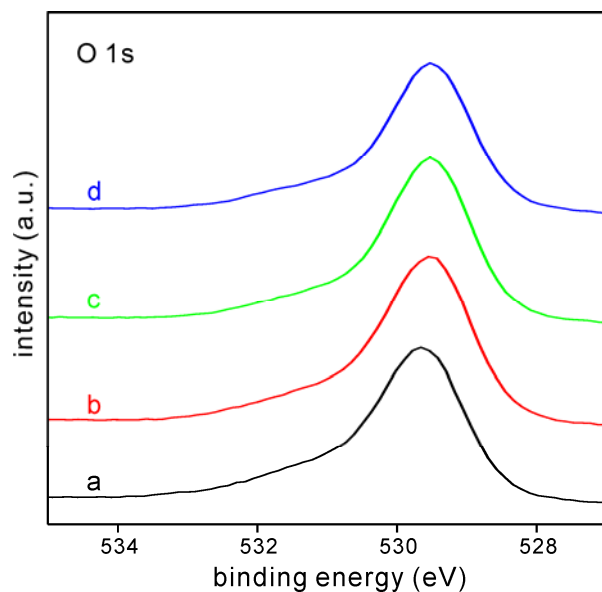

Figure 4-7 XPS spectra of the O1s of TiO$_2$ nanopopcorns grown on Ti foil with VR(H$_2$O$_2$:HF:H$_2$O) of (a) 1:0.5:1000, (b) 1:1:1000, (c) 1:2.5:1000, and (d) 1:5:1000.

Figure 4-8 shows that the photoluminescence spectrum of TiO$_2$ nanopopcorns grown at VR(H$_2$O$_2$:HF:H$_2$O) of 2.5:1:1000 is red-shifted by 10 nm from that of TiO$_2$ nanopopcorns grown at VR(H$_2$O$_2$:HF:H$_2$O) of 1:1:1000 due to the increased presence of oxygen vacancies.

The photoluminescence spectra of anatase TiO_2 nanomaterials can be considered to have three kinds of physical origins:[46] self-trapped excitons, oxygen vacancies, and surface states. The band at the long-wavelength side of the photoluminescence spectrum of anatase TiO_2 nanoparticles has been attributed to oxygen vacancies. The fact that oxygen-vacancy luminescence is weaker in the photoluminescence spectrum of Figure 4-8a than in any other spectra of Figure 4-8 supports that our TiO_2 nanopopcorns grown at $VR(H_2O_2:HF:H_2O)$ of 1:1:1000 have the best-defined anatase crystalline structure. Figure 4-9 displays that photoluminescence is weakest in TiO_2 nanopopcorns grown at $VR(H_2O_2:HF:H_2O)$ of 1:1:1000. This also suggests that our TiO_2 nanopopcorns grown at $VR(H_2O_2:HF:H_2O)$ of 1:1:1000 have the well-defined –Ti–O– network of the anatase TiO_2 with a minimal amount of trap sites and oxygen vacancies.
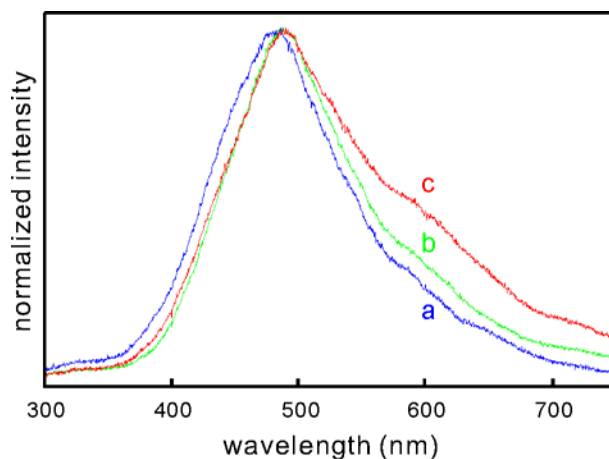
Figure 4-8 Maximum-normalized photoluminescence spectra of TiO_2 nanopopcorns grown on Ti foil with $VR(H_2O_2:HF:H_2O)$ of (a) 1:1:1000, (b) 1:2.5:1000, and (c) 2.5:1:1000. Samples were suspended in water and excited at 266 nm.
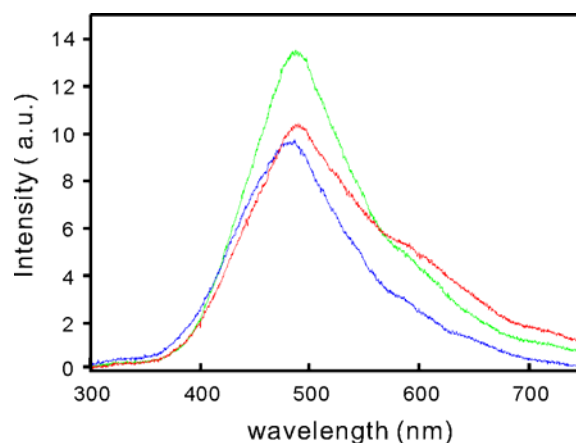
Figure 4-9 Photoluminescence spectra of TiO_2 nanopopcorns grown on Ti foil. VR(H_2O_2:HF:H_2O) were (*blue*) 1:1:1000, (*green*) 1:2.5:1000, (*red*) 2.5:1:1000, and samples were suspended in water and excited at 266 nm.

Figure 4-10 indicates that the photocatalytic degradation rate constant of MB increases sharply with the concentration of TiO_2 nanopopcorns suspended in water, suggesting that our as-prepared TiO_2 nanopopcorns have high photocatalytic activity. The photodegradation kinetic profiles of MB in Figure 4-11a and their pseudo-first-order kinetic rate plots in Figure 4-11b indicate that anatase TiO_2 nanopopcorns grown on Ti foil at VR(H_2O_2:HF:H_2O) of 1:1:1000 have the most-enhanced photocatalytic activity (see above). The photocatalytic activity of the TiO_2 nanopopcorns without being treated via any annealing process has been evaluated in terms of the degradation kinetics of MB under UV (360±5 nm) light irradiation of 0.8 mW cm^{-2} with stirring continuously. Before exposure to UV light irradiation, each sample was stirred in the dark for 90 min to allow it to reach a complete adsorption–desorption equilibrium. The linear relationship of Figure 4-11b shows that the photocatalytic degradation of MB follows the pseudo-first-order kinetics of ln (C_0/C) = kt, where C/C_0 is the
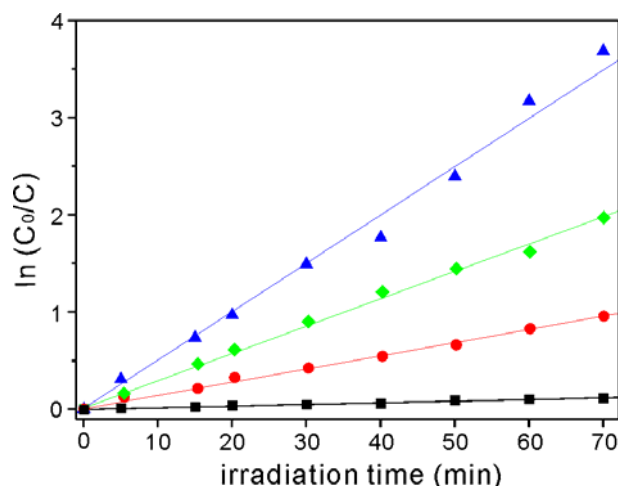
Figure 4-10 Pseudo-first-order kinetic rate plots for the photocatalytic degradation of MB (360 ppm) at different concentraions of TiO_2 nanopopcorns grown at $VR(H_2O_2:HF:H_2O)$ of 1:1:1000 on Ti foil. The suspended masses of nanopopcorns in 2 mL of water were (squares) 0.0, (circles) 1.2, (diamonds) 2.4, and (triangles) 4.8 mg. The rate constants obtained from the best-fitted lines with the nanopopcorns of 0.0, 1.2, 2.4, and 4.8 mg are 0.11, 0.96, 1.8, and 3.0 h^{-1}, respectively.

normalized MB concentration, t is the reaction time, and k is the rate constant.[8,10,12] The photodegradation rate constant in the presence of anatase TiO_2 nanopopcorns grown at $VR(H_2O_2:HF:H_2O)$ of 1:1:1000 is 3.0 h^{-1} whereas that in the absence of any TiO_2 nanopopcorns is 0.11 h^{-1}, revealing that photocatalytic rate constant of the $VR(H_2O_2:HF:H_2O)$ of 1:1:1000 is 2.9 h^{-1}. The enhanced photocatalytic activity of anatase TiO_2 nanopopcorns grown at $VR(H_2O_2:HF:H_2O)$ of 1:1:1000 can be attributed to the 3D hierarchical nanostructures and exposed {001} facets of the anatase nanopopcorns. It has been reported that 3D hierarchical nanostructures have a greater number of active sites than either 0D or 1D architectures do.[19,21,30] The {001} facets have been demonstrated to be more reactive to absorb water dissociatively to form hydrogen peroxide and peroxide radicals

86

compared with the {101} facets. Thus, the high photocatalytic activity of our TiO_2 nanopopcorns grown at VR(H_2O_2:HF:H_2O) of 1:1:1000 is considered to arise from the preferential {001} facets and the well-defined structure of the anatase TiO_2.[5,17]
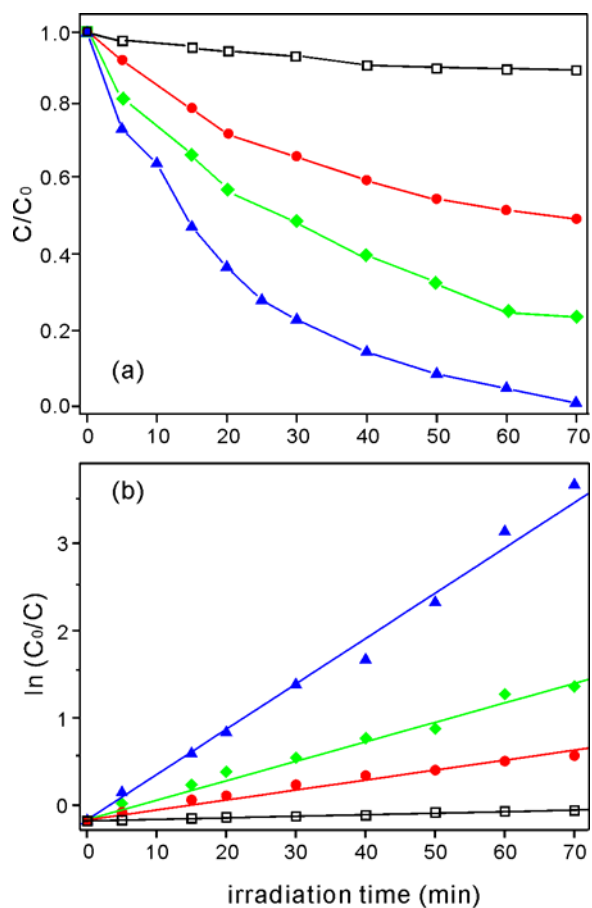
Figure 4-11 (a) Photocatalytic degradation kinetic profiles of MB (360 ppm) in 2 mL water in the (open) absence and (closed) presence of 4.8 mg TiO_2 nanopopcorns grown at VR(H_2O_2:HF:H_2O) of (triangles) 1:1:1000, (diamonds) 1:2.5:1000, and (circles) 2.5:1:1000 and (b) their pseudo-first-order kinetic rate plots. The rate constants obtained from the best-fitted lines of squares, circles, diamonds, and triangles are 0.11, 0.66, 1.3, and 3.0 h^{-1}, respectively.

The current density–voltage ($J–V$) characteristic curves in Figure 4-12 indicate that TiO_2 nanopopcorns grown on Ti foil perform well as the working electrode of DSSC without

being treated via any annealing process. The photovoltaic parameters of DSSCs in Table 4-1, obtained from the J–V characteristic profiles of Figure 4-12, reveal that the short-circuit current density (J_{sc}) of 11.5 mA cm^{-2} from DSSC with TiO$_2$ nanopopcorns grown on Ti foil at VR(H$_2$O$_2$:HF:H$_2$O) of 1:1:1000 is high in particular. The highest current density can probably be attributed to the best-defined anatase crystallinity and the largest surface area of the nanopopcorns grown at VR(H$_2$O$_2$:HF:H$_2$O) of 1:1:1000 to absorb dye molecules most effectively.[18–23] The open circuit voltages (V_{oc}) have been found to be 576, 548, and 518 mV for DSSCs based on TiO$_2$ nanopopcorns on Ti foil grown at VR(H$_2$O$_2$:HF:H$_2$O) of 1:1:1000, 1:2.5:1000, and 2.5:1:1000, respectively. The variation of V_{oc} can be attributed probably to different recombination rates in the conduction band of our TiO$_2$ nanopopcorns as discussed above with Figure 4-8.[17,18,22] Table 4-1 also indicates that the overall power conversion efficiency of DSSC changes enormously with the working electrode, which was based on TiO$_2$ nanopopcorns on Ti foil. The power conversion efficiency with TiO$_2$ nanopopcorns grown on Ti foil at VR(H$_2$O$_2$:HF:H$_2$O) of 1:1:1000, which is 6.6 times larger than that with TiO$_2$ nanopopcorns grown on Ti foil at VR(H$_2$O$_2$:HF:H$_2$O) of 2.5:1:1000, has been found to be as high as 3.98%. We suggest that the highest power conversion efficiency using TiO$_2$ nanopopcorns grown on Ti foil at VR(H$_2$O$_2$:HF:H$_2$O) of 1:1:1000 directly without being annealed results mainly from their largest surface area to absorb dye molecules largely and their best-defined anatase crystallinity to reduce recombination losses effectively.
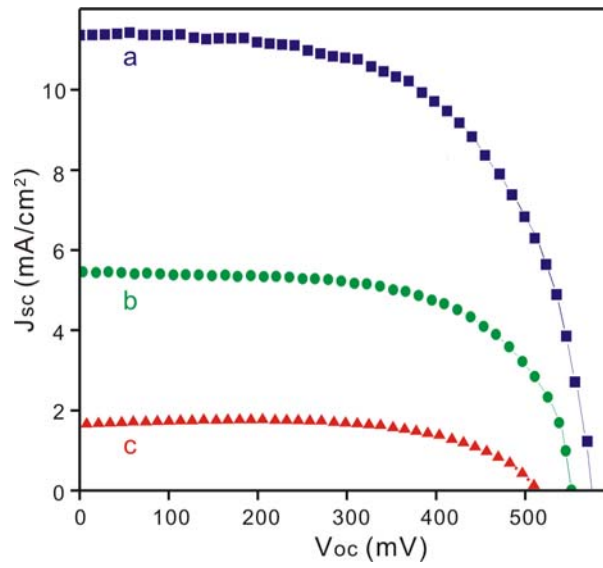
Figure 4-12 Current density-voltage characteristics of DSSCs based on TiO$_2$ nanopopcorns grown on Ti foil atVR(H$_2$O$_2$:HF:H$_2$O) of (a) 1:1:1000, (b) 1:2.5:1000, and (c) 2.5:1:1000.

Table 4-1 Photovoltaic operation parameters of DSSCs produced with anatase TiO$_2$ nanopopcorns grown on Ti foil electrodes grown at variation of VR(H$_2$O$_2$:HF:H$_2$O)

VR(H$_2$O$_2$:HF:H$_2$O)	J_{sc} [mA cm^{-2}]	V_{oc} [mV]	Fill factor	Efficiency
1:1:1000	11.5	576	60	3.98%
1:2.5:1000	5.52	548	61	1.85%
2.5:1:1000	1.75	518	66	0.60%

4. 5. Conclusions

Well-defined nanopopcorns of the tetragonal anatase TiO_2 have been facilely grown on Ti foil hydrothermally to be employed for photocatalytic and photovoltaic materials directly without being treated via any annealing process. Truncated tetragonal pyramidal TiO_2 nanocrystals have grown hierarchically on the surface of initial tetragonal bipyramidal TiO_2 nanostructures to form TiO_2 nanopopcorns exposing the {101} and {001} facets dominantly. The morphology of TiO_2 nanostructures with a minimal amount of Ti–OH in their surface has been controlled well by adjusting $VR(H_2O_2:HF:H_2O)$. TiO_2 nanopopcorns grown at $VR(H_2O_2:HF:H_2O)$ of 1:1:1000 have the best-defined –Ti–O– network of the tetragonal anatase TiO_2 structure with a minimal amount of trap sites and oxygen vacancies. The enhanced photocatalytic activity of our anatase TiO_2 nanopopcorns grown at $VR(H_2O_2:HF:H_2O)$ of 1:1:1000 arises from their 3D hierarchical nanostructures and exposed {001} facets. The highest power conversion efficiency of 3.98% using TiO_2 nanopopcorns grown on Ti foil at $VR(H_2O_2:HF:H_2O)$ of 1:1:1000 as the working electrode of DSSC results from their largest surface area to absorb dye molecules and their best-defined anatase crystallinity to reduce recombination losses.

4. 6. Acknowledgments

4. 7. References

[1]   Y. Yin, A. P. Alivisatos, *Nature* **2005**, *437*, 664.

[2]   A. Fujisjima, X. T. Zhang, D. A. Tryk, *Surf. Sci. Rep.* **2008**, *63*, 515.

[3]   J. Y. Kim, S. Lee, K.-H. Yoo, D.-J. Jang, *Appl. Phys. Lett.* **2009**, *94*, 153301.

[4]   M. Law, L. E. Greene, J. C. Johnson, R. Saykally, P. D. Yang, *Nature Mater.* **2005**, *4*, 455.

[5]   Y. Kuwahara, H. Yamashita, *J. Mater. Chem.* **2011**, *21*, 2407.

[6]   S. K. Choi, H. S. Yang, J. H. Kim, H. Park, *Appl. Catal. B-Envion.* **2012**, *121-122*, 206.

[7]   N. Bao, Y. Li, Z. T. Wei, G. B. Yin, J. J. Niu, *J. Phys. Chem. C* **2011**, *115*, 5708.

[8]   T.-D. Nguyen-Phan, E. W. Shin, *J. Ind. Eng. Chem.* **2011**, *17*, 397.

[9]   A. K. Chakraborty, Z. Qi, S. Y. Chai, C. Lee, S.-Y. Park, D.-J. Jang, W. I. Lee, *Appl. Catal. B-Envion.* **2010**, *93*, 368.

[10]   F. X. Xiao, *J. Mater. Chem.* **2012**, *22*, 7819.

[11]   A. Mills, S. L. Hunte, *J. Photochem. Photobiol. A-Chem.* **1997**, *108*, 1.

[12]   P. Wilhelm, D. Stephan, *J. Photochem. Photobiol. A-Chem.* **2007**, *185*, 19.

[13]   M. Čaplovičová, P. Billik, Ľ. Čaplovič, V. Brezová, T. Turáni, G. Plesch, P. Fejdi, *Appl. Catal. B-Environ.* **2012**, *117-118*, 224.

[14]   J. G. Yu, T. T. Ma, S. W. Liu, *Phys. Chem. Chem. Phys.* **2011**, *13*, 3491.

[15]   F. Bosc, A. Ayral, P.-A. Albouy, C. Guizard, *Chem. Mater.* **2003**, *15*, 2463.

[16]   J. J. Liao, S. W. Lin, L. Zhang, N. Q. Pan, X. K. Cao, J. B. Li, *ACS Appl. Mater. Interfaces* **2012**, *4*, 171.

[17]   W. Zhou, F. F. Sun, K. Pan, G. H. Tian, B. J. Jiang, Z. Y. Ren, C. G. Tian, H. G. Fu, *Adv. Funct. Mater.* **2011**, *21*, 1922.

[18]   N. K. Allam, K. Shankar, C. A. Grimes, *Adv. Mater.* **2008**, *20*, 3942.

[19]   Z. H. Zhang, P. Wang, *Energy Environ. Sci.* **2012**, *5*, 6506.

[20]   D. Zhao, T. Y. Peng, L. L. Lu, P. Cai, P. Jiang, Z. Q. Bian, *J. Phys. Chem. C* **2008**, *112*, 8486.

[21]   J.-Y. Liao, B.-X. Lei, H.-Y. Chen, D.-B. Kuang, C.-Y. Su, *Energy Environ. Sci.* **2012**, *5*, 5750.

[22]   S. H. Kang, S.-H. Choi, M.-S. Kang, J.-Y. Kim, H.-S. Kim, T. Hyeon, Y.-E. Sung, *Adv. Mater.* **2008**, *20*, 54.

[23]   N.-G. Park, J. van de Lagemaat, A. J. Frank, *J. Phys. Chem. B* **2000**, *104*, 8989.

[24]   W. P. Liao, J. J. Wu, *J. Mater. Chem.* **2011**, *21*, 9255.

[25]   B. Liu, E. S. Aydil, *J. Am. Chem. Soc.* **2009**, *131*, 3985.

[26]   J. W. Hou, X. C. Yang, X. Y. Lv, M. Huang, Q. Y. Wang, J. Wang, *J. Alloy. Compd.* **2012**, *511*, 202.

[27]   D. V. Portan, K. Papaefthymiou, E. Arvanita, G. Jiga, G. C. Papanicolaou, *J. Mater. Sci.* **2012**, *47*, 4696.

[28]   M. Liu, L. Y. Piao, L. Zhao, S. T. Ju, Z. J. Yan, T. He, C. L. Zhou, H. L. Li, W. J. Wang, *Chem. Comm.* **2010**, *46*, 1664.

[29]   M. Liu, L. Y. Piao, W. M. Lu, S. T. Ju, L. Zhao, C. L. Zhou, H. L. Li, W. J. Wang, *Nanoscale* **2010**, *2*, 1115.

[30]   X. H. Yang, Z. Li, C. H. Sun, H. G. Yang, C. Z. Li, *Chem. Mater.* **2011**, *23*, 3486.

[31]   N. K. Allam, C. A. Grimes, *Langmuir* **2009**, *25*, 7234.

[32]   S. D. Burnside, V. Shklover, C. Barbé, P. Comte, F. Arendse, K. Brooks, M. Grätzel, *Chem. Mater.* **1998**, *10*, 2419.

[33]   B. Liu, E. S. Aydil, *Chem.Comm.* **2011**, *47*, 9507.

[34]   F. Amano, O.-O. Prieto-Mahaney, Y. Terada, T. Yasumoto, T. Shibayama, B. Ohtani, *Chem. Mater.* **2009**, *21*, 2601.

[35]   Y. Q. Dai, C. M. Cobley, J. Zeng, Y. M. Sun, Y. N. Xia, *Nano Lett.* **2009**, *9*, 2455.

[36]   U. Diebold, *Surf. Sci. Rep.* **2003**, *48*, 53.

[37]   H. G. Yang, H. C. Zheng, *J. Phys. Chem. B* **2003**, *107*, 12244.

[38]   J. Mühlebach, K. Müller, G. Schwarzenbach, *Inorg. Chem.* **1970**, *9*, 2381.

[39]   H. Ichinose, M. Terasaki, H. Katsuki, *J. Sol-Gel Sci. Technol.* **2001**, *22*, 33.

[40]   S. Yoriya, M. Paulose, O. K. Varghese, G. K. Mor, C. A. Grimes, *J. Phys. Chem. C* **2007**, *111*, 13770.

[41]   J.-Y. Kim, M. R. Kim, S.-Y. Park, D.-J. Jang, *CrystEngComm* **2010**, *12*, 1803.

[42]   R. J. Bandaranayake, G. W. Wen, L. Y. Lin, H. X. Jiang, C. M. Sorensen, *Appl. Phys. Lett.* **1995**, *67*, 831.

[43]   D. Bersani, P. P. Lottici, X.-Z. Ding, *Appl. Phys. Lett.* **1998**, *72*, 73.

[44]   M. R. Bayati, F. Golestani-Fard, A. Z. Moshfegh, R. Molaei, *Mater. Res. Bull.* **2011**, *46*, 1642.

[45]   Zs. Pap, V. Danciu, Zs. Cegléd, Á. Kukovecz, A. Oszkó, A. Dombi, K. Mogyorósi, *Appl. Catal. B-Envion.* **2011**, *101*, 461.

[46]   Y. Lei, L. D. Zhang, G. W. Meng, G. H. Li, X. Y. Zhang, C. H. Liang, W. Chen, S. X. Wang, *Appl. Phys. Lett.* **2001**, *78*, 1125.

[47]   K. Shankar, G. K. Mor, H. E. Prakasam, S. Yoriya, M. Paulose, O. K. Varghese, C. A. Grimes, *Nanotechnology* **2007**, *18*, 065707.

[48]   K.-S. Ahn, M.-S. Kang, J.-W. Lee, Y. S. Kang, *J. Appl. Phys.* **2007**, *101*, 84312.

Chapter 5. Facile Synthesis of Highly Luminescent Water-Soluble CdTe/CdS/ZnS Quantum Dots[†]

---

5. 1. Abstract

Core-shell-shell quantum dots (QDs) of CdTe/CdS/ZnS having an average diameter of 4.2 nm and exhibiting type-II behaviors have been facilely synthesized in water *via* a one-pot technique. Water-dispersible CdTe/CdS/ZnS QDs have been prepared simply by injecting Zn^{2+}(aq) into an aqueous colloidal solution of CdTe/CdS core-shell QDs having an average diameter of 3.8 nm, which were already synthesized and stabilized in water with assistance of 3-mercaptopropionic acid. The optical properties of CdTe/CdS/ZnS QDs have been controlled by adjusting reaction time as well as pH, reaction temperature, and Zn^{2+} amount. The band-gap energy of CdTe/CdS/ZnS core-shell-shell QDs decreases gradually from 2.25 eV to 2.07 eV as the reaction time changes from 0 min to 720 min. The photoluminescence spectrum of CdTe/CdS/ZnS core-shell-shell QDs shifts to the red steadily from 538 nm to 613 nm as the reaction time changes from 0 min to 720 min. Photoluminescence has been found to be the most efficient when CdTe/CdS/ZnS core-shell-shell QDs were grown for 6 h at pH 10.6 and 100 $^{\circ}$C with [Zn] / [Cd] of 1/300. The photoluminescence quantum yield of the aqueous colloidal solution of CdTe/CdS/ZnS core-shell-shell QDs has been found to be as large as 15% whereas that of CdTe/CdS core-shell QDs has been observed as 4%.

5. 2. Introduction

The design and the controlled fabrication of nanostructured materials having functional properties have been extensively studied because of their potential applications in catalysis, optoelectronics, and transistors.[1-5] In particular, luminescent colloidal semiconductor nanoparticles attract considerable attention because they can be employed for the development of fluorescent dyes, light-emitted diodes, and solar cells.[6-9] Colloidal hybrid quantum dots (QDs) having composite core-shell or core-shell-shell structures are known to exhibit unique physical and chemical properties distinctly different from those of individual components.[6-21] In core-shell QDs of type-II structures such as ZnSe/CdS,[10] CdTe/CdSe,[11] and CdSe/CdTe,[12] the shell material having a wider band gap is grown onto the core material to reduce the nonradiative recombination effectively by confining the wave function of an electron-hole pair to the interior of the core material.[10-19] When QDs contain Cd^{2+} ions, an inherent cytotoxicity is observed as Cd^{2+} ions disorder from the QDs under UV irradiation.[15,22] For instance, CdTe QDs stabled by a mercaptan acid cannot be used singly in cells or tissues for bioapplications although they provide a simple way to generate aqueous QDs.[23-25] On the other hand, ZnS is nontoxic and chemically stable under any conditions although it has a wide band gap to passivate CdTe or CdSe cores efficiently. Thus, in composite nanostructures having CdTe or CdSe cores and ZnS shells, ZnS can not only decrease the toxicity of cadmium ions but also increase the quantum yield and the photostability of QDs.[20]

Diverse methods such as the organometallic precursor route,[26] the nonorganometallic

precursor route,[27] and the single-molecule precursor route[28] have been successfully established to synthesize highly luminescent QDs. However, most of those methods employ various alkylphosphine molecules to prepare complex precursors. Unfortunately, alkylphosphine molecules are well known to be hazard, unstable, and expensive, and QDs prepared in an organic solution are hard to be applied in an aqueous solution.[11,15,18,19] It has been reported that water-dispersible QDs can be directly synthesized *via* an aqueous method[29] and that composite QDs protected by ZnS shells can also be prepared in aqueous solutions by using a hydrothermal process,[11] a microwave irradiation method,[15] or a chemical aerosol flow method.[25] To the best of our knowledge, few approaches to synthesize luminescent core-shell-shell QDs with CdS inner shells and ZnS outer shells have been reported so far.[25,30-32] Although a few works have been paid attention to for the synthesis of the CdTe/CdS/ZnS core-shell-shell QDs, they have required extremely troublesome multisteps. Thus, the development of a low-cost, simple, and continuous way is urgently needed to prepare hydrophilic QDs capped with ZnS shells.

In this paper, we report a facile, simple, and economical process to synthesize highly luminescent CdTe/CdS/ZnS core-shell-shell QDs which are dispersible and stable in water. It is hard to grow a ZnS shell epitaxially on a CdTe core due to a large lattice mismatch between CdTe and ZnS (16.4%), which induces strain at the interface between the core and the shell and leads to a low luminescence quantum yield and a broad size distribution.[15,33] Thus, we have introduced a CdS inner shell, whose lattice constant is between those of CdTe and ZnS, between the CdTe core and the ZnS outer shell to reduce strain inside a nanocrystal

98

considerably. As shown in Scheme 5-1, the introduction of CdS between CdTe and ZnS has made the composite QDs exhibit type-II behaviors. The photoluminescence wavelength of a CdTe/CdS/ZnS core-shell-shell QD has been tuned widely as much as 75 nm by adjusting the thickness of the inner CdS shell. The photoluminescence quantum yield (PLQY) of the aqueous colloidal solution of CdTe/CdS/ZnS core-shell-shell QDs has been found to be as large as 15% whereas that of CdTe/CdS core-shell QDs has been observed as 4%.
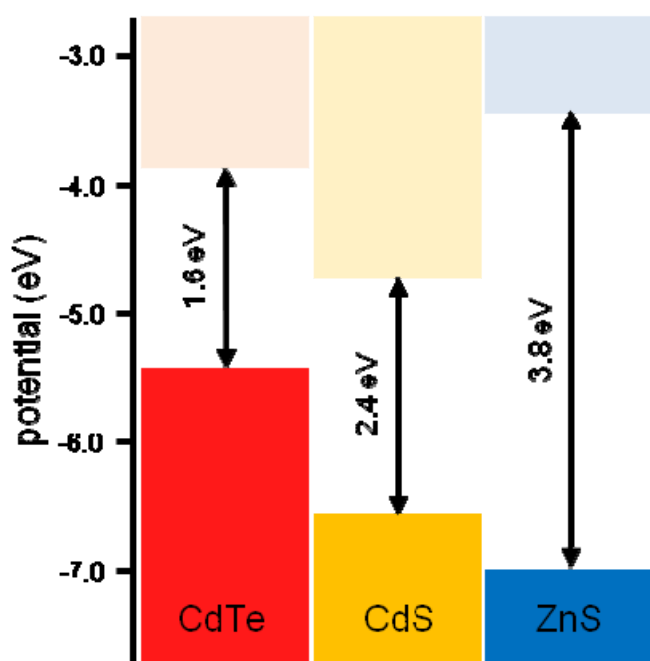
Scheme 5-1 Schematic representation of the energy-level alignment of a bulk CdTe/CdS/ZnS core-shell-shell system.

5. 3. Experimental Details

The analytical grade chemicals of $CdCl_2(s)$, 3-mercaptopropionic acid(l, MPA), $NaBH_4(s)$, $NaOH(s)$, $Te(s)$, and $ZnCl_2(s)$ were used as purchased from Sigma-Aldrich.

Deionized water with a resistivity of greater than 18 MΩ cm from a Millipore Milli-Q system was used throughout the experiments. An oxygen-free NaHTe solution as a telluride anion precursor was prepared *via* the following reaction:

$$4\ NaBH_4(aq) + 2\ Te(s) + 7\ H_2O(l) \rightarrow 2\ NaHTe(aq) + Na_2B_4O_7(aq) + 14\ H_2(g) \qquad (1)$$

1.6 mmol of $NaBH_4$(s) and 0.36 mmol of Te(s) were added into 2.0 mL of deionized water under N_2(g) atmosphere with stirring until the violet color became colorless. While the molar ratio of $Cd^{2+}/Te^{2-}/MPA$ was maintained to be 2/1/5 in the reaction, MPA-capped CdTe/CdS core-shell QDs were synthesized in an aqueous solution. 0.18 mmol of $CdCl_2$(s) and 39 μL of MPA(l) were added into 25 mL of deionized water, and the pH of the solution was adjusted to 9.0 by dropping 1.0 M NaOH(aq). Note that thioglycolic acid can also be employed to stabilize Cd^{2+} and Zn^{2+} ions. The mixture was placed in a three-necked flask and bubbled by N_2(g) for 30 min to remove O_2(g). Then 0.5 mL of an oxygen-free NaHTe solution prepared freshly *via* eq 1 was injected into the mixture quickly under vigorous stirring. The resulting mixed solution was heated and refluxed at 100 $^{\circ}$C for 2 h. CdTe/CdS/ZnS core-shell-shell QDs were prepared by adding 10 mM $ZnCl_2$(aq) into the above prepared aqueous colloidal solution of CdTe/CdS core-shell QDs. Thioacetamide and MPA can also be injected with $ZnCl_2$ to produce ZnS shells. We have found the optimal conditions for the synthesis of highly luminescent CdTe/CdS/ZnS core-shell-shell QDs after we tried diverse experimental conditions such as the volume of 10 mM $ZnCl_2$(aq) in μL (V_{Zn}, 1.8 x 10^4 [Zn] / [Cd]), pH, reaction time, and reaction temperature. The prepared QDs of core-shell CdTe/CdS and core-shell-shell CdTe/CdS/ZnS were precipitated by adding acetone and centrifuged at 10,000 rpm.

PLQYs were measured by comparing the fluorescence intensities of prepared QDs with those of primary standard Rhodamine 6G (quantum yield = 95% in water) solutions at the same optical density (OD = 0.05) and at the same excitation wavelength (355 nm). The integrated intensities of the emission spectra, corrected for differences in the refraction indices, were used to calculate PLQYs. High-resolution transmission electron microscopy (HRTEM) images as well as selected-area electron diffraction (SAED) patterns and energy dispersive X-ray (EDX) profiles were measured with a JEOL JEM-3000F microscope. While high-resolution X-ray diffraction (HRXRD) patterns were obtained with a Bruker D8 DISCOVER diffractometer using Cu Kα radiation (λ = 0.15418 nm), X-ray photoelectron spectroscopy (XPS) was investigated using a KRATOS AXIS-HSi spectrometer with an excitation source of Al Kα = 1486.6 eV. Absorption spectra were monitored by using a Scinco S-3100 spectrometer. Photoluminescence spectra were measured employing a Princeton Instruments ICCD576G CCD detector with excitation at 355 nm using 6 ns pulses from a Q-switched Quantel Brilliant Nd:YAG laser.

5. 4. Results and Discussion

The HRTEM images of Figure 5-1a and Figure 5-2a show that CdTe/CdS/ZnS core-shell-shell QDs grown with V_{Zn} of 60, as well as CdTe/CdS core-shell QDs without ZnS shells, have spherical structures with good crystallinity. The average diameters of CdTe/CdS/ZnS

core-shell-shell QDs and CdTe/CdS core-shell QDs have been found to be 4.2 and 3.8 nm, respectively, suggesting that the thickness of the outer ZnS shell of CdTe/CdS/ZnS QDs is as thin as 0.2 nm. The structural details of QDs have been further provided by measuring enlarged HRTEM images and SAED patterns. The observed lattice-fringe distance (0.37 nm) of a CdTe/CdS/ZnS core-shell-shell QD in Figure 5-1b is the same as that of a CdTe/CdS core-shell QD in Figure 5-2b and agrees well with the spacing of the (111) planes of the cubic zinc blende CdTe structure. All the average d-spacing values calculated from the observed SAED patterns of Figure 5-1c and Figure 5-2c also agree with the respective standard interplanar distances of the cubic zinc blende CdTe structure. These suggest that both the enlarged
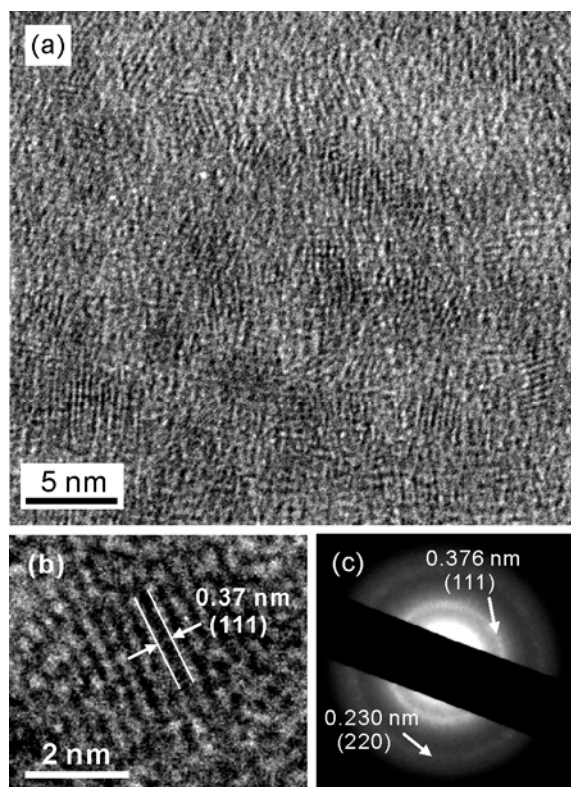
Figure 5-1 HRTEM images (a,b) and SAED pattern (c) of CdTe/CdS/ZnS core-shell-shell QDs grown for 6 h with V_{Zn} of 60 at pH 10.6 and 100 $^\circ$C.

HRTEM of Figure 5-1b and the SAED pattern of Figure 5-1c reveal mainly the structural details of the CdTe core because both the inner CdS and the outer ZnS shells are very thin compared with the CdTe core. However, the EDX profiles of Figure 5-3 indicate that CdTe/CdS/ZnS core-shell-shell QDs have ZnS shells as well as CdS shells and that CdTe/CdS core-shell QDs have CdS shells indeed. Thus, Figures 5-1 and 5-2 reveal that CdTe/CdS/ZnS core-shell-shell QDs have been synthesized successfully in an aqueous solution *via* a one-pot technique.

Figure 5-2 HRTEM images (a,b) and SAED pattern (c) of CdTe/CdS QDs grown at pH 9.0 and 100 $^\circ$C.

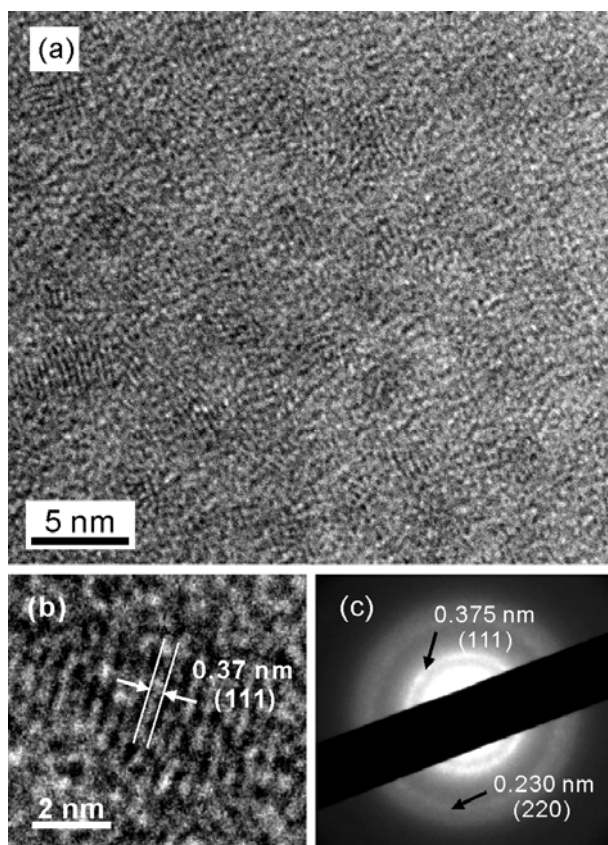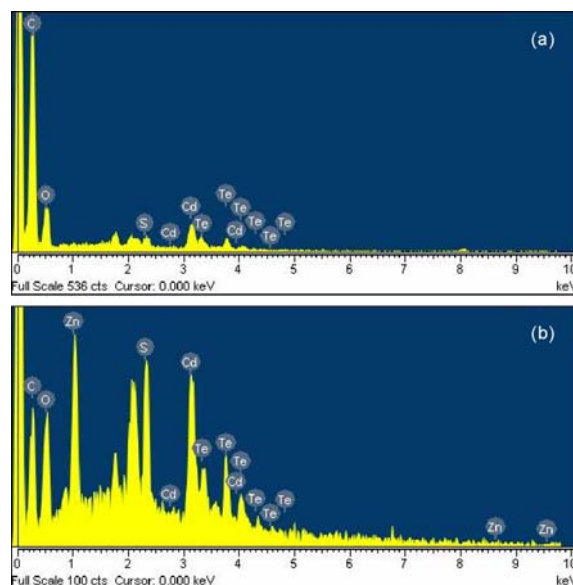**Figure 5-3** EDX profiles of CdTe/CdS/ZnS core-shell-shell QDs grown with V_{Zn} of 0 (a) and 60 (b) at pH 10.6 and 100 $^{\circ}$C. The molar ratios of Cd/Te/S/Zn were found to be 2.1/1.0/1.3/0.0 in the profile *a* and 1.8/1.0/2.1/2.2 in the profile *b*.

The HRXRD pattern in Figure 5-4 of CdTe/CdS QDs prepared without the addition of Zn^{2+} agrees well with the standard diffraction pattern of the reference cubic zinc blende CdTe structure with a lattice constant of a = 6.49 Å (JCPDS Card No. 10-0207). The standard diffraction patterns of the reference cubic structures of CdS and ZnS with lattice constants of a = 5.82 Å (JCPDS Card No. 42-1411) and a = 5.41 Å (JCPDS Card No. 05-0566), respectively, are also shown in Figure 5-4. The mean crystallite diameter, *d*, of CdTe/CdS QDs can be determined from the line width of a HRXRD spectrum by using the Scherrer's formula $<d>$ = $0.94\lambda/(B\cos\theta_B)$, where λ is the X-ray wavelength, *B* is the full width at the half maximum of the diffraction peak (radian), and θ_B is the half angle of a diffraction peak on the 2θ scale.[34,35] The mean crystallite diameter of CdTe/CdS core-shell QDs has been estimated to be 3.7 nm by using the (111) peak at 2θ of 23.8˚. The fact that the mean crystallite diameter (3.7 nm)

calculated with the HRXRD pattern is very close to the average diameter (3.8 nm) estimated

with the HRTEM of Figure 5-2a suggests that the CdTe cores of CdTe/CdS core-shell QDs

have single-crystalline structures and that the CdS shells of CdTe/CdS core-shell QDs are as

thin as 0.05 nm. Then, the latter one hints that the CdS shell of a CdTe/CdS core-shell QD is

produced as Cd on the surface of the CdTe core binds with MPA to form a chemical bond of

Cd-SR, where R is an organic group of $CH_2CH_2CO_2^-$. As V_{Zn} used to grow CdTe/CdS/ZnS

core-shell-shell QDs increases, not only the diffraction peaks of the cubic ZnS structure grow

newly but also the diffraction peaks of the cubic CdS structure increase slightly. This suggests

that while an outer ZnS shell forms newly on the surface of a CdTe/CdS QD, the inner CdS

shell becomes thicker as Zn^{2+} is added to the aqueous colloidal solution of CdTe/CdS QDs.

However, the positions and the widths of the diffraction peaks of the CdTe cores remain
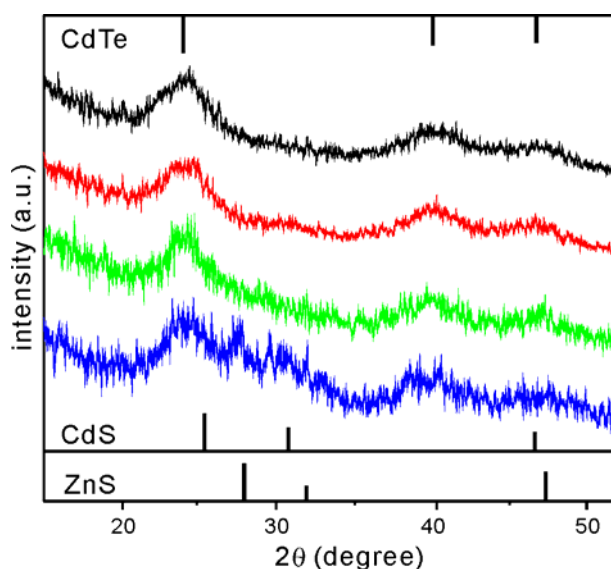

Figure 5-4 HRXRD patterns of CdTe/CdS/ZnS core-shell-shell QDs grown with V_{Zn} of 0 (black), 30 (red), 60 (green), and 90 (blue) at pH 10.6 and 100 $^{\circ}$C. The standard diffraction lines of cubic CdTe, cubic CdS, and cubic ZnS are also shown for comparison.

almost invariantly regardless of the increase of V_{Zn}. This suggests that a core-shell-shell structure, rather than an alloyed structure, has been produced by the addition of Zn^{2+}. According to the Vegard's law, the formation of a homogeneous alloy is expected to exhibit a significant narrowing of XRD peak widths by the increase of nanoparticle sizes.[15,36-39]

The XPS spectra of Figure 5-5 can provide further significant information about the surface composition of CdTe/CdS core-shell QDs and CdTe/CdS/ZnS core-shell-shell QDs. For the XPS analysis of as-prepared QDs, the colloidal QDs were precipitated by using a centrifuge and then dropped on a Si wafer and dried at room temperature. The observed binding energies of the Cd 3d of CdTe/CdS/ZnS QDs grown with V_{Zn} of 0, 30, and 60 are 403.2, 403.5, and 403.9 eV, respectively. In other words, the binding energy of Cd 3d shifts to the higher energy and the intensity of Cd 3d increases as V_{Zn} increases. Increment in the thickness of the CdS shell increases the binding energy of Cd 3d because the electronegativity of S is higher than that of Te. The intensity increase of Cd 3d with the increment of V_{Zn} indicates that the addition of Zn^{2+} not only forms the outer ZnS shell but also increases the thickness of the inner CdS shell apparently. Whereas the intensity of Te 3d decreases, the intensity of Zn 2p appears newly and increases with the increase of V_{Zn}. However, the binding energies of both Te 3d and Zn 2p remain almost the same regardless of V_{Zn}. These indicate that Te remains in the CdTe core whereas Zn^{2+} binds only with S^{2-} to form the outer ZnS shell with the addition of Zn^{2+} to an aqueous colloidal solution of CdTe/CdS core-shell QDs. On the other hand, S 2p shifts to the lower binding energy and increases in intensity with V_{Zn}. The binding energies of S 2p have been found as 162.4, 161.7, and 161.3 eV for CdTe/CdS/ZnS

QDs grown with V_{Zn} of 0, 30, and 60, respectively. The large change in S 2p binding energy suggests that the sulfur atom of the chemical bond of Cd-SR existing on the surface of CdTe/CdS core-shell QD releases the organic group R to bind with Zn^{2+}, increasing the thickness of the inner CdS shell as V_{Zn} increases.[19,40] The increase of S 2p intensity with V_{Zn} suggests that the sulfur atom of MPA(aq) also binds with Zn^{2+} to form the outer ZnS shell. Overall, Figure 5-5 has revealed that the addition of Zn^{2+} to an aqueous colloidal solution of CdTe/CdS core-shell QDs, where the atomic molar ratio of Cd/Te/S is 2/1/5, not only produces the outer ZnS shells but also increases the thickness of the inner CdS shells.
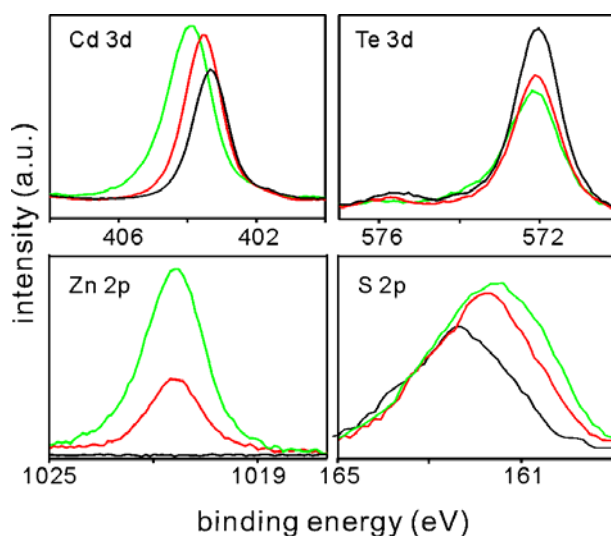
Figure 5-5 XPS spectra of CdTe/CdS/ZnS core-shell-shell QDs grown with V_{Zn} of 0 (black), 30 (red) and 60 (green) at pH 10.6 and 100 $^{\circ}$C.

Figure 5-6 shows that the extinction spectrum of CdTe/CdS/ZnS core-shell-shell QDs grown with V_{Zn} of 60 at pH 10.6 and 100 $^{\circ}$C in an aqueous solution shifts to the longer wavelength gradually from 509 nm to 574 nm as the reaction time changes from 0 min to 720 min. On the other hand, the band-gap energy of CdTe/CdS/ZnS QDs, estimated by plotting

the $(\alpha h\nu)^2$ of a scatter-removed extinction spectrum against photon energy $(h\nu)$,[41] decreases

steadily from 2.25 eV to 2.07 eV as the reaction time increases from 0 min to 720 min. The

molar ratio of Cd/Te/MPA was set to be 2/1/5, allowing that extra Cd-SR monomers in the

aqueous colloidal solution of CdTe/CdS core-shell QDs increase the thickness of the CdS

shell while the S of extra MPA binds with Zn to form the outer ZnS shell newly with the

addition of Zn^{2+}(aq). As the thickness of the inner CdS shell increases, Scheme 1 suggests

that the extinction spectrum of QDs shifts to the longer wavelength and that their band-gap

energy decreases because electrons in the valence band of the CdTe core can be directly

excited to the conduction band of the inner CdS shell.

Figure 5-6 Absorption spectra of the aqueous colloidal solutions of CdTe/CdS/ZnS core-shell-shell QDs grown with V_{Zn} of 60 at pH 10.6 and 100 °C for indicated reaction times in units of min.
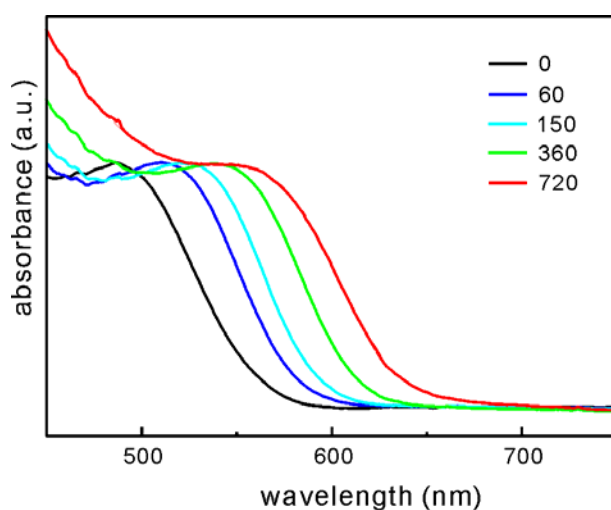
The photoluminescence spectrum of CdTe/CdS/ZnS core-shell-shell QDs grown with

V_{Zn} of 60 at pH 10.6 and 100 °C in an aqueous solution has been observed to shift to the red

from 538 nm to 613 nm as the reaction time changes from 0 min to 720 min (Figure 5-7). The red shift has been attributed to the thickness increase of the inner CdS shells of CdTe/CdS/ZnS core-shell-shell QDs as the reaction time increases. When the CdTe core is excited, an electron moves to the conduction band of the inner CdS shell and recombines with a hole in the valence band of the CdTe core to emit photoluminescence.[7] The formation of alloyed $Cd_xZn_{1-x}Te_yS_{1-y}$ QDs would lead to a blue shift in both extinction and photoluminescence spectra because of the larger band-gap energy of alloyed QDs.[15,19,37,39] Thus, the red shift with the increase of the reaction time also indicates that our intended CdTe/CdS/ZnS core-shell-shell QDs, rather than $Cd_xZn_{1-x}Te_yS_{1-y}$ alloyed QDs, have been produced successfully. As shown in Figure 5-8, the photoluminescence intensity of the CdTe/CdS/ZnS core-shell-shell QDs increases as largely as 3 times as the reaction time changes from 0 min to 720 min. The PLQY of CdTe/CdS core-shell QDs has been found to increase from 4% to 15% as the QDs were treated for 6 h at pH 10.6 and 100 °C with V_{Zn} of 60. These have been attributed to the decrease of defect sites and
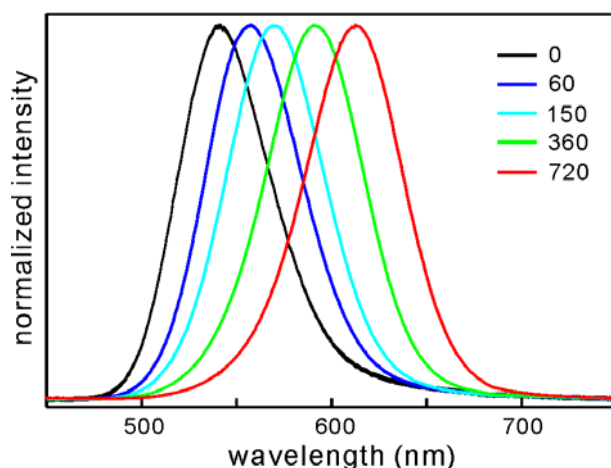

Figure 5-7 Maximum-normalized photoluminescence spectra of the aqueous colloidal solutions of CdTe/CdS/ZnS core-shell-shell QDs grown with V_{Zn} of 60 at pH 10.6 and 100 °C for indicated reaction times in units of min.
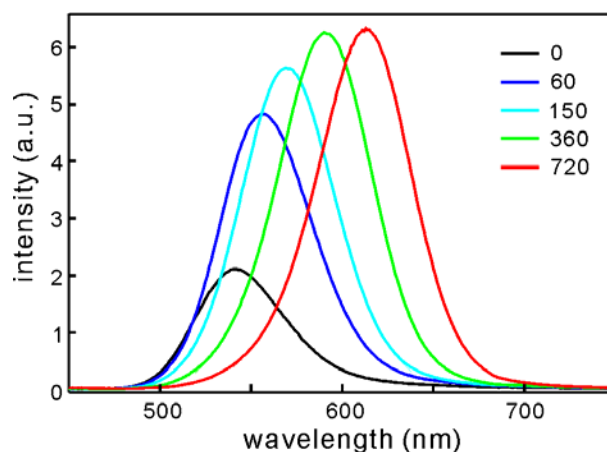
Figure 5-8 Photoluminescence spectra of the aqueous colloidal solutions of CdTe/CdS/ZnS core-shell-shell QDs grown with V_{Zn} of 60 for indicated reaction times in units of min at pH 10.6 and 100 $^{\circ}$C.

surface states owing to improved crystallinity and increased size with the increase of the reaction time. In particular, the outer ZnS shell with a wide energy gap internalizes photogenerated electrons and holes as well as prevents the Cd^{2+} ions from leaking into the aqueous solution.[7,42] If the shells are not thick enough, the photoluminescence stability of the core-shell-shell QDs is not greatly improved. However, if the shells are too thick, the PLQY of the QDs decreases because of largely increased scattering. Thus, the optimized shell thickness is a key point for the core-shell-shell QDs to have a high PLQY and good stability.

We have found the optimal conditions for the synthesis of highly luminescent CdTe/CdS/ZnS core-shell-shell QDs after we varied experimental conditions of V_{Zn}, pH, and reaction temperature in addition to reaction time. Figure 5-9a shows that the extinction spectrum of CdTe/CdS/ZnS core-shell-shell QDs shifts to the longer wavelength by 30 nm while the extinction magnitude of CdTe/CdS/ZnS core-shell-shell QDs has been found to

110

increase gradually with the increment of V_{Zn}. However, extinction resulting from scattering increases suddenly as V_{Zn} changes from 60 to 90. These suggest that the thickness of the shells increases with the increment of V_{Zn} and that the optimized shell thickness of CdTe/CdS/ZnS core-shell-shell QDs can be achieved at V_{Zn} of 60. Figure 5-9b shows that the photoluminescence spectrum of CdTe/CdS/ZnS core-shell-shell QDs shifts to the red by 28 nm with the increment of V_{Zn} while its spectral width remains almost invariantly. The latter one suggests that the size distribution of QDs changes hardly with V_{Zn}.[6] Whereas the photoluminescence intensity of CdTe/CdS/ZnS core-shell-shell QDs increases with V_{Zn} until V_{Zn} of 60, that decreases with V_{Zn} above V_{Zn} of 60. This also supports that the optimized shell thickness of the core-shell-shell QDs can be obtained at V_{Zn} of 60. Figure 5-10 shows that pH of an aqueous colloidal solution of CdTe/CdS/ZnS core-shell-shell QDs is also one of important factors to prepare highly luminescent QDs. In order to study the influence of pH on the photoluminescence of the core-shell-shell QDs, pH was controlled by adding 0.1 M NaOH(aq) or HCl(aq) to the as-prepared aqueous colloidal solution of CdTe/CdS core-shell QDs, whose initial pH was 9.0. The photoluminescence of the CdTe/CdS/ZnS core-shell-shell QDs has been found to be the strongest at pH as high as 10.6 (Figure 5-10a) because the precipitation of the QDs decreases with the increase of pH, as suggested by their extinction spectra (Figure 5-10b). Although it has been reported that higher reaction temperature can cause broad distribution of sizes and large amount of surface defects,[15,43] Figure 5-11 suggests that reaction temperature as high as 100 $^\circ$C is necessary to synthesize highly luminescent CdTe/CdS/ZnS core-shell-shell QDs facilely in water at ambient pressure.

Figure 5-9 Absorption spectra (a) and photoluminescence spectra (b) of the aqueous colloidal solutions of CdTe/CdS/ZnS core-shell-shell QDs grown for 6 h with indicated V_{Zn} at pH 10.6 and 100 $^{\circ}$C.

Figure 5-10 Extinction spectra (a) and photoluminescence spectra (b) of the aqueous colloidal solutions of CdTe/CdS/ZnS core-shell-shell QDs grown for 6 h with V_{Zn} of 60 at 100 $^{\circ}$C and indicated pHs.

Figure 5-11 shows that pH of an aqueous colloidal solution of CdTe/CdS/ZnS core-shell-shell QDs is also one of important factors to prepare highly luminescent QDs. In order to study the influence of pH on the photoluminescence of the core-shell-shell QDs, pH was controlled by adding 0.1 M NaOH(aq) or HCl(aq) to the as-prepared aqueous colloidal solution of CdTe/CdS core-shell QDs, whose initial pH was 9.0. The photoluminescence of the CdTe/CdS/ZnS core-shell-shell QDs has been found to be the strongest at pH as high as 10.6 because the precipitation of the QDs decreases with the increase of pH, as suggested by their absorption spectra. Although it has been reported that higher reaction temperature can cause broad distribution of sizes and large amount of surface defects (He et al. 2008), Figure 5-11 suggests that reaction temperature as high as 100 $^\circ$C is necessary to synthesize highly luminescent CdTe/CdS/ZnS core-shell-shell QDs facilely in water at ambient pressure.

Figure 5-11 Photoluminescence spectra of the aqueous colloidal solutions of CdTe/CdS/ZnS core-shell-shell QDs grown for 6 h with V_{Zn} of 60 at pH 10.6 and indicated temperatures in units of $^\circ$C.
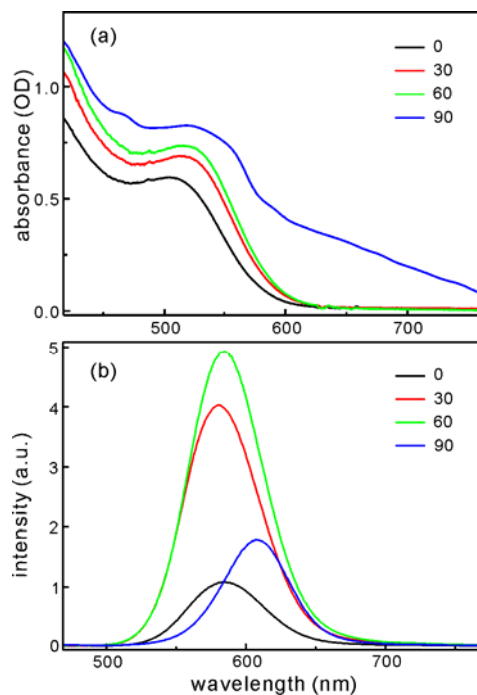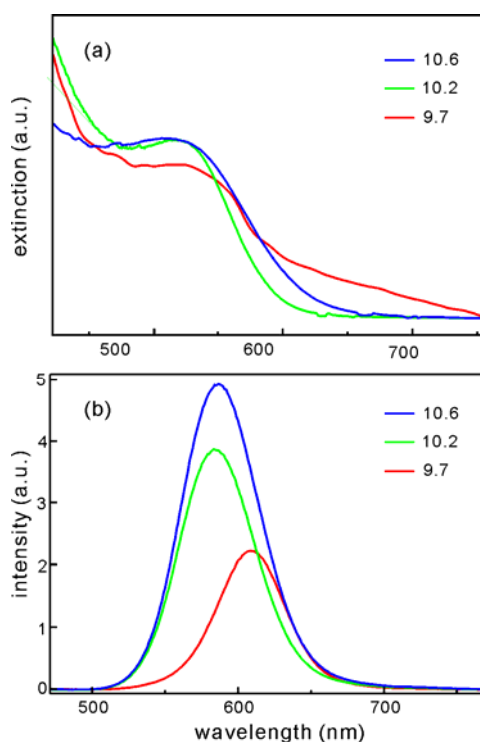
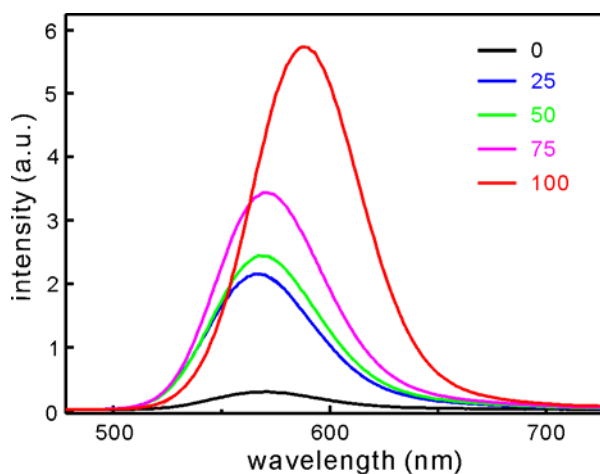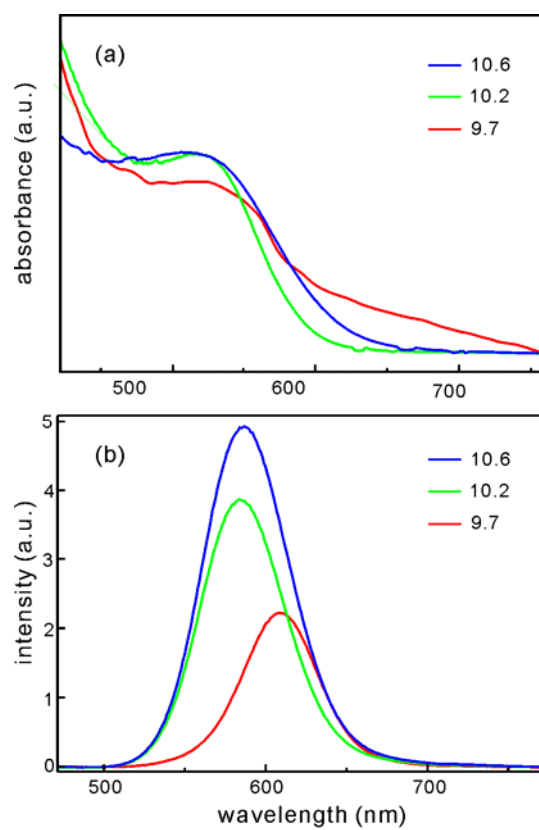**Figure 5-12** Absorption spectra (a) and photoluminescence spectra (b) of the aqueous colloidal solutions of CdTe/CdS/ZnS core-shell-shell QDs grown for 6 h with V_{Zn} of 60 at 100 °C and indicated pHs.

5. 5. Conclusions

Water-dispersible CdTe/CdS/ZnS core-shell-shell QDs having an average diameter of 4.2 nm and exhibiting type-II behaviors have been facilely synthesized by injecting Zn^{2+}(aq) simply into an aqueous colloidal solution of CdTe/CdS core-shell QDs having an average diameter of 3.8 nm. HRXRD patterns suggest that while an outer ZnS shell forms newly on the surface of a CdTe/CdS core-shell QD, the inner CdS shell becomes thicker with the addition of Zn^{2+}(aq). XPS spectra have also revealed that the addition of Zn^{2+} to the aqueous colloidal solution, where the atomic molar ratio of Cd/Te/S is 2/1/5, not only produces the outer ZnS shells but also increases the thickness of the inner CdS shells. The optical properties of CdTe/CdS/ZnS QDs have been controlled by adjusting reaction time as well as V_{Zn}, pH, and reaction temperature. The absorption spectrum of the QDs shifts to the longer wavelength and their band-gap energy decreases with shell thickness because electrons in the valence band of the CdTe core can be directly excited to the conduction band of the inner CdS shell. The photoluminescence spectrum of CdTe/CdS/ZnS core-shell-shell QDs shifts to the red from 538 to 613 nm as the reaction time changes from 0 to 720 min. The red shift has been attributed to the thickness increase of the inner CdS shells of CdTe/CdS/ZnS core-shell-shell QDs with the reaction time. The photoluminescence has been found to be the most efficient when CdTe/CdS/ZnS core-shell-shell QDs were grown for 6 h at pH 10.6 and 100 $^{\circ}$C with V_{Zn} of 60. The PLQY of the aqueous colloidal solution of CdTe/CdS/ZnS QDs has been found to be as large as 15% whereas that of CdTe/CdS core-shell QDs has been observed as 4%.

5. 6. Acknowledgments

5. 7. References

[1] Y. J. Song, R. M. Garcia, R. M. Dorin, H. R. Wang, Y. Qiu, E. N. Coker, W. A. Steen, J. E. Miller, J. A. Shelnutt, *Nano Lett.* **2007**, *7*, 3650.

[2] R. Costi, A. E. Saunders, U. Banin, *Angew. Chem. Int. Ed.* **2010**, *49*, 4878.

[3] J.-Y. Kim, S. Lee, K.-H. Yoo, D.-J.; Jang, *Appl. Phys. Lett.* **2009**, *94*, 153301.

[4] Y. Yang, J. L. Shi, H. R. Chen, S. G. Dai, Y. Liu, *Chem. Phys. Lett.* **2003**, *370*, 1.

[5] J.-Y. Kim, S. J. Kim, D.-J. Jang, *J. Phys. Chem. C* **2011**, *115*, 672.

[6] F.-Y. Liu, J.-S. Yu, *J. Colloid Interf. Sci.* **2010**, *351*, 1.

[7] S. Taniguchi, M. Green, S. B. Rizvi, A. Seifalian, *J. Mater. Chem.* **2011**, *21*, 2877.

[8] F. Aldeek, L. Balan, G. Medjahdi, T. Roques-Carmes, J.-P. Malval, C. Mustin, J. Ghanbaja, R. Schneider, *J. Phys. Chem. C* **2009**, *113*, 19458.

[9] M. R. Kim, J. H. Chung, M. Lee, S. Lee, D.-J. Jang, *J. Colloid Interf. Sci.* **2010**, *350*, 5.

[10] Z. J. Ning, H. N. Tian, C. Z. Yuan, Y. Fu, H. Y. Qin, L. C. Sun, H. Ågren, *Chem. Comm.* **2011**, *47*, 1536.

[11] J. Wang, H. Y. Han, *J. Colloid Interf. Sci.* **2010**, *351*, 83.

[12] B. Blackman, D. M. Battaglia, T. D. Mishima, M. B. Johnson, X. Peng, *Chem. Mater.* **2007**, *19*, 3815.

[13] W. J. Zhang, G. J. Chen, J. Wang, B. C. Ye, X. H. Zhong, *Inorg. Chem.* **2009**, *48*, 9723.

[14] C.-Y. Chen, C.-T. Cheng, C.-W. Lai, Y.-H. Hu, P.-T. Chou, Y.-H. Chou, H.-T. Chiu, *Small* **2005**, *1*, 1215.

[15] Y. He, H.-T. Lu, L.-M. Sai, Y.-Y. Su, M. Hu, C.-H. Fan, W. Huang, L.-H. Wang, *Adv. Mater.* **2008**, *20*, 3416.

[16] D. V. Talapin, I. Mekis, S. Götzinger, A. Kornowski, O. Benson, H. Weller, *J. Phys. Chem. B* **2004**, *108*, 18826.

[17] S. Kim, B. Fisher, H.-J. Eisler, M. Bawendi, *J. Am. Chem. Soc.* **2003**, *125*, 11466.

[18] Z. Y. Gu, L. Zou, Z. Fang, W. H. Zhu, X. H. Zhong, *Nanotechnol.* **2008**, *19*, 135604.

[19] H. Peng, L. J. Zhang, C. Soeller, J. Travas-Sejdic, *J. Lumin.* **2007**, *127*, 721.

[20] W. Qin, R. A. Shah, P. Guyot-Sionnest, *ACS Nano* **2012**, *6*, 912.

[21] H. B. Shen, H. Z. Wang, Z. J. Tang, J. Z. Niu, S. Y. Lou, Z. L. Du, S. L. Li, *CrystEngComm* **2009**, *11*, 1733.

[22] A. M. Defus, W. C. W. Chan, S. N. Bhatia, *Nano Lett.* **2004**, *4*, 11.

[23] V. A. Sinani, D. S. Koktysh, B.-G. Yun, R. L. Matts, T. C. Pappas, M. Motamedi, S. N. Thomas, N. A. Kotov, *Nano Lett.* **2003**, *3*, 1177.

[24] J. N. Tian, R. J. Liu, Y. C. Zhao, Y. Peng, X. Hong, Q. Xu, S. L. Zhao, *Nanotechnol.* **2010**, *21*, 305101.

[25] C. M. Yan, F. Q. Tang, L. L. Li, H. B. Li, X. L. Huang, D. Chen, X. W. Meng, J. Ren, *Nanoscale Res. Lett.* **2010**, *5*,189.

[26] C. B. Murray, D. J. Norris, M. Bawendi, *J. Am.Chem. Soc.* **1993**, *115*, 8706.

[27] L. Qu, A. Peng, X. G. Peng, *Nano Lett.* **2001**, *1*, 333.

[28] M. Green, P. O'Brien, *Chem. Commun.* **1999**, 2235.

[29] H. Zhang, Z. Zhou, B. Yang, M. Y. Gao, *J. Phys. Chem. B* **2003**, *107*, 8.

[30] S. S. Xu, H. B. Shen, C. H. Zhou, H. Yuan, C. S. Liu, H. Z. Wang, L. Ma, L. S. Li, *J. Phys. Chem. C* **2011**, *115*, 20876.

[31] J. Wang, X. C. Jiang, H. Y. Han, N. Li, *Electrochem. Commun.* **2011**, *13*, 359.

[32] M. Green, P. Williamson, M. Samalova, J. Davis, S. Brovelli, P. Dobson, F. Cacialli, *J. Mater. Chem.* **2009**, *19*, 8341.

[33] B. O. Dabbuousi, J. Rodriguez-Viejo, F. V. Mikulec, J. R. Heine, J. R. Mattoussi, R. Ober, K. F. Jensen, M. Bawendi, *J. Phys. Chem. B* **1997**, *101*, 9463.

[34] D. Routkevitch, T. Bigioni, M. Moskovits, J. M. Xu, *J. Phys. Chem.* **1996**, *100*, 14037.

[35] J.-Y. Kim, H. Jeong, D.-J. Jang, *J. Nanopart. Res.* **2011**, *13*, 6699.

[36] X. H. Zhong, Y. Y. Feng, W. Knoll, M. Y. Han, *J. Am. Chem. Soc.* **2003**, *125*, 13559.

[37] C.-T. Cheng, C.-Y.; Chen, C.-W.; Lai, W. H. Liu, S.-C. Pu, P.-T. Chou, Y.-H. Chou, H.-T. Chiu, *J. Mater. Chem.* **2005**, *15*, 3409.

[38] L. Vegard, H. Schjelderup, *Phys. Z.* **1917**, *18*, 93.

[39] Y. He, H.-T. Lu, L.-M. Sai, W.-Y. Lai, Q. L. Fan, L.-H. Wang, W. Huang, *J. Phys. Chem. B* **2006**, *110*, 13370.

[40] H. Borchert, D. V. Talapin, N. Gaponik, C. McGinley, S. Adam, A. Lobo, T. Möller, H. Weller, *J. Phys. Chem. B* **2003**, *107*, 9662.

[41] F. Y. Shen, W. X. Que, X. T. Yin, Y. W. Huang, Q. Y. Jia, *J. Alloy. Compd.* **2011**, *509*, 9105.

[42] Z. Fang, Y. Li, H. Zhang, X. H. Zhong, L. Y. Zhu, *J. Phys. Chem. C* **2009**, *113*, 14145.

[43] Y. He, H.-T. Lu, L.-M. Sai, W.-Y. Lai, Q.-L. Fan, L.-H. Wang, W. Huang, *J. Phys. Chem. B* **2006**, *110*, 13352.

Appendices

A. Preferentially Linear Connection of Gold Nanoparticles in Derivatization with Phosphorothioate Oligonucleotides[†]

A. 1. Abstract

A gold nanosphere in water is considered to attain special stability in derivatization like an artificial atom when the octet rule is satisfied by forming four covalent bonds with two $5'$-phosphorothioate-modified oligonucleotide molecules. Owing to this, the hybridization of two mutually complementary gold-bound oligonucleotides makes gold nanospheres preferentially connected linearly by duplexes to produce strands like linear artificial molecules. We have then fixated the linear strands of DNA-linked gold nanospheres by reducing Ag^+ ion clusters immobilized around duplexes to show the absorption spectrum of silver-coated artificial-molecular nanorods.

A. 2. Introduction

The spectroscopic, electronic, and chemical properties of nanocrystalline materials are of great interest in both basic and applied researches.[1,2] In particular, metal nanostructures attract considerable attention scientifically as well as industrially because they can be possibly used in diverse applications such as catalysis, devices, transistors, and optoelectronics.[1,3] Nanoclusters and colloidal solutions of noble metals exhibit characteristic optical and physical properties that are substantially different from those of the corresponding bulk metals, thus attracting a great deal of interest.[4–6] In addition, coreshell and alloy bimetallic nanoparticles can exhibit peculiar electronic, optical, and catalytic properties that are absent in the corresponding monometallic nanoparticles.[7–9] The conduction electron charge density and its corresponding electromagnetic field in metallic systems can undergo plasmon oscillations. Because of the nature of the optical constants for noble metals, the charge oscillations can propagate along the surface at optical frequencies.[7,10] The optical response of metal nanopaticles can be tuned by controlling their size, shape, composition, and environment, providing a starting point for emerging research fields like surface plasmon-based photonics or plasmonics.[7,10]

Molecular building blocks offer a variety of possibilities to fabricate and manipulate nanostructured materials with "bottom up" approaches.[11,12] Oligonucleotides serve as building blocks of nanostructures for novel electronic devices and biological modifiers of nanoparticles and surfaces.[3,13] They are of special interest due to their self-organization

121

ability, combinatorial information capacity, and molecular-biological processability.[14] Their complexes with nanoparticles could be employed as highly sensitive labels.[11,14,15] The complementary specificity of DNA by the hybridization of specifically designed linker strands provides a precise means for programming the assembly of colloidal nanoparticles.[14,16–18] The most studied template DNA molecules are terminal-modified DNA, in which the thiol group is modified at the 5' or 3' terminus of DNA.[12,16–19] While self-assembly depends on interactions, sizes, and shapes,[5,20] large assemblies are often constructed by using mutually complementary oligonucleotides attached to nanoparticles.[16,18,19] Beyond the fundamental motivation to understand the underlying mechanisms involved in self-organization processes, self-assembled architectures of metallic nanoparticles have potential applicabilities in nanotechnologies.[21]

Nanoparticles of metals and semiconductors with diameters in the range of $\tilde{1}30$ nm behave as "artificial atoms" having size-dependent optical and electronic properties.[10,22–26] This analogy originates from quantum confinement and single-charge tunneling effects in semiconductor and metal nanocrystals.[1,22,24–26] In particular, the electronic wave functions of semiconductor nanocrystals have been reported[23] to exhibit atomic-like symmetries of 's' and 'p'. Furthermore, arrays of chemically synthesized nanocrystals can also behave as "artificial atomic solids" with unique collective properties derived from size-dependent nanocrystal properties and inter-nanoparticle coupling mechanisms.[14,24,25] It has also been reported[5–7,10] that a compelling analogy exists between plasmon resonances of metallic nanoparticles and wave functions of simple atoms and molecules. In "artificial molecules" of

complex metallic nanostructures, the plasmons mix and hybridize just like the electron wave functions of simple atomic and molecular orbitals.[10] Moreover, it has been shown very recently that the "artificial atoms" of gold nanoparticles bind with ligands to form divalent "artificial molecules".[6,25]

This paper presents that when the octet rule is satisfied, gold nanoparticles, like artificial atoms, dispersed in water are considered to attain special stability in derivatization with 5'-phosphorothioate-modified oligonucleotides inducing gold nanospheres to be connected linearly by duplexes. The linear strands of DNA-linked gold nanospheres are fixated by reducing Ag^+. The growth of coreshell structures may be accomplished by the successive reduction of one ionic metal over another. However, it often leads to form fresh second-metal particles as well as shells around first-metal cores.[1,8,9] This drawback has been overcome by immobilizing and reducing second-metal silver ions around duplexes, as DNA templates employed for platinum ion clusters,[27] to cap the duplexes-linked first-metal nanospheres of gold.

A. 3. Experimental Details

Reasonably monodisperse gold nanospheres of two different sizes having average diameters of 9.8 nm and 12.9 nm dispersed in water were prepared by reducing 1.0 mM

HAuCl$_4$(aq) with sodium citrate(aq).[16,28] The concentration of gold nanospheres was determined by measuring absorbance at 520 nm, where the extinction coefficient was estimated to be 2.4 x 10^8 M^{-1}cm^{-1}. 5'-Phosphorothioate-modified oligonucleotides[18] of TAT-AAG-CAA-AAT-3' [12-mer], 5'(phosphorothioate)-ATA-ACC-ATT-GTA-AAT-TAA-TTA-3' [21-mer], and 5'(phosphorothioate)-GGG-CGC-CGT-TCA-CCA-CGC-CTT-CGG-ACC-GGG-TCG-GCA-ACT-CCA-3' [42-mer] and their respectively complementary strands were purchased from Bioneer and employed to derivatize gold nanospheres. Oligonucleotide-modified gold nanospheres dispersed in water were prepared by adding a 3.1 mL aqueous solution containing a 150 nM oligonucleotide to 25 mL of the gold nanosphere colloidal solution at 20 ℃. The colloidal solution was then added with 3.2 mL of an aqueous solution containing 1 mM Tris buffer (pH = 7.2), 5 mM EDTA, 5 M NaF, and 0.1 M PVP. 5 mL of this colloidal solution was mixed with 5 mL of a gold colloidal solution modified with a mutually complementary oligonucleotide to prepare an aqueous colloidal solution of gold nanospheres linked via mutually complementary double-stranded 12-, 21-, and 42-mers (12-, 21-, and 42-duplexes, respectively). The concentration of duplexes in the solution is the same as that of the nanospheres (7.4 nM). Duplexes-linked gold nanospheres are fixated with silver to be [Ag]/[Au] = 1, if unspecified otherwise, by adding 80 L of 0.10 M AgNO$_3$(aq) and 40 L of 0.10 M hydroquinone(aq) to 10 mL of the above colloidal solution.

Energy-dispersive X-ray (EDX) profiles and high-resolution transmission electron microscopy (HRTEM) images were measured with a JEOL JEM 3000F microscope while

transmission electron microscopy (TEM) images with a JEOL JEM 2000 microscope. Absorption spectra were monitored by using a Scinco S 3100 spectrometer.

A. 4. Results and Discussion

The TEM images of Figure A-1 show that gold nanospheres having an average diameter of 9.8 nm can be linearly connected well by 12-duplexes or 21-duplexes. One might say that gold nanoparticles are aggregated, rather than connected by duplexes, linearly by accident during drying processes for TEM measurements. However, Table A-1 indicates that the average interparticle distance of a duplexes-linked gold nanoparticle strand increases with the length of the connecting DNA. This suggests that the linear connection of gold nanospheres via DNA is energetically preferential when the concentration of duplexes is the same as that of the nanoparticles.[16–18]
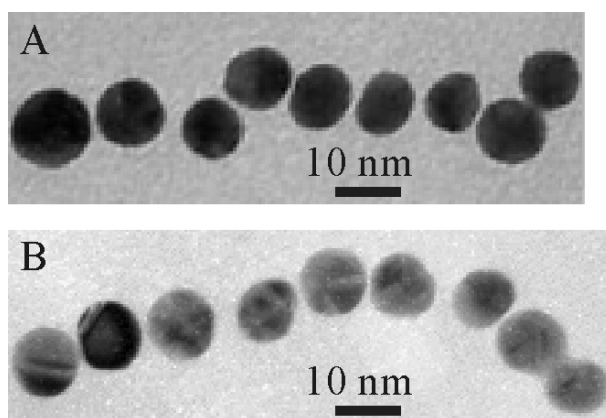

Figure A-1 TEM images of nine gold nanospheres connected linearly via 12-duplexes (A) and 21-duplexes (B).

Furthermore, Figure A-2 shows evidently the preferentially linear connection of gold nanospheres by duplexes. Figures A-2A and B reveal that duplexes-linked gold nanoparticle strands are encapsulated and fixated with silver by adding hydroquinone to reduce Ag^+ ions clustered around duplexes.[15–18,29] Thus, the stability of linearly connected gold nanoparticle strands have been increased substantially by silver coating. However, Figure A-2C designates that gold nanoparticles connected via lengthy duplexes cannot be fixated at the same experimental conditions owing to the large interparticle distances of gold nanoparticles. Although the strand of gold nanospheres connected by 12-duplexes is well fixated, that of gold nanospheres by 42-duplexes is hardly fixated with silver. The nanoparticles of Figure A-2C are bigger on the average than those of Figure A-2A although the average initial sizes of employed gold nanospheres were the same each other (Figure A-2 and Table A-1). The reason of this is that reduced silver in Figure A-2C was utilized to form the shells of gold nanospheres only whereas that in Figure A-2A was also spent to encapsulate connecting duplexes as well. Both particles and DNA are encapsulated well to be fixated for short duplexes-linked gold nanoparticle strands with reduction of Ag^+ ions whereas particles only are capped without being bridged with silver. Because Ag^+ ions clustered around duplexes

Table A-1 Particle Sizes and Interparticle Distances of Duplexes-Linked Gold Nanoparticle Strands

Figure	DNA	Ag^+ reduction	d^a (nm)	l^b (nm)
A-1A	12-duplexes	no	9.8	10.5
A-1B	21-duplexes	no	9.8	11.3
A-2A	12-duplexes	yes	10.3	9.6
A-2B	21-duplexes	yes	11.6	10.9
A-2C	42-duplexes	yes	12.9	13.9

[a] Average diameter of gold nanoparticles, measured perpendicularly to the axis of a strand.
[b] Average distance between the centers of two neighboring gold nanoparticles.

are reduced on metallic surfaces,[10] silver is built up preferentially on gold surfaces near

duplexes to bridge gold nanoparticles through short duplexes. Thus, the middle positions of

lengthy duplexes are hardly conjugated via silver because of the large space. Nevertheless,

we suggest that gold nanoparticles connected by 42-duplexes in Figure A-2C can also be

fixated with silver by reducing Ag^+ ions extensively. The average distances between the

centers of gold nanoparticles are 9.6, 10.9, and 13.9 nm in Figures A-2A, A-2B and A-2C,

respectively, showing that the distances between gold nanoparticles are correlated with the

lengths of DNA (Table A-1). This also indicates that gold nanoparticles are connected

linearly via oligonucleotide duplexes indeed. However, our TEM images taken with dried

samples are not considered to give us quantitative correlation between the distance and the

length because the free volume of DNA is mainly due to the existence of water.[30] It is
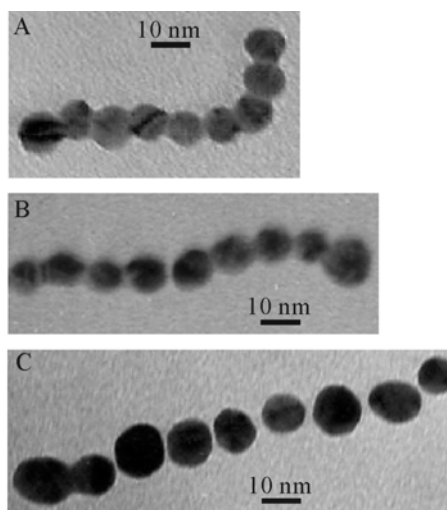

Figure A-2 TEM images of nine gold nanospheres connected linearly via 12-duplexes (A), 21-duplexes (B), and 42-duplexes (C) after reduction of Ag^+ to be [Ag]/[Au] = 1. Note that the actual initial particles of A and B before reduction of Ag^+ are not the same particles shown in A and B of Figure A-1, respectively.

noteworthy in Table A-1 that although the average particle sizes of gold nanospheres linked by both 12-duplexes and 21-duplexes have been increased, their average interparticle distances have been decreased due to strongly binding metallic bridges between gold nanoparticles with reduction of Ag^+ ions. Metallic bridges are considered to exclude water molecules near duplexes to reduce the volume of DNA.[30] This also supports that gold nanoparticles are connected linearly by duplexes and that duplexes-linked gold nanoparticle strands are fixated well.

The absorption of DNA at 260 nm decreases with mixing gold colloidal solutions modified with respectively complementary oligonucleotides as the hybridization of mutually complementary DNA strands is reported to reduce DNA absorption.[12,13] Besides, the surface plasmon absorption of gold nanoparticles shifts to the red by 5.3 nm with the formation of 21-duplexes-linked gold nanoparticle strands (Figure A-3). These suggest that DNA-linked gold nanoparticle strands are produced by the hybridization of mutually complementary DNA strands. Figure A-3 also shows that the reduction of Ag^+ ions in a colloidal solution of gold nanoparticles linked via hybridized DNA strands induces the surface-plasmon resonances of gold nanoparticles at 522 nm[9] to disappear gradually with the molar ratio of [Ag]/[Au] while it causes two broad plasmon absorption bands of silver nanorods to appear newly around 410 nm and above 700 nm at a high value of [Ag]/[Au].[3,12,13] The absorption bands around 410 and above 700 nm are attributed to the transverse and the longitudinal modes of silver nanorods or nanowires produced by coating DNA-linked gold nanoparticle strands with silver. The featureless broad absorption of the longitudinal modes above 700 nm suggests that the

aspect ratios of silver nanorods or nanowires are extremely diverse. The disappearance of gold absorption indicates that silver encloses gold nanoparticles as well as connecting duplexes thoroughly.
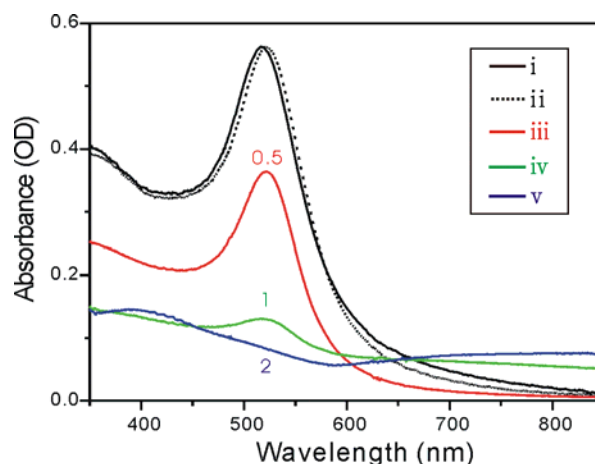

Figure A-3 Absorption spectra of gold nanospheres derivatized by 21-duplexes in water before (i) and after hybridization (ii) and those of gold nanospheres linked by 21-duplexes and dispersed in water after reducing various concentrations of Ag^+ (iii-v). The ratios of [Ag]/[Au] after reduction are given near the individual spectra of iii-v.

Along these lines, TEM images in Figure A-4 as well as the new appearance of silver nanorod absorption with reduction of Ag^+ ions in Figure A-3 designate that duplexes-linked gold nanoparticle strands are already present before reduction of Ag^+ ions and that the linear structures of the TEM images of Figures A-1 and A-2 are indeed due to preferentially linear connection, rather than linear aggregation by accident during drying processes for TEM measurements.[17] The TEM image of Figure A-5 also shows that the linear structures of duplexes-linked gold nanoparticles have been produced on a large scale and fixated with reduction of Ag^+ ions.
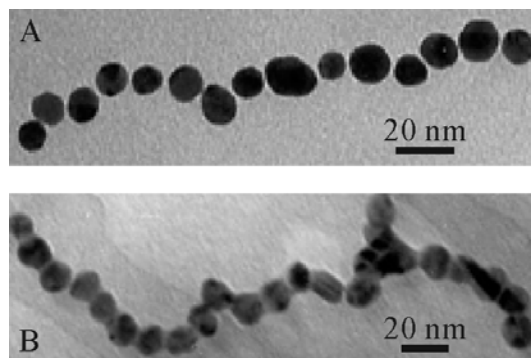
Figure A-4 TEM images of 21-duplexes-linked gold nanoparticle strands before (A) and after silver coating at [Ag]/[Au] = 1 (B).
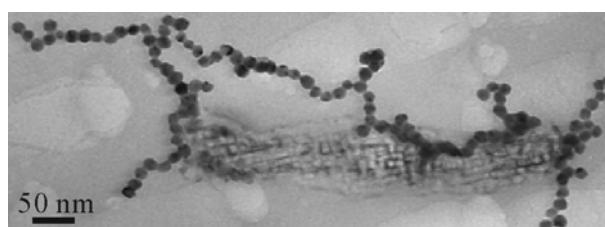
Figure A-5 TEM image on a large scale of 21-duplexes-linked gold nanoparticle strands after silver coating at [Ag]/[Au] = 1.

EDX line-intensity profiles of gold and silver scanned parallel and perpendicularly to the axis of a gold nanosphere strand after reduction of Ag^+ with hydroquinone also show that silver encapsulates and fixates the linear strand of duplexes-connected gold nanoparticles (Figure A-6).[11] The profile of silver is uniform along the strand (top of Figure A-6), suggesting that silver is reduced to encapsulate both the particles and the duplexes of the strand well.[31] The flat intensity profile of silver in the transverse direction of the gold nanoparticle strand (bottom of Figure A-6) also designates that silver is present to form a shell of the linear structure. We have found by examining magnified HRTEM images that junctions between gold nanoparticles are well fixated by silver to show the typical crystalline

130

fcc structures of silver. The observed fringe spacing of 0.29 nm agrees well with the literature value of the separation between the (110) lattice planes of silver although gold and silver have very close lattice spacing. Considering these with Figures A-2 and A-3, we suggest that Ag$^+$ ions clustered around duplexes[11] are reduced to coat duplexes-linked gold nanoparticle strands entirely.
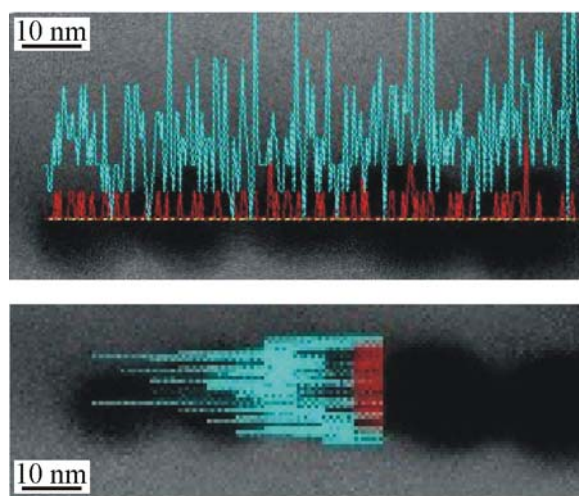
Figure A-6 EDX elemental intensity profiles of gold (blue) and silver (red), line-scanned parallel (top) and perpendicularly at a waist (bottom) to the axis of a 21-duplexes-linked gold nanosphere strand after reduction of Ag$^+$.

We have shown in the above that gold nanospheres act as artificial atoms to form artificial molecules of DNA-linked gold nanoparticle strands.[14,15] It is well known[32] that nanoparticles such as gold nanospheres have size-dependent optical and electronic properties. This suggests that gold nanospheres of different sizes may act as different types of artificial atoms. In this manner, a linear artificial molecule consisting of two different types of artificial atoms[5,6] has been produced by hybridizing two mutually complementary oligonucleotides, to which gold nanospheres of two different sizes are bound (Figure A-7). This also supports

131

that the linear connection of gold nanospheres via DNA is energetically favorable when the concentration of duplexes is the same as that of the nanoparticles.[17]
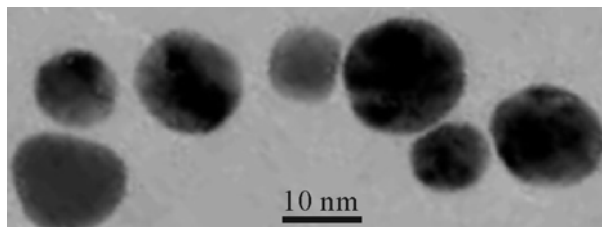

Figure A-7 TEM images of three large and three small gold nanoparticles linked alternatively each other by 21-duplexes.

The question is what causes the preferentially linear connection of gold nanopaticles by duplexes. As shown in Figure A-8A, we speculate that gold nanoparticles like artificial atoms[5,6,22,23] attain special stability in derivatization with 5'-phosphorothioate-modified oligonucleotides when the octet rule is satisfied. The hybridization of two mutually complementary oligonucleotides, to which gold nanoparticles are considered to be bound with satisfaction of the octet rule, makes gold nanospheres preferentially connected linearly by duplexes to produce strands like linear artificial molecules (Figure A-8B).[5,6,27] It is suggested that the derivatization of a gold nanosphere with a 5'-phosphorothioate-modified DNA molecule can occur by forming two covalent bonds between the sulfur and the oxygen atoms of the molecule and the surface of the particle,[33] as shown in Figure A-8A. Once a modified DNA molecule binds to a gold nanosphere via forming two covalent bonds, another molecule approaches the particle at the opposite side of the bound DNA molecule, owing to electrostatic repulsion between DNA molecules, to form two covalent bonds with the

nanosphere. We have found that the derivatization of gold nanoparticles at high temperature above 50 °C brings about multi-oligonucleotide modification. Figures A-1-7 have shown that the hybridization of two mutually complementary oligonucleotides bound to gold nanospheres produces linear strands of duplexes-linked gold nanoparticles. This is considered to suggest that derivatization attains special stability when two 5'-phosphorothioate-modified oligonucleotide molecules bind to a gold nanosphere. In other words, a gold nanoparticle is suggested to attain special stability in derivatization when the octet rule is satisfied by forming four covalent bonds with two modified DNA molecules. This also suggests the artificial-atomic nature of gold nanospheres. Then, gold nanospheres of different sizes may act as different types of artificial atoms. Figures A-7 and A-8B suggest that one can synthesize a linear artificial molecule consisting of two different types of artificial atoms by hybridizing two mutually complementary oligonucleotides, to which two different-size gold nanoparticles are bound.
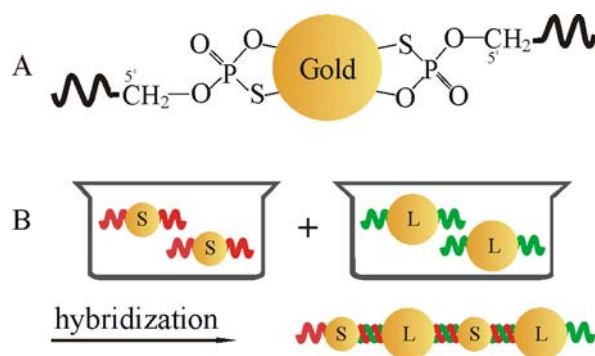
Figure A-8 Scheme suggesting that a gold nanosphere like an artificial atom attain special stability when it satisfies the octet rule in derivatization with 5'-phosphorothioate-modified oligonucleotides (A) and that the hybridization of two mutually complementary oligonucleotides, to which two different-size gold nanospheres of S and L are bound with satisfaction of the octet rule, yields a strand like a linear artificial molecule of $(SL)_n$ (B).

A. 5. Conclusions

Artificial atoms of gold nanospheres having average diameters of 10 nm are preferentially connected linearly by 12-, 21-, and 42-duplexes to form linear artificial molecules of duplexes-linked gold nanoparticle strands. The linear structures of the artificial molecules are then fixated by reducing Ag^+ ion clusters immobilized around duplexes to show the absorption spectrum of silver-coated artificial-molecular nanorods. We suggest that derivatization attains special stability when two 5'-phosphorothioate-modified oligonucleotide molecules bind to a gold nanosphere. In other words, a gold nanoparticle is speculated to attain special stability in derivatization when the octet rule is satisfied by forming four covalent bonds with two modified DNA molecules. Linear artificial molecules consisting of two different types of artificial atoms have been synthesized as well by hybridizing two mutually complementary oligonucleotides, to which two different-size gold nanoparticles are bound.

## A. 6. Acknowledgments

A. 7. References

[1] C. Burda, X.B. Chen, R. Narayanan, M.A. El-Sayed, Chem. Rev. 105 (2005) 1025.

[2] M.R. Kim, J.Y. Kim, D.-J. Jang, Eur. Phys. J. D 43 (2007) 279.

[3] R.C. Jin, Y.W. Cao, C.A. Mirkin, K.L. Kelly, G.C. Schatz, J.G. Zheng, Science 294 (2001) 1901.

[4] P.K. Jain, I.H. El-Sayed, M.A. El-Sayed, Nano Today 2 (2007) 18.

[5] G.A. Devries, M. Brunnbauer, Y. Hu, A.M. Jackson, B. Long, B.T. Neltner, O. Uzun, B.H. Wunsch, F. Stellacci, Science 315 (2007) 358.

[6] D.F. Perepichka, F. Rosei, Angew. Chem. Int. Ed. 46 (2007) 6006.

[7] H. Wang, Y.P. Wu, B. Lassiter, C.L. Nehl, J.H. Hafner, P. Nordlander, N.J. Halas, Proc. Natl. Acad. Sci. USA 103 (2006) 10856.

[8] S.J. Kim, C.S. Ah, D.-J. Jang, Adv. Mater. 19 (2007) 1064.

[9] J.H. Hodak, A. Henglein, M. Giersig, G.V. Hartland, J. Phys. Chem. B 104 (2000) 11708.

[10] H. Wang, D.W. Brandl, P. Nordlander, N.J. Halas, Acc. Chem. Res. 40 (2007) 53.

[11] R.C. Jin, G.S. Wu, Z. Li, C.A. Mirkin, G.C. Schatz, J. Am. Chem. Soc. 125 (2003) 1643.

[12] O.-H. Kwon, S. Lee, D.-J. Jang, Eur. Phys. J. D 34 (2005) 243.

[13] D. Zanchet, C.M. Micheel, W.J. Parak, D. Gerion, S.C. Williams, A.P. Alivisatos, J. Phys. Chem. B 106 (2002) 11758.

[14] A. Kumar, M. Pattarkine, M. Bhadbhade, A.B. Mandale, K.N. Ganesh, S.S. Datar, C.V. Dharmadhikari, M. Sastry, Adv. Mater. 13 (2001) 341.

[15] M. Fischler, U. Simon, H. Nir, Y. Eichen, G.A. Burley, J. Gierlich, P.M.E. Gramlich, T. Carell, Small 3 (2007) 1049.

[16] C.A. Mirkin, R.L. Letsinger, R.C. Mucic, J.J. Storhoff, Nature 382 (1996) 607.

[17] D. Lee, S. Lee, H. Kim, D.-J. Jang, Eur. Phys. J. D 24 (2003) 303.

[18] L. Jiang, H. Zhang, J. Zhuang, B. Yang, W. Yang, T. Li, C. Sun, Adv. Mater. 17 (2005) 2066.

[19] R. Wirtz, C. Wälti, P. Tosch, M. Pepper, A.G. Davies, W.A. Germishuizen, A.P.J. Middelberg, Langmuir 20 (2004) 1527.

[20] J.M. Petroski, T.C. Green, M.A. El-Sayed, J. Phys. Chem. A 105 (2001) 5542.

[21] A.A. Lazarides, K.L. Kelly, T.R. Jensen, G.C. Schatz, J. Mol. Struct. 529 (2000) 59.

[22] M.A. Kastner, Phys. Today 46 (1993) 24.

[23] U. Banin, Y.W. Cao, D. Katz, O. Millo, Nature 400 (1999) 542.

[24] A.J. Quinn, G. Redmond, Prog. Solid State Chem. 33 (2005) 263.

[25] N. Nilius, T.M. Wallis, W. Ho, Science 297 (2002) 1853.

[26] R.C. Ashoori, Nature 379 (1996) 413.

[27] R. Seidel, L.C. Ciacchi, M. Weigel, W. Pompe, M. Mertig, J. Phys. Chem. B 108 (2004) 10801.

[28] K.C. Grabar, R.G. Freeman, M.B. Hommer, M.J. Natan, Anal. Chem. 67 (1995) 735.

[29] T.M.-H. Lee, H. Cai, I.-M. Hsing, Electroanalysis 16 (2004) 1628.

[30] D. Rentzeperis, D.W. Kupke, L.A. Marky, Biopolymers 33 (1993) 117.

[31] A. Rai, M. Chaudhary, A. Ahmed, S. Bhargava, M. Sastry, Mater. Res. Bull. 42 (2007) 1212.

[32] S. Shukla, A. Priscilla, M. Banerjee, R.R. Bhonde, J. Ghatak, P.V. Satyam, M. Sastry, Chem. Mater. 17 (2005) 5000.

[33] Y. Tai, M. Watanabe, J. Murakami, K. Taijiri, J. Mater. Sci. 42 (2007) 1285.

B. Electrophoretic Separation of Gold Nanoparticles According to Bifunctional Molecules-Induced Charge and Size[†]

B. 1. Abstract

Gold nanospheres modified with bifunctional molecules have been separated and characterized by using agarose gel electrophoresis as well as optical spectroscopy and electron microscopy. The electrophoretic mobility of a gold nanosphere capped with 11-mercaptoundecanoic acid (MUA) has been found to depend on the number of MUA molecules per gold nanosphere (R_{MG}), indicating that it increases with the surface charge of the nanoparticle. The extinction spectrum of gold nanospheres capped with MUA at a R_{MG} value of 1,000 and connected via 1,6–hexanedithiol (HDT) decreases by 33% in magnitude and shifts to the red as largely as 22 nm with the increase of the molar ratio of HDT to MUA (R_{HM}). Gold nanospheres capped with MUA and connected via HDT have been separated successfully using gel electrophoresis and characterized by measuring reflectance spectra of discrete electrophoretic bands directly in the gel and by monitoring transmission electron microscope images of gold nanoparticles collected from the discrete bands. Electrophoretic mobility has been found to decrease substantially with the increment of R_{HM}, indicating that the size of aggregated gold nanoparticles increases with the concentration of HDT.

B. 2. Introduction

Noble metal nanostructures having functional properties attract considerable attention because they can be employed potentially in a diverse range of technology.[1–7] Their surfaces have often been modified because of their attractive potential in the miniaturization of devices and in the usage of bioanalysis.[8–13] Oligonucleotide-decorated gold nanoparticles can be organized in a solution[14,15] through highly specific hybridization between complementary DNA strands attached to gold nanospheres, which are emerging as promising tools to emit light on cellular processes.[16–18] The ligand molecules bind specifically to their corresponding receptor molecules on the surface of other nanoparticles, helping to avoid unwanted crosslinking that eventually leads to the flocculation of the nanoparticles.[19–21] However, it has not been easy to directly synthesize nanoparticles that are decorated with a specific number of ligand molecules on the surface of them.[22] On the other hand, nanoparticles modified with desired ligand molecules having particular functional groups can be sorted by controlling the number of the ligand molecules.[22–24] Thus, it is necessary to develop efficient separation methods for the characterization of metal nanoparticles.[22,25–30]

Electrophoretic nanoanalysis techniques are well established and widely used in a variety of fields including chemistry, biochemistry, and pharmacology because they provide inexpensive and efficient tools for quality assurance and safety control.[31] Although gel electrophoresis has been commonly used to separate biomolecules, it can also be employed to separate noble metal nanoparticles with direct observation of colors induced by surface-

plasmon resonances.[32–34] The electrophoretic separation of metal nanoparticles derivatized with surfactant molecules has been employed in order to develop a method suitable for separating a wide range of nanoparticles.[25] We have reported that various silver nanoplates transformed by laser pulses can be separated using agarose gel electrophoresis.[34] Gold nanorods stabilized by monofunctional and bifunctional polyethylene glycol (PEG) have also been separated by agarose gel electrophoresis because bifunctional PEG provides anchor points to attach either small gold nanoparticles or specific biomolecules.[31] In addition, the electrophoretic separation method using agarose gel has been investigated to compare the sizes of nanoparticles modified by complex molecules.[35] Compared with other separation techniques such as centrifugation,[36] high-performance liquid chromatography,[37] capillary electrophoresis,[38] diafiltration,[39] or size-exclusion chromatography,[40] the agarose gel electrophoretic separation method has the advantage of allowing multiple runs in parallel on the same gel.[1] This is a considerable advantage at stages of understanding mechanisms and optimizing conditions.

In this article, we present that gold nanoparticles have been derivatized by 11–mercaptoundecanoic acid (MUA) and 1,6–hexanedithiol (HDT) and then electrophoretically separated according to charge and size, which have been controlled by changing the molecular numbers of both the bifunctional derivatants on a nanoparticle. The electrophoretic mobility of a MUA–capped gold nanosphere has been found to depend on the number of MUA attached on the surface of the gold nanosphere. The extinction spectrum of gold nanospheres capped with MUA and connected via HDT shifts to the red with the increase of

the molar ratio of HDT to MUA (R_{HM}). The electrophoretic mobility of MUA–capped gold nanospheres has been found to decrease substantially with the increment of the R_{HM} value, indicating that the aggregation of gold nanospheres increases with the concentration of HDT.

B. 3. Experimental Details

The analytical grade chemicals of $HAuCl_4$(s), sodium citrate(s), MUA(s), HDT(l), and 10 x Tris-borate-EDTA (TBE) buffer(aq, pH 9.5) were used as purchased from Sigma-Aldrich. Megabased agarose was purchased from Biorad and used without further purification. Deionized water with a resistivity of greater than 18 MΩ cm, from a Millipore Milli-Q system, was used throughout the experiments. Gold nanospheres, having an average diameter of 9.8 nm with a standard deviation of 0.7 nm, dispersed in water were prepared by reducing 1.0 mM $HAuCl_4$ with sodium citrate.[14,41] The concentration of gold nanospheres was determined to be 9.5 nM by measuring absorbance at 518 nm, where the extinction coefficient of the surface-plasmon absorption was reported to be 2.4 x 10^8 M^{-1} cm^{-1}.[41–43] Gold nanospheres were capped with MUA by mixing gold hydrosols with given amounts of an aqueous MUA solution. The molar ratio of MUA to gold nanospheres (R_{MG}) was varied from 0 to 50,000 (Figure B-1). Gold nanospheres capped with MUA at R_{MG} values of 1,000 and 10,000 were typically used for experiments. MUA–capped gold nanospheres were then connected by dithiol molecules of HDT. R_{HM} was varied from 0 to 100.
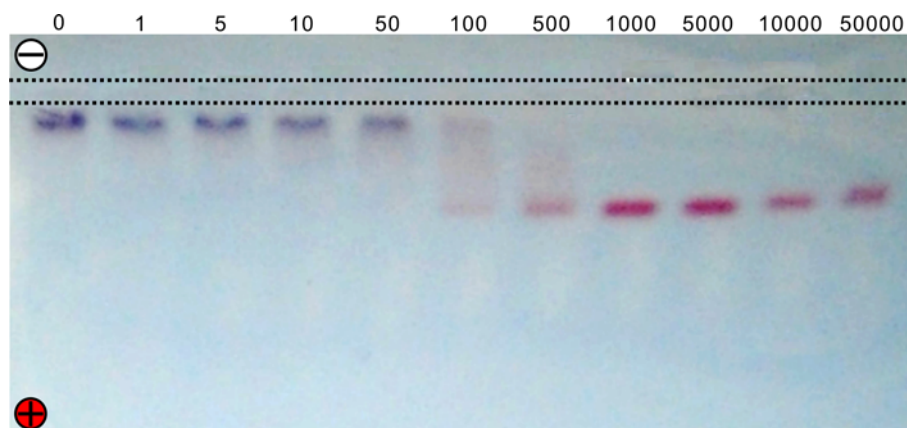
Figure B-1 True color photographs of an aqueous 0.5% agarose gel run for 30 min at 100 V in 1 × TBE buffer. Gold nanospheres were capped with MUA at indicated R_{MG} values before electrophoresis.

Absorption spectral changes of surface-plasmon resonances for a 2 mL aqueous colloidal solution of gold nanospheres contained in a quartz cell having a path length of 10 mm were monitored by using a UV/vis spectrophotometer (Scinco, UVS3100). A drop of a colloidal solution was placed on a carbon-coated copper grid and allowed to dry in the air to examine microscopic images of gold nanospheres using a transmission electron microscope (TEM, Hitachi, H-7600). For electrophoresis, an aqueous 0.5%m/m agarose gel was prepared and immersed in 1 x TBE buffer.[34] Considering the migration velocity of nanoparticles and the transmittance of samples,[22,34] we have chosen 0.5% as the optimal concentration of the agarose gel. The gel of 20 x 24 cm^2 having a thickness of 3 cm was run in a horizontal electrophoresis system having an electrode spacing of 30 cm (Biorad, Sub-Cell Model 192) for 30 min at 100 V while its extinction was monitored using a reflectance spectrometer (StellarNet, EPP2000C UV-VIS). Each electrolyte was prepared afresh prior to use. Gel

142

images were taken with a consumer digital camera (Nikon, D80) and processed only with slight linear contrast adjustments in order to give true color photographs of the visual gel appearance. Since the sample dispensing step of planar gel electrophoresis was conducted manually by using a pipette, special attention was paid to the dispersion of nanoparticles prior to sampling.[34] The mobility of a sample was determined repeatedly by measuring the sample position from the start position where the sample had been loaded. All of the experiments were performed at room temperature.

B. 4. Results and Discussion

Figures B-1 and B-2 show that the electrophoretic mobility of a MUA–capped gold nanosphere depends on the number of MUA molecules attached on the surface of the gold nanosphere. In order to give negative charges to the surfaces of gold nanospheres, MUA was selected as the capping agent. Gold nanospheres having an average diameter of 9.8 nm have been derivatized by MUA at diverse R_{MG} values. Although bifunctional molecules of MUA were covalently attached to the surface of gold nanospheres, the nanoparticles were still dispersed stably in the electrolytic solution through electrostatic repulsion.[33] The carboxylate group of MUA has made gold nanospheres migrate to the anodic electrode in an electric field. An appropriate choice of R_{MG} values has prevented retardation in the migration of gold nanospheres in an agarose gel. This has been confirmed by comparing the migration

143

of gold nanospheres capped with MUA at different R_{MG} values in gel electrophoresis. At or above a R_{MG} value of 1,000, MUA–capped gold nanospheres have migrated uniformly with showing a well-defined electrophoretic band in the gel (Figure B-1). This indicates that the electrophoretic mobility of a gold nanosphere increases with the surface charge of the nanoparticle induced by MUA. Thus, it is suggested that the functionalization of gold nanospheres using MUA molecules allows to introduce electrostatic double layers for the separation of the nanoparticles under aqueous conditions. Gold nanospheres capped with MUA at R_{MG} values of 0, 1, and 10 have been found to migrate hardly in the gel (Figure B-1). The flocculation of gold nanoparticles at the loading position has induced absorption shift from green to orange to show a blue band. However, gold nanospheres at a R_{MG} value of 100 begin to migrate and those at or above a R_{MG} value of 1,000 migrate well in the gel with maintaining a red band (Figure B-1). Gold nanospheres with negative charges have been found to migrate toward the positive pole. The electrophoretic mobility of a gold nanosphere at or above a R_{MG} value of 1,000 has been found to be sufficiently large to migrate in the gel. This suggests that electrophoretic mobility in our electrophoresis method using an agarose gel can be controlled well by the surface functionalization of metal nanoparticles. Gold nanospheres capped with MUA at a R_{MG} value of 1,000 have been found to have the most well-defined electrophoretic band with the largest electrophoretic mobility (Figure B-1). Thus, the optimum value of R_{MG} in our electrophoretic separation method is 1,000, implying that a R_{MG} value of 1,000 could be an appropriate value for the real electrophoretic separation of gold nanoparticles.
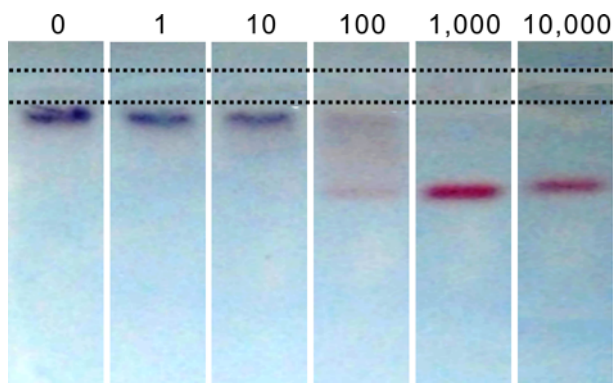
Figure B- 2 True color photographs of an aqueous 0.5% agarose gel run for 30 min at 100 V in 1 × TBE buffer. Gold nanospheres were capped with MUA at indicated R_{MG} values before electrophoresis.

Table B-1 Optical and Electrophoretic Changes of MUA-Capped Gold Nanoparticles with Variation of R_{HM} at a R_{MG} Value of 1,000.

R_{HM}	λ_{max}[a]	Mobility $[m^2\,V^{-1}\,s^{-1}]$[b]
0	518	7.1×10^{-7}
1	519	7.3×10^{-7}
5	521	6.8×10^{-7}
10	525	6.1×10^{-7}
50	530	4.8×10^{-7}
100	540	3.7×10^{-7}

[a] Wavelength at the absorption maximum of gold nanoparticles. [b] Relative errors are within ±2%.

Figure B-3 shows that the extinction of gold nanospheres capped with MUA and connected via HDT decreases with the increase of R_{HM}. This suggests that HDT molecules have made MUA–derivatized gold nanoparticles aggregate together. The HDT molecules in a colloidal solution of MUA–capped gold nanospheres induce the surface-plasmon resonances of gold nanoparticles at 518 nm to shift gradually to the red with the increase of the R_{HM} value (Figures B-4 and B-5), because MUA–capped gold nanospheres have been connected

to each other via HDT molecules to form aggregated nanoparticles (see below). As shown in Figure B-3, the extinction spectrum of MUA–capped gold nanospheres in the presence of HDT decreases in magnitude and shifts to the red compared with that in the absence of HDT. The extinction spectrum of gold nanospheres capped with MUA at a R_{MG} value of 1,000 decreases by 33% in magnitude and shifts to the red by 22 nm gradually with the increase of the R_{HM} value (Table B-1). Also, the extinction spectrum of gold nanospheres capped with MUA at a R_{MG} value of 10,000 decreases by 47% in magnitude and shifts to the red by 30 nm gradually with the R_{HM} value. This suggests that gold nanospheres capped with MUA at a R_{MG} value of 10,000 aggregate via HDT more readily than those at a R_{MG} value of 1,000 do. We thus suggest that unbound MUA anions and their counter cations of Na^+ at a R_{MG} value of 10,000 make the ionic strength of the colloidal solution at pH 9.5 be larger to flocculate
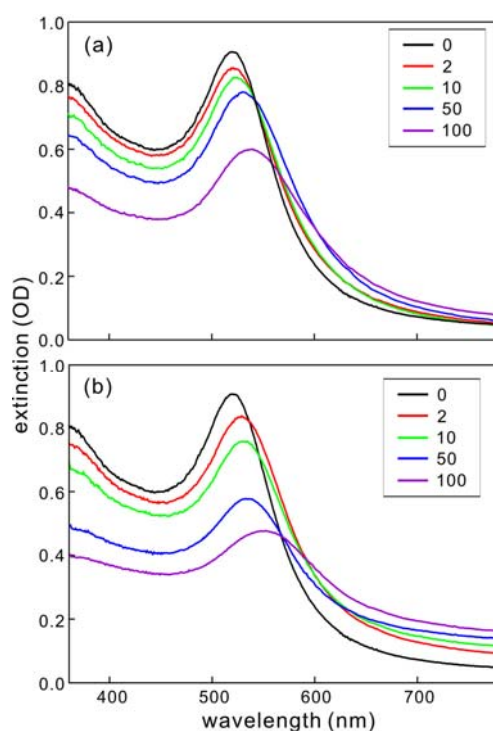

Figure B-3 Extinction spectra of gold nanospheres capped with MUA at R_{MG} values of (a) 1,000 and (b) 10,000 and connected via HDT at indicated R_{HM} values.

gold nanoparticles together more easily than those at a R_{MG} value of 1,000 do.[8, 22]
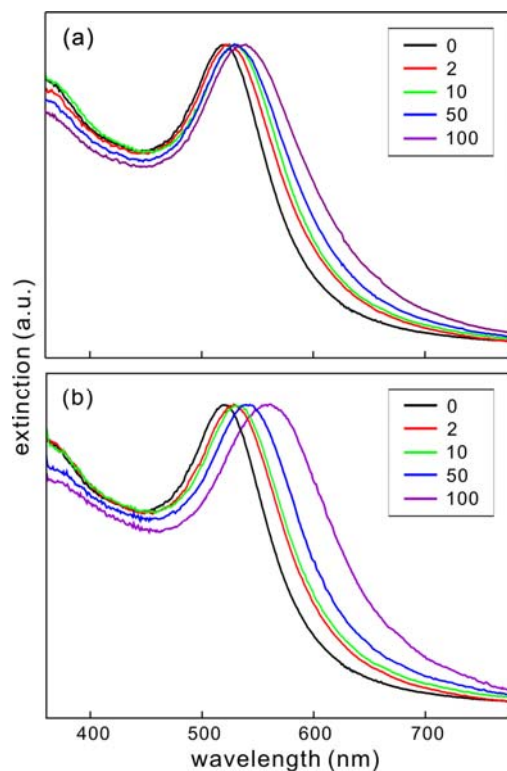

Figure B-4 Peak-normalized extinction spectra of gold nanospheres capped with MUA at R_{MG} values of (a) 1,000 and (b) 10,000 and connected via HDT at indicated R_{HM} values.

The TEM images of Figure B-6 show that gold nanospheres having an average diameter of 9.8 nm with a standard deviation of 0.7 nm have been capped with MUA at a R_{MG} value of 1,000 and connected by HDT molecules. The aggregation of MUA–capped gold nanospheres increases with R_{HM}, suggesting that HDT molecules interconnect gold nanospheres together. Thus, Figure B-6 indicates that the decrease and the red shift of the extinction spectra of gold nanospheres with the increase of R_{HM}, shown in Figure B-3, are due to the aggregation of gold nanospheres induced by HDT molecules.[4,14] FigureB-6 suggests that we can control the sizes of MUA–capped gold nanospheres for electrophoretic separation by adjusting R_{HM} values.
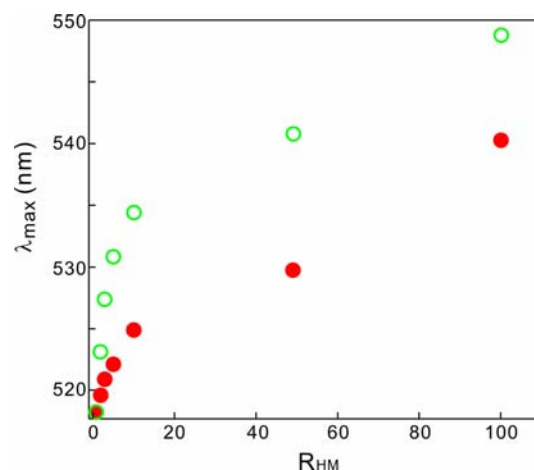
Figure B-5 Wavelength changes of the extinction maxima of gold nanospheres having R_{MG} values of 1,000 (closed) and 10,000 (open) with R_{HM}.

Figure B-7 shows that the electrophoretic mobility of a gold nanosphere depends on the number of HDT molecules attached on the surface of the gold nanoparticle. The electrophoretic mobility of gold nanoparticles at a R_{MG} value of 1,000 decreases gradually with R_{HM}, because HDT molecules induce MUA–capped gold nanospheres to aggregate together (Figures B-3 and B-6). The mobility of a gold hydrosol in our electrophoresis method using an agarose gel decreases with R_{HM} because bigger gold nanoparticles experience more friction from the gel. The apparent electrophoretic mobility, m_{app}, of a gold
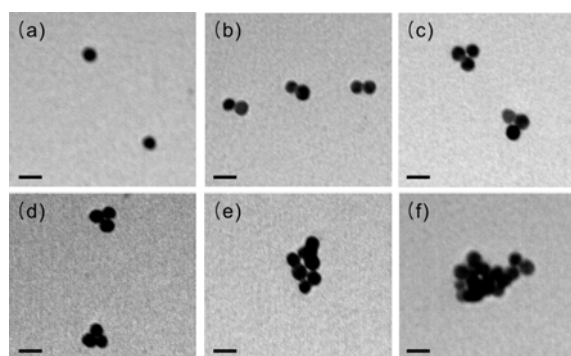

Figure B-6 TEM images of gold nanospheres capped with MUA at a R_{MG} value of 1,000 and connected via HDT at R_{HM} values of (a) 0, (b) 1, (c) 5, (d) 10, (e) 50, and (f) 100. Each scale bar indicates 10 nm.

nanoparticle has been determined approximately by the equation of $m_{app} = (L_{tot} L_{eff}) / (V_{sep} t_{sep})$.[34,44] L_{tot} is the total length of the separation medium (distance between two electrodes in the applied apparatus), L_{eff} is the migrated distance of the analyzed particle, t_{sep} is the time of separation, and V_{sep} is the applied voltage of the system. The value of m_{app} became as small as 3.7 x 10^{-7} $m^2 V^{-1} s^{-1}$ at a R_{HM} value of 100 whereas it was 7.1 x 10^{-7} $m^2 V^{-1} s^{-1}$ in a HDT–free condition (Table B-1). We have found that the electrophoretic mobility of MUA–capped gold nanoparticles also depends on the degree of their aggregation. A close examination of Figure B-7 reveals that two electrophoretic bands are observable at or above a R_{HM} value of 10. We consider that the band near the loading position is due to flocculated gold nanoparticles while the band moved to the positive electrode to show m_{app} is due to aggregated but not flocculated gold nanoparticles. Thus, Figure B-7 suggests that the flocculation, as well as aggregation, of MUA–capped gold nanospheres is induced by HDT molecules. Because gold nanoparticles flocculate at large R_{HM} values, they should not be connected severely to eliminate flocculation.
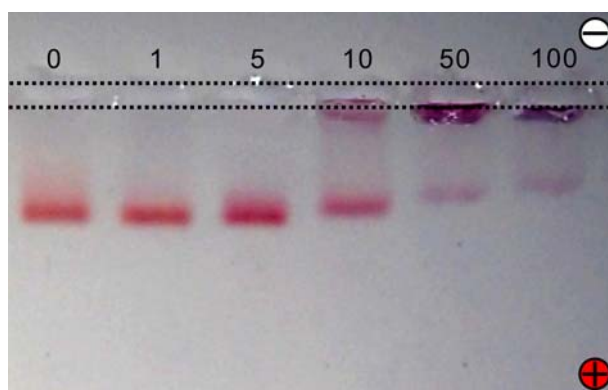

Figure B-7 True color photographs of an aqueous 0.5% agarose gel run for 30 min at 100 V in 1 × TBE buffer. Before electrophoresis, gold nanospheres were capped with MUA at a R_{MG} value of 1,000 and connected via HDT at R_{HM} values indicated inside.

Figure B-8 shows that the electrophoretic separation of a mixed sample of gold nanoparticles capped with MUA at a R_{MG} value of 1000 and connected via HDT at R_{HM} values of 1 and 50 has been made using our electrophoresis method with an agarose gel. The two discrete electrophoretic bands of Figure B-8a indicate that the gold nanoparticles having different R_{HM} values in a mixture sample have been separated well. The electrophoretic mobility of the MUA-capped gold nanoparticles having a R_{HM} value of 50 is lower than that of the MUA-capped gold nanoparticles having a R_{HM} value of 1. The colors on the gel are induced by the aggregation-dependent surface-plasmon resonances of gold nanoparticles. The reflectance spectra of two discrete electrophoretic bands having different R_{HM} values of 1 and 50 were measured directly on the gel (Figure B-8b). The reflectance extinction spectrum of MUA–capped gold nanospheres connected via HDT at a R_{HM} value of 50 is shifted to the red by 13 nm compared with that at a R_{HM} value of 1. The panels of Figure B-8c and d indicate that our gel electrophoretic method is efficient for the post-synthetic separation of metal nanoparticles. Conventional carbon-coated copper TEM grids were inserted at the places of the indicated bands by cutting the gel slightly with a surgical knife. After the gel was run for additional 3 min, gold nanoparticles were deposited on the grids. Representative TEM images obtained from the indicated two bands of Figure B-8a are presented in Figure B-8c and d. We consider that our electrophoretic separation method using an agarose gel is suitable for separating a wide range of metal nanoparticles such as gold nanoparticles coated with bifunctional molecules.

150
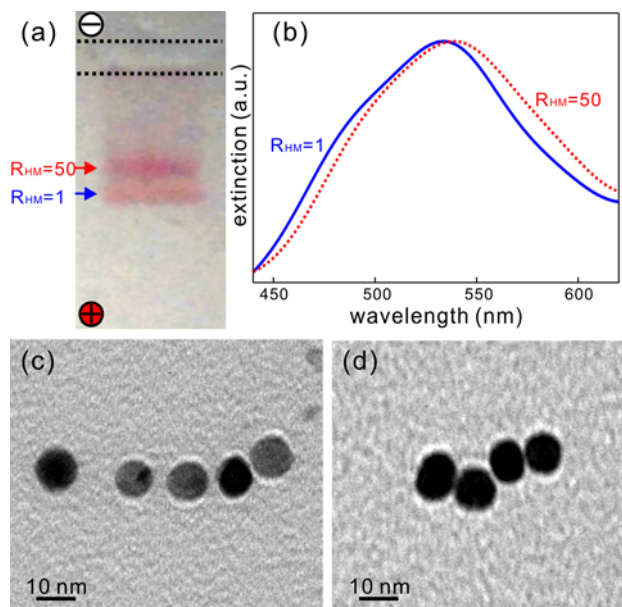
Figure B-5 (a) True color photograph of a 0.5% agarose gel run for 30 min at 100 V in 1 × TBE buffer. The sample before electrophoresis was a mixture of MUA–capped (at a R_{MG} value of 1,000) gold nanospheres connected via HDT at a R_{HM} value of 1 and those at a R_{HM} value of 50. (b) Normalized reflectance spectra of two electrophoretic bands having indicated R_{HM} values in the gel of *a*. (c, d) TEM images of gold nanospheres collected in the two bands having R_{HM} values of (c) 1 and (d) 50 in the gel of *a*.

B. 5. Conclusions

The electrophoretic mobility of a gold nanosphere capped covalently with MUA depends on R_{MG}, indicating that it increases with the surface charge of the nanoparticle. Thus, electrophoretic mobility in our electrophoresis method using an agarose gel can be controlled well by the surface functionalization of metal nanoparticles. Gold nanospheres capped with MUA at R_{MG} value of 1,000 have been found to have the most well-defined electrophoretic band with the largest electrophoretic mobility, suggesting that the optimum value of R_{MG} in our electrophoretic method is 1,000. Compared with the extinction spectrum of gold nanospheres in the absence of HDT, that of gold nanospheres capped with MUA at a R_{MG} value of 1,000 decreases by 33% in magnitude and shifts to the red by 22 nm with the increase of R_{HM}. Unbound MUA anions and their counter cations of Na^+ have made the ionic strength of the colloidal solution be large to flocculate gold nanoparticles together. The decrease and the red shift of the extinction spectra of gold nanospheres with the increase of R_{HM} are also due to the aggregation of gold nanospheres induced by HDT molecules. The electrophoretic mobility of MUA–capped gold nanoparticles depends on the degree of aggregation. A mixture of gold nanospheres connected via HDT at different R_{HM} values has been separated successfully using gel electrophoresis and characterized by measuring reflectance spectra of discrete electrophoretic bands directly in the gel and by monitoring transmission electron microscope images of gold nanoparticles collected from the discrete bands. Thus, we suggest that our electrophoretic separation method using an agarose gel is suitable for separating a wide range of metal nanoparticles.

B. 6. Acknowledgments

B. 7. References

[1] Hanauer, M., Pierrat, S., Zins, I., Lotz, A., Sönnichsen, C., *Nano Lett.* 2007, *7*, 2881–2885.

[2] Narayanan, R., El-Sayed, M. A., *J. Phys. Chem. B* 2005, *109*, 12663–12676.

[3] Hsieh, Y.-L., Chen, T.-H., Liu, C.-P., Liu, C.-Y., *Electrophoresis* 2005, *26*, 4089–4097.

[4] Kim, J.-Y., Kim, S. J., Jang, D.-J., *J. Phys. Chem. C* 2011, *115*, 672–675.

[5] Hutter, E., Fendler, J. H., *Adv. Mater.* 2004, *16*, 1685–1706.

[6] Wang, Y. Q., Nikitin, K., McComb, D. W., *Chem. Phys. Lett.* 2008, *456*, 202–205.

[7] Petrova, H., Lin, C.-H., Hu, M., Chen, J. Y., Siekkinen, A. R., Xia, Y. N., Sader, J. E., Hartland, G. V., *Nano Lett.* 2007, *7*, 1059–1063.

[8] López-Viota, J., Mandal, S., Delgado, A. V., Toca-Herrera, J. L., Möller, M., Zanuttin, F., Balestrino, M., Krol, S., *J. Colloid Interf. Sci.* 2009, *332*, 215–223.

[9] Aubin, M.-E., Morales, D. G., Hamad-Schifferli, K., *Nano Lett.* 2005, *5*, 519–522.

[10] Nehilla, B. J., Vu, T. Q., Desai, T. A., *J. Phys. Chem. B* 2005, *109*, 20724–20730.

[11] Kist, T. B. L., Mandaji, M., *Electrophoresis* 2004, *25*, 3492–3497.

[12] Soto, C. M., Blum, A. S., Wilson, C. D., Lazorcik, J., Kim, M., Gnade, B., Ratna, B. R., *Electrophoresis* 2004, *25*, 2901–2906.

[13] Sperling, R. A., Liedl, T., Duhr, S., Kudera, S., Zanella, M., Lin, C.-A. J., Chang, W. H., Braun, D., Parak, W. J., *J. Phys. Chem. C* 2007, *111*, 11552–11559.

[14] Kim, J.-Y., Lee, D. H., Kim, S. J., Jang, D.-J., *J. Colloid Interf. Sci.* 2008, *326*, 387–391.

[15] Parak, W. J., Pellegrino, T., Micheel, C. M., Gerion, D., Williams, S. C., Alivisatos, A. P., *Nano Lett.* 2003, *3*, 33–36.

[16] Aaron, J., Travis, K., Harrison, N., Sokolov, K., *Nano Lett.* 2009, *9*, 3612–3618.

[17] Voliani, V., Ricci, F., Luin, S., Beltram, F., *J. Mater. Chem.* 2012, *22*, 14487–14493.

[18] Voliani, V., Ricci, F., Signore, G., Nifosi, R., Luin, S., Beltram, F., *Small* 2011, *7*, 3271–3275.

[19] Wangoo, N., Bhasin, K. K., Mehta, S. K., Suri, C. R., *J. Colloid Interf. Sci.* 2008, *323*, 247–254.

[20] Dougherty, G. M., Rose, K. A., Tok, J. B.-H., Pannu, S. S., Chuang, F. Y. S., Sha, M. Y., Chakarova, G., Penn, S. G., *Electrophoresis* 2008, *29*, 1131–1139.

[21] Wang, Z. C., Tan, B., Hussain, I., Schaeffer, N., Wyatt, M. F., Brust, M., Cooper, A. I., *Langmuir* 2007, *23*, 885–895.

[22] Surugau, N., Urban, P. L., *J. Sep. Sci.* 2009, *32*, 1889–1906.

[23] Pellegrino, T., Sperling R. A., Alivisatos, A. P., Parak, W. J., *J. Biomed. Biotechnol.* 2007, *2007*, 26796.

[24] Hasenoehrl, C., Alexander, C. M., Azzarelli, N. N., Dabrowiak, J. C., *Electrophoresis* 2012, *33*, 1251–1254.

[25] Sperling, R. A., Pellegrino, T., Li, J. K., Chang, W. H., Parak, W. J., *Adv. Funct. Mater.* 2006, *16*, 943–948.

[26] Misra, T. K., Liu, C.-Y., *J. Nanopart. Res.* 2009, *11*, 1053–1063.

[27] Bercovici, M., Lele, S. K., Santiago, J. G., *J. Chromatogr. A* 2009, *1216*, 1008–1018.

[28] Oszwaldowski, S., Zawistowska-Gibula, K., Roberts, K. P., *Anal. Bioanal. Chem.* 2011, *399*, 2831–2842.

[29] Liu, F.-K., *J. Chromatogr. A* 2009, *1216*, 2554–2559.

[30] Mesgari, S., Poon, Y. F., Yan, L. Y., Chen, Y., Loo, L. S., Thong, Y. X., Chan-Park, M. B., *J. Phys. Chem. C* 2012, *116*, 10266–10273.

[31] Pierrat, S., Zins, I., Breivogel, A., Sönnichsen, C., *Nano Lett.* 2007, *7*, 259–263.

[32] Tanaka, T., Jin, H., Miyata, Y., Kataura, H., *Appl. Phys. Exp.* 2008, *1,* 114001(1)–114001(3).

[33] Xu, X. Y., Caswell, K., Tucker, E., Kabisatpathy, S., Brodhacker, K. L., Scrivens, W. A., *J. Chromatogr. A* 2007, *1167*, 35–41.

[34] Kim, J.-Y., Kim, S. J., Jang, D.-J., *J. Sep. Sci.* 2009, *32*, 4161–4166.

[35] Sperling, R. A., Liedl, T., Duhr, S., Kudera, S., Zanella, M., Lin, C.-A. J., Chang, W. H., Braun, D., Parak, W. J., *J. Phys. Chem. C* 2007, *111,* 11552-11559.

[36] Qiu, P. H., Mao, C. B., *Adv. Mater.* 2011, *23*, 4880–4885.

[37] Henglein, A., *J. Phys. Chem.* 1993, *97*, 5457-5471.

[38] Liu, F. K., Wei, G. T., *Anal. Chim. Acta* 2004, *510*, 77-83.

[39] Sweeney, S. F., Woehrle, G. H., Hutchison, J. E., *J. Am. Chem. Soc.* 2006, *128*, 3190-3197.

[40] Wei, G. T., Liu, F. K., Wang, C. R. C., *Anal. Chem.* 1999, *71*, 2085-2091.

[41] Lee, D., Lee, S., Jang, D.-J., *Eur. Phys. J. D* 2003, *24*, 303–306.

[42] Storhoff, J. J., Lazarides, A. A., Mucic, R. C., Mirkin, C. A., Letsinger, R. L., Schatz, G. C., *J. Am. Chem. Soc.* 2000, *122*, 4640–4650.

[43] Ackerman, G. A., Yang, J., Wolken, K. W., Histochem. J., *Cytochem.* 1983, *31*, 433–440.

[44] Liu, F.-K., *J. Chromatogr. A* 2007, *1167*, 231–235.

C. Laser-Induced Shape Transformation and Electrophoretic Analysis of Triangular Silver Nanoplates[†]

C. 1. Abstract

The shape transformation of silver triangular nanoplates induced by nanosecond laser pulses has been monitored using agarose gel electrophoresis as well as optical spectroscopy and electron microscopy. Laser irradiation truncates the vertices of the triangular nanoplates, having an average edge size of 110 nm and an average thickness of 14 nm, to form nearly regular-hexagonal and spherical silver nanoplates gradually. The surface-enhanced Raman scattering of 4-nitrobenzenethiol absorbed on silver nanoparticles has been found to decrease enormously with laser irradiation, showing its strong dependence on the shape transformation of nanostructures. Electrophoretic mobility values have been found to decrease substantially with the increase of irradiation time, indicating that the surface charge density of silver nanoplates has been modified largely by laser pulses.

C. 2. Introduction

Nanostructured materials having functional properties attract considerable attention because they can be employed potentially in a diverse range of technologies.[1–5] Metal nanostructures are particularly interesting scientifically as well as industrially, because they have possible uses in diverse applications such as catalysts, devices, transistors, and optoelectronics.[6–8] Once nanoparticles are formed in host materials, it is very difficult to change their sizes and shapes with available traditional technologies such as heating and chemical modification. However, laser irradiation can melt, reshape, or fragment nanoparticles without significantly perturbing the environment in glasses or other matrix media.[9–15] Since the heating is very selective, the laser-induced shape change of metal nanostructures provides simple means for post-preparation shape control.[11–17] Most of the early studies on the laser-induced change of metal nanoparticles were concentrated on the size reduction of noble metal particles as a breaking-down process to produce fine metal nanoparticles.[18–22] We have recently reported that not only the mutual transposition of the core and the shell of a Au@Pt core/shell nanosphere but also the excavation of the silver core of a Ag@Pt nanoparticle can be obtained by exciting the surface plasmon resonances of platinum with picosecond laser pulses to form a new, reversed core/shell Pt@Au nanosphere[16] and a hollow platinum nanospheres,[17] respectively. The laser-induced formation mechanism of noble metal nanostructures is not understood well yet although the laser-induced size reduction and shape alteration of gold nanoparticles in water have been

explained to occur through melting and vaporization.[11, 14, 20, 21] The dependence of melting temperatures on metals has been exploited to fabricate or alter metal nanocomposites optically.[9–17, 21, 22] Considered that the absorption coefficient of metallic particles depends on the particle size according to the Mie theory, it is feasible to excite nanoparticles size selectively using the wavelength tunability of the laser.

It is highly important to obtain monodispersed nanoparticles having specific sizes and shapes in order to define and exploit their properties well.[1,2] Alternatives to the direct synthesis of nanoparticles are the post-synthetic separation and modification of particles similar to cleaning procedures in organic synthesis.[23–25] Substantial endeavors have been made to purify nanoparticles based on sizes and shapes after preparation. As gel electrophoresis has been commonly used to separate biomolecules, noble-metal nanoparticles could be separated by the gel electrophoresis with observing directly their colors induced by plasmon resonances.[23–33] Relationship between the shape and the color allows direct visual or spectroscopic analysis of successful separations, which appear as multicolored lanes in a gel. Compared with other separation techniques, gel electrophoresis has the advantage of allowing multiple runs in parallel on the same gel.[23, 24, 27–33] The electrophoretic methods can provide inexpensive and efficient tools for quality assurance and safety control as well.[23–33] This is a considerable advantage at the stage of understanding mechanisms and optimizing conditions.

In this article, we present that the shape transformation of the triangular silver nanoplates can be obtained by exciting the surface plasmon resonances of silver nanoplates

159

with nanosecond laser pulses to produce nearly regular-hexagonal silver nanoplates (Figure C-1). The vertices of a triangular silver nanoplate were truncated gradually by laser irradiation. The triangular silver nanoplate was changed into a truncated triangular silver nanoplate, a nearly regular-hexagonal silver nanoplate, and then a spherical silver nanoplate with the increase of irradiation time. The laser-induced preparation of nearly regular-hexagonal silver nanoplates by controlling kinetic growth in liquid solutions is very limited, and nanoparticles of different shapes are often obtained from a mixture.
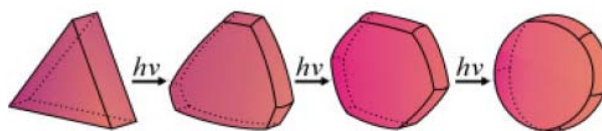

Figure C-1 Schematic diagram of the laser-induced shape transformation of a triangular silver nanoplate. Laser irradiation truncates the vertices of a triangular silver nanoplate gradually to form a truncated triangular nanoplate, a nearly regular-hexagonal nanoplate, and a spherical nanoplate sequentially.

C. 3. Experimental Details

The following analytic grade chemicals were purchased from Sigma-Aldrich and used without further purification: silver nitrate, hydrazine monohydrate, sodium chloride, sodium borohydride, 4-nitrobenzenethiol (4-NBT), trisodium citrate, and 10 x Tris-borate-EDTA (TBE) buffer (an aqueous solution of 0.89 M Tris, 0.02 M EDTA disodium, and 0.89M boric acid). Megabase agarose was purchased from Bio-Rad and used without further purification. Deionized water with a resistivity of greater than 18 MΩ cm (Millipore, Milli-Q System) was

used in the preparation of aqueous solutions. For the preparation of the aqueous colloidal solution of triangular silver nanoplates,[4] 0.5 mL of aqueous 59mM $AgNO_3$ and 1mL of aqueous 34 mM trisodium citrate were added to 98 mL of water with stirring for several minutes. Then, 0.5 mL of aqueous 20 mM $NaBH_4$ was added. The resultant solution was stirred for 1 h and aged for at least 24 h at room temperature before use. Silver nanoplates were prepared by enlarging these small silver seeds in the presence of citrate. Two solutions (1 and 2) were prepared. The solution 1 was prepared by injecting 0.9 mL of aqueous 40mM hydrazine, 0.3 mL of aqueous 40 mM trisodium citrate, and 0.4 mL of silver seeds to 60 mL of water. The solution 2 was prepared by adding 0.3 mL of aqueous 59 mM AgNO3 into 30 mL of water. Then, the solution 2 was added drop-by-drop into the solution 1 with vigorous stirring. The laser-induced shape transformation of silver triangular nanoplates was performed by irradiating 1mL of the above prepared silver colloid in a quartz cell having a pass length of 10mm with 6 ns pulses of 355 nm having an average energy of 3mJ from a Q-switched Nd:YAG laser (Quantel, Brilliant B) run at 10 Hz. A spot diameter of the laser beam was 5 mm at the sample. A drop of a colloidal solution was placed on a carbon-coated copper grid and allowed to dry in the air to examine the microscopic images of irradiated or unirradiated silver nanoplates using a transmission electron microscope (TEM, Hitachi, H-7600). For each sample, usually 300 particles from different parts of the grid were examined to estimate the shape distribution of nanoparticles. Absorption spectral changes of silver nanoplates with laser irradiation were monitored by measuring the absorption spectra of a sample contained in a quartz cell of 10mm light path using a UV/vis spectrometer (Scinco, S-3100). Raman spectra of 4-NBT adsorbed on the surfaces of silver nanoplates were measured

using a confocal microscope Raman system (OLYMPUS, BX41). The 514.5 nm radiation from an air cooled, Ar1 laser (Dynamic Laser, LS300) was used as the excitation source. In total 0.1 mL of 1mM 4-NBT in ethanol was added to 0.5 mL of an irradiated or unirradiated silver colloid contained in a centrifugal tube, shaken several times, and then allowed to stay for an hour to reach the adsorption equilibrium.[34, 35] The resulting colloid was then dropped on a quartz plate of 10 mm x 10 mm and dried completely for Raman measurements. Raman spectra of a silicon wafer at 520 cm^{-1} were used to calibrate the spectrometer, and the accuracy of the spectral measurement was estimated to be better than 1 cm^{-1}. For the electrophoresis of silver colloids, an aqueous 0.5%m/m agarose gel was prepared and immersed in 1 x TBE buffer. Agarose gel is most often used for the separation of nanoparticles by gel electrophoresis while TBE is the most common electrolyte.[23] Considering the migration velocity of nanoparticles and the transmittance of samples,[23, 24, 28–30] we have chosen 0.5%m/m as the optimal concentration of agarose gel. The gel of 7 x 7 cm^2 having a thickness of 1 cm was run in a horizontal electrophoresis system having an electrode spacing of 15 cm (Bio-Rad, Mini-Sub Cell GT System). All electrolytes were prepared afresh each day prior to use. Since the sample dispensing step of planar gel electrophoresis was conducted by manual pipetting, special attention was paid to the dispersion of nanoparticles prior to sampling.[23] Gel images were taken with a consumer digital camera (Nikon, D80) and processed only with slight linear contrast adjustments in order to give a true representation of the visual gel appearance. All the measurements were conducted at room temperature.

C. 4. Results and Discussion

The TEM image of Figure C-2a shows that silver nanoparticles as prepared are mostly triangular nanoplates in morphology, whose average edge size is 110 nm and whose average thickness is 14 nm. As indicated in Table C-1, other particles such as truncated triangular nanoplates, nearly regular-hexagonal nanoplates, and spherical nanoplates are also found to exist. Figure C-2 and Table C-1 indicate that the abundance of triangular nanoplates decreases while that of nearly regular-hexagonal nanoplates or that of spherical nanoplates increases with irradiation time. This suggests that laser irradiation truncates the vertices of triangular silver nanoplates gradually to increase the size distribution of silver nanoparticles consequently. The existence of numerous small spherical nanoparticles after irradiation for 60 min also supports this suggestion (Figure C-2c). The close examination of Figure C-2 hints that the kinetically formed initial rough surfaces of silver nanoplates have been transformed into energetically favorable smooth and round surfaces. Although silver nanoplates have experienced shape transformation apparently upon irradiation, their sizes have hardly been decreased except the truncation of vertices.
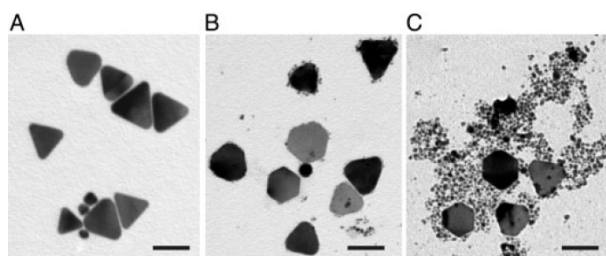

Figure C-2 TEM images of the triangular silver nanoplates after irradiation for 0 min (a), 10 min (b), and 60 min (c). Scale bars indicate 100 nm.

The spectrum of the sample without irradiation shows typical absorption for triangular silver nanoplates (Figure C-3a). There are a strong dipole resonance at 787 nm, a weak in-plane quadrupole resonance at 546 nm, and a third plasmon resonance due to out-of-plane quadrupole excitation at 354 nm.[4, 36] As laser irradiation goes on, the dipole resonances of the triangular silver nanoplates decrease substantially whereas the dipole resonances of small silver nanospheres at 392 nm start to increase mainly (Figure C-3). We consider that as triangular silver nanoplates have been reported to decompose into colloidal nanoparticles by laser pulses,[22] laser irradiation truncates the vertices of the triangular silver nanoplates to form nearly regular-hexagonal and spherical silver nanoplates gradually. Compared with triangular nanoplates, the dipole resonance peaks of nearly regular-hexagonal and spherical silver nanoplates are decreased due to the lack of sharp corners.[5] Although the dipolar resonances of silver nanoplates are reported to shift to the blue substantially with lamp irradiation,[37] they are found to shift to the red slightly with laser irradiation in our experiment. Considering our previous works on the melting of noble-metal nanoparticles,[15 –
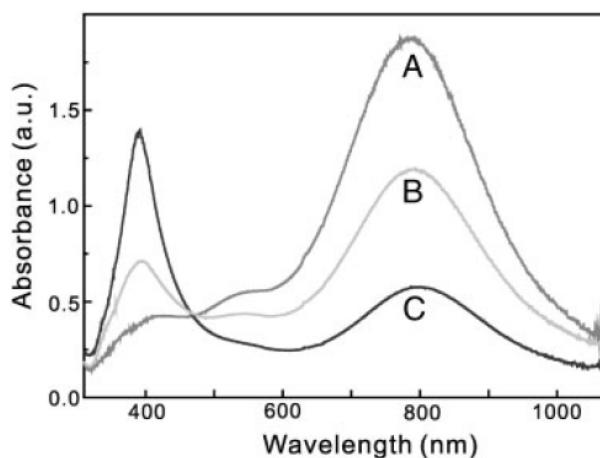

Figure C-3 Absorption spectra of the silver triangular nanoplates suspended in water after irradiation for 0 min (a), 10 min (b), and 60 min (c).

[17] we suggest that the thermalized photon energy of laser pulses melts the edges of silver nanoplates. This induces a silver nanoplate to have smooth rims, increasing the aspect ratio, that is, the ratio of the edge length to the thickness. The red shift of the dipolar resonance is thus attributed to the increase of the aspect ratios of silver nanoplates by laser irradiation.

Figure C-4 shows that the surface-enhanced Raman scattering (SERS) of 4-NBT absorbed on silver nanoparticles decreases enormously with irradiation time, revealing its strong dependence on the shapes of silver nanoplates. The complete absence of the S-H stretching peak in the SERS spectrum, observable at 2548 cm^{-1} for pure 4-NBT (not shown in Figure C-4), indicates that 4-NBT is adsorbed on silver as thiolate after S-H bond cleavage. Thus, all of the peaks in Figure C-4 can be attributed to 4-nitrobenzenethiolate.[34, 35] The prominent peak at 1335 cm^{-1} can be assigned to the symmetric stretching vibration of the nitro group [$v_s(NO_2)$]. The large intensity decrease of SERS peaks with laser irradiation suggests that the Raman enhancement of a triangular silver nanoplate is much higher than that of a nearly regular-hexagonal or a spherical silver nanoplate.[38] Thus, the truncation of
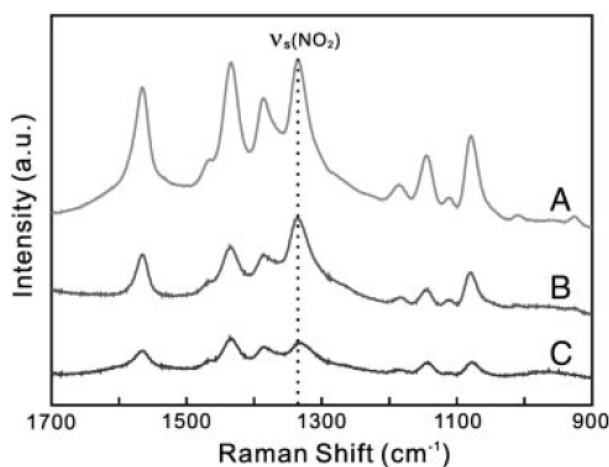

Figure C-4 SERS spectra of 4-NBT absorbed on the silver triangular nanoplates after irradiation for 0 min (a), 10 min (b), and 60 min (c) with excitation at 514.5 nm.

165

the vertices of a triangular silver nanoplate reduces the Raman enhancement effect of a silver nanostructure.

Figure C-5a shows the true color photographs of an aqueous 0.5%m/m agarose gel loaded with colloidal solutions of silver nanoplates and run multiply in parallel on the same gel for 30 min at 100 V (130 mA) in 1 x TBE buffer. The bands were directly visible due to the characteristic surface plasmon resonances of silver nanoparticles. It is known that although the nanorods and the spherical particles show a clear trend of electrophoretic mobility, triangular silver nanoplates do not.[23, 24] The separation is not perfect yet, which is most likely caused by a variation in the number charges per particle and the small overall particle charge. Nonetheless, the TEM images of the lane i suggest that our gel electrophoretic method is efficient for the postsynthetic separation of silver nanoparticles. The electrophoretic mobility decreases substantially with the increase of irradiation time (Table C-1), suggesting that the mobility depends strongly on the surface charge density of silver nanostructures as well as on the shapes of silver nanoparticles. The apparent electrophoretic mobility, m_{app}, of a silver nanoparticle has been determined approximately following the equation of $m_{app} = (L_{tot} L_{eff}) / (U_{sep} t_{sep})$, where L_{tot} is the total length of the separation medium (distance between two electrodes in the applied apparatus), L_{eff} is the migrated distance of the analyzed particle, t_{sep} is the time of separation, and U_{sep} is the applied voltage of the system. Triangular nanoplates are faster than nearly regular-hexagonal nanoplates or spherical nanoplates, and nearly regular-hexagonal nanoplates are faster than spherical nanoplates. The mobility of nanoplates does not show clear trend. Because

166

nanoplates are flat and their thickness cannot be determined from our TEM images, the mobility may have been influenced by hidden parameters.[23,24] The characteristic visible colors of the lane i for the sample without laser irradiation are due to the typical characteristic absorption bands of triangular silver nanoplates as discussed with Figure C-3a. Compared with the TEM images of Figure C-2, the TEM images of Figure C-5b show silver nanoparticles of uniform sizes and shapes, indicating that the gel electrophoresis separates mixed samples well into bands. In particular, small spherical nanoparticles produced by irradiation are hardly observable in Figure C-5b although they are found numerously in
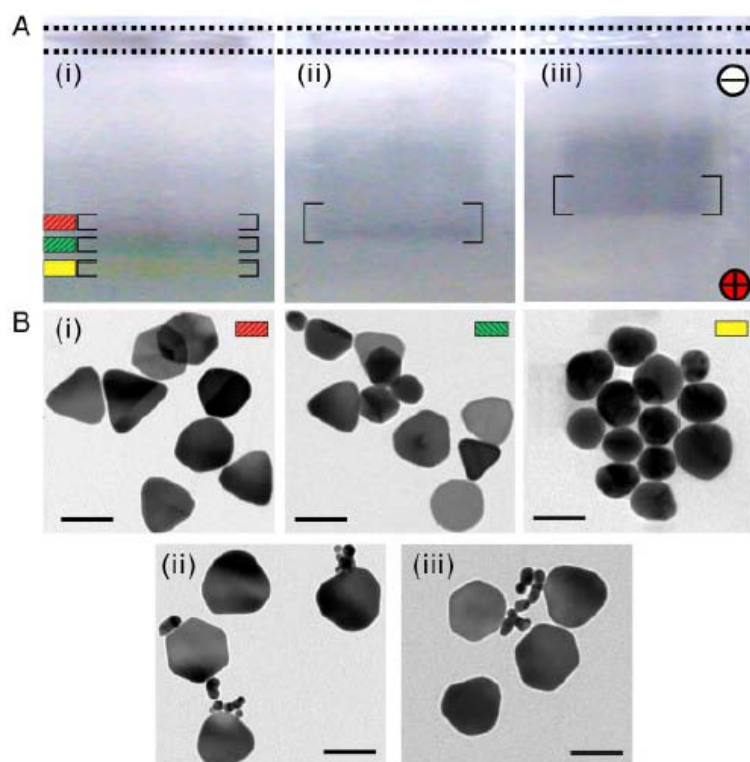

Figure C-5 True color photographs of an aqueous 0.5%m/m agarose gel run for 30 min at 100 V in 1 × TBE buffer (a) and TEM images of silver triangular nanoplates collected from gel positions indicated by brackets (b). Silver triangular nanoplates were irradiated for 0 min (i), 10 min (ii), and 60 min (iii) before electrophoresis. The dashed lines show the sample loading positions of the gel, and each scale bar indicates 100 nm.

Figure C-2c. This suggests that our agarose gel electrophoresis method is efficient in the separation of silver nanoplates. The electrophoretic band became broader with irradiation time. As discussed with Figure C-2, this also suggests that laser irradiation has increased the size distribution of silver nanoparticles.

Table C-1 Shape and Mobility Changes of Silver Nanoplates with Irradiation Time.

Figure	Irradiation time	TNP	Truncated TNP	HNP	SNP	Mobility ($m^2\,V^{-1}\,s^{-1}$)[a]
2a	0 min	48%	31%	15%	6%	4.5×10^{-8}
2b	10 min	40%	27%	19%	14%	3.8×10^{-8}
2c	60 min	36%	24%	22%	18%	3.2×10^{-8}

TNP, HNP, and SNP indicate triangular, nearly regular-hexagonal, and spherical nanoplates, respectively. [a] Relative errors are within ±8%.

C. 5. Conclusions

The shape transformation of silver triangular nanoplates induced by nanosecond laser pulses has been monitored using agarose-gel electrophoresis as well as optical spectroscopy and electron microscopy. Laser irradiation induced triangular silver nanoparticles to undergo shape transformation. The vertices of triangular silver nanoplates were truncated by laser irradiation to form truncated triangular nanoplates, nearly regular-hexagonal nanoplates, and spherical nanoplates sequentially. The existence of numerous small nanospheres supports this mechanism. The dipole resonances of the triangular silver nanoplates at 787 nm decreased largely whereas the dipole resonances of truncated small silver nanospheres at 392 nm started to increase mainly with laser irradiation. The SERS of 4-NBT absorbed on silver nanoparticles decreased enormously with laser irradiation time, showing its strong dependence on the shapes of nanostructures.

C. 6. Acknowledgments

C. 7. References

[1] Jain, P. K., Huang, X. H., El-Sayed, I. H., El-Sayed, M. A., *Acc. Chem. Res.* 2008, *41*, 1578 – 1586.

[2] Xu, X. Y., Ray, R., Gu, Y. L., Ploehn, H. J., Gearheart, L., Raker, K., Scrivens, W. A., J. Am. Chem. Soc. 2004, *126*, 12736-12737.

[3] Sherry, L. J., Jin, R. C., Mirkin, C. A., Schatz, G. C., Van Duyne, R. P., Nano Lett. 2006, *6*, 2060 – 2065.

[4] Zou, X. Q., Dong, S. J., *J. Phys. Chem. B* 2006, *110*, 21545 – 21550.

[5] Wiley, B. J., Im, S. H., Li, Z. Y., McLellan, J., Siekkinen, A., Xia, Y. N., *J. Phys. Chem. B* 2006, *110,* 15666 – 15675.

[6] Jin, R. C., Cao, T. W., Mirkin, C. A., Kelly, K. L., Schatz, G. C., Zheng, J. G., *Science* 2001, *294*, 1901 – 1903.

[7] Zhao, Q. T., Hou, L. S., Huang, R., Li, S. Z., *Mater. Chem. Phys.* 2004, *85*, 180 – 183.

[8] Griffin, J., Singh, A. K., Senapati, D., Lee, E., Gaylor, K., Jones-Boone, J., Ray, P. C., *Small* 2009, *5*, 839 – 845.

[9] Harada, M., Okamoto, K., Terazima, M., *Langmuir* 2006, *22*, 9142 – 9149.

[10] Harada, M., Okamoto, K., Terazima, M., *J. Colloid Interface Sci.* 2009, *332*, 373 – 381.

[11] Kurihara, K., Kizling, J., Stenius, P., Fendler, J. H., *J. Am. Chem. Soc.* 1983, *105*, 2574 – 2579.

[12] Link, S., Burda, C., Nikoobakht, B., El-Sayed, M. A., *J. Phys. Chem. B* 2000, *104*, 6152 – 6163.

[13] Zhao, C. J., Zhao, Q. T., Zhao, Q. Z., Qiu, J. R., Zhu, C. S., Guo, S. W., *J. Photochem. Photobiol. A-Chem.* 2007, *187*, 146 – 151.

[14] Callegari, A., Tonti, D., Chergui, M., *Nano Lett.* 2003, *3*, 1565–1568.

[15] Kim, S. J., Ah, C. S., Jang, D. J., *J. Nanopart. Res., in press*, DOI 10.1007/s11051-008-9565-y.

[16] Kim, S. J., Ah, C. S., Jang, D. J., *Adv. Mater.* 2007, *19*, 1064 – 1068.

[17] Ah, C. S., Kim, S. J., Jang, D. J., *J. Phys. Chem. B* 2006, *110*, 5486 – 5489.

[18] Kapoor, S., Palit, D. K., Mukherjee, T., *Chem. Phys. Lett.* 2001, *349*, 19 – 24.

[19] Brause, R., Möltgen, H., Kleinermanns, K., *Appl. Phys. B* 2002, *75*, 711 – 716.

[20] Takami, A., Kurita, H., Koda, S., *J. Phys. Chem. B* 1999, *103*, 1226 – 1232.

[21] Wang, Z. L., Petroski, J. M., Green, T. C., El-Sayed, M. A., *J. Phys. Chem. B* 1998, *102* 6145 – 6151.

[22] Zhao, Q. T., Hou, L. S., Zhao, C. J., Gu, S. P., Huang, R., Ren, S. H., *Laser Phys. Lett.* 2004, *1* 115 – 117.

[23] Surugau, N., Urban, P. L., *J. Sep. Sci.* 2009, *32*, 1889 – 1906.

[24] Hanauer, M., Pierrat, S., Zins, I., Lotz, A., Sönnichsen, C., *Nano Lett.* 2007, *7*, 2881 – 2885.

[25] Yang, L., Guihen, E., Glennon, J. D., *J. Sep. Sci.* 2005, *28*, 757 – 766.

[26] Zanchet, D., Micheel, C. M., Parak, W. J., Gerion, D., Alivisatos, A. P., *Nano Lett.* 2001, *1*, 32 – 35.

[27] Parak, W. J., Pellegrino, T., Micheel, C. M., Gerion, D., Williams, S. C., Alivisatos, A. P., *Nano Lett.* 2003, *3*, 33 – 36.

[28] Zanchet, D., Micheel, C. M., Parak, W. J., Gerion, D., Williams, S. C., Alivisatos, A. P., *J. Phys. Chem. B* 2002, *106*, 11758 – 11763.

[29] Aubin, M. E., Morales, D. G., Hamad-Schifferli, K., *Nano Lett.* 2005, *5*, 519 – 522.

[30] Sperling, R. A., Liedl, T., Duhr, S., Kudera, S., Zanella, M., Lin, C. A. J., Chang, W. H., Braun, D., Parak, W. J., *J. Phys. Chem. C* 2007, *111*, 11552 – 11559.

[31] Xu, X. Y., Caswell, K. K., Tucker, E., Kabisatpathy, S., Brodhacker, K. L., Scrivens, W. A., *J. Chromatogr. A* 2007, *1167*, 35 – 41.

[32] Liu, F. K., *J. Chromatogr. A* 2009, *1216*, 2554 – 2559.

[33] Pierrat, S., Zins, I., Breivogel, A., Sönnichsen, C., *Nano Lett.* 2007, *7*, 259 – 263.

[34] Han, S. W., Lee, I., Kim, K., *Langmuir* 2002, *18*, 182 – 187.

[35] Shin, K. S., Lee, H. S., Joo, S. W., Kim, K., *J. Phys. Chem. C* 2007, *111*, 15223 – 15227.

[36] Sarkar, A., Kapoor, S., Mukherjee, T., *J. Colloid Interface Sci.* 2005, *287*, 496 – 500.

[37] An, J., Tang, B., Ning, X. H., Zhou, J., Xu, S. P., Zhao, B., Xu, W. Q., Corredor, C.,

Lombardi, J. R., *J. Phys. Chem. C* 2007, *111*, 18055 – 18059.

[38] Tiwari, V. S., Oleg, T., Darbha, G. K., Hardy, W., Singh, J. P., Ray, P. C., *Chem. Phys.*

Lett. 2007, *446*, 77 – 82.

D. List of Publications

1. Mee Rahn Kim, **Jong-Yeob Kim**, and Du-Jeon Jang, "Electrochemical fabrication of arrayed alumina nanowires showing strong blue emission" *Eur. Phys. J. D* **2007**, *43*, 279.

2. **Jong-Yeob Kim**, Dong Hun Lee, Seol Ji Kim, and Du-Jeon Jang, "Preferentially linear connection of gold nanoparticles in derivatization with phosphorothioate oligonucleotides" *J. Colloid Interface Sci.* **2008**, *326*, 387.

3. **Jong-Yeob Kim**, Sunbae Lee, Kyung-Hwa Yoo, and Du-Jeon Jang, "Coulomb blockade effect and negative differential resistance in the electronic transport of bacteriorhodopsin" *Appl. Phys. Lett.* **2009**, *94*, 153301.

4. **Jong-Yeob Kim**, Seol Ji Kim, and Du-Jeon Jang, "Laser-induced shape transformation and electrophoretic analysis of triangular silver nanoplates" *J. Sep. Sci.* **2009**, *32*, 4161.

5. **Jong-Yeob Kim**, Mee Rahn Kim, Sun-Young Park, and Du-Jeon Jang, "Hydrothermal growth control of ZnSe·N$_2$H$_4$ nanobelts" *CrystEngComm* **2010**, *12*, 1803.

6. **Jong-Yeob Kim**, Seol Ji Kim, and Du-Jeon Jang, "Laser-induced fabrication of Au@CdS core-shell nanowires" *J. Phys. Chem. C* **2011**, *115*, 672.

7. Mee Rahn Kim, **Jong-Yeob Kim**, Seol Ji Kim, and Du-Jeon Jang, "Laser-induced fabrication of platinum nanoshells having enhanced catalytic and Raman properties" *Appl. Catal. A-Gen.* **2011**, *393*, 317.

8. **Jong-Yeob Kim**, Chil Seong Ah, and Du-Jeon Jang, "Controlled aspect ratios of gold nanorods in reduction-limited conditions" *J. Nanomater.* **2011**, 405853.

9. **Jong-Yeob Kim**, Hyeok Jeong, and Du-Jeon Jang, "Hydrothermal fabrication of well-ordered ZnO nanowire arrays on Zn foil: room-temperature ultraviolet nanolaser" *J. Nanopart. Res.* **2011**, *13*, 6699-6706.

10. Yeonho Kim, **Jong-Yeob Kim**, and Du-Jeon Jang, "One-pot and template-free fabrication of ZnS·(ethylenediamine)$_{0.5}$ hybrid nanobelts" *J. Phys. Chem. C* **2012**, *116*, 10296-10302.

11. Yu-Yang Zhang, **Jong-Yeob Kim**, Yeonho Kim, and Du-Jeon Jang, "Facile synthesis of highly luminescent water-soluble CdTe/CdS/ZnS quantum dots" *J. Nanopart. Res.* **2012**, *14*, 1117-1125.

12. **Jong-Yeob Kim**, Hyung-Bae Kim, and Du-Jeon Jang, "Electrophoretic separation of gold nanoparticles according to bifunctional molecules-induced charge and size" *Electrophoresis* **in press**.

13. Myounghee Son, Seol Ji Kim, **Jong-Yeob Kim**, and Du-Jeon Jang, "Laser-induced silver nanosoldering of gold nanoparticles" *Submitted to J. Nanosci. Nanotech.*.

14. **Jong-Yeob Kim**, Daeki Lee, Hark Jin Kim, Iseul Lim, Wan In Lee, and Du-Jeon Jang, "Annealing-free preparation of anatase TiO$_2$ nanopopcorns on Ti foil via a hydrothermal process and their photocatalytic and photovoltaic applications" *Submitted to J. Mater. Chem. A.*

E. List of Presentations

E. 1. International Presentations

1. Mee Rahn Kim, **Jong-Yeob Kim**, and Du-Jeon Jang, "Fabrication of arrayed alumina nanowires showing strong blue emission" *XIII International Symposium on Small Particles and Inorganic Clusters (ISSPIC13)*, Göteborg, Sweden (**2006**).

2. **Jong-Yeob Kim**, Dong Hun Lee, Seol Ji Kim, and Du-Jeon Jang, "Preferentially linear connection of gold nanoparticles via octet rule-satisfied derivatization with phosphorothioate oligonucleotide" *4th International Symposium of BK21 Chemistry & Molecular Engineering Division and 16th International Symposium of SNU-UT-NTU Chemistry Departments*, Seoul, Korea (**2008**).

3. Seol Ji Kim, Chil Seong Ah, **Jong-Yeob Kim**, and Du-Jeon Jang, "Optical fabrication of hollow and core-shell metal nanospheres" *Particles 2008: Particle Synthesis, Characterization, and Particle-Based Advanced Materials*, Orlando, FL, USA (**2008**).

4. **Jong-Yeob Kim**, Mee Rahn Kim, Sun-Young Park, and Du-Jeon Jang, "Control of the length-to-width ratios of ZnSe nanobelts by a solvothermal process" *XIV International Symposium on Small Particles and Inorganic Clusters (ISSPIC14)*, Valladolid, Spain (**2008**).

5. **Jong-Yeob Kim**, Sun-Young Park, and Du-Jeon Jang, "Solvothermal control of the length-to width ratios of ZnSe nanobelts" *Gorden Research Conferences on Clusters, Nanocrystals & Nanostructures*, South Hadley, MA, USA (**2009**).

6. **<u>Jong-Yeob Kim</u>**, Sunbae Lee, Kyung-Hwa Yoo, and Du-Jeon Jang, "Coulomb blockade effect and negative differential resistance in the molecular electronic transport of bacteriorhodopsin" *The 4th Winter School of Asian CORE*, Seoul, Korea (**2009**).

7. <u>Yeonho Kim</u>, **Jong-Yeob Kim**, and Du-Jeon Jang, "Synthesis, characterization, and formation mechanism of ZnS-based inorganic-organic hybrid nanobelts" *Gorden Research Conferences on Colloidal, Macromolecular & Polyelectrolyte Solutions*, Ventura, CA, USA (**2012**).

8. **Jong-Yeob Kim**, <u>Myounghee Son</u>, and Du-Jeon Jang, "ZnO nanowires fabricated hydrothermally for room-temperature" *Gorden Research Conferences on Colloidal, Macromolecular & Polyelectrolyte Solutions*, Ventura, CA, USA (**2012**).

9. **Jong-Yeob Kim**, <u>Daeki Lee</u>, and Du-Jeon Jang, "Well-ordered ZnO nanowire arrays for ultraviolet nanolasers" *XVI International Symposium on Small Particles and Inorganic Clusters (ISSPIC16)*, Leuven, Belgium (**2012**).

10. **Jong-Yeob Kim**, Daeki Lee, Hark Jin Kim, Iseul Lim, Wan In Lee, and Du-Jeon Jang, "Facile fabrication of anatase TiO_2 nanostructures for photocatalytic and photovoltaic applications" *Gorden Research Conferences on Nanomaterials for Applications in Energy Technology*, Ventura, CA, USA (**2013**).

E. 2. Domestic Presentations

1. Ji Yeon Park, **Jong-Yeob Kim**, and Du-Jeon Jang, "Fabrication and characterization of Rectangular ZnSe Nanoplates" *The 98th National Meeting of the Korean Chemical Society*, Gwangju, Korea (**2006**).

2. **Jong-Yeob Kim** and Du-Jeon Jang, "Formation mechanism of ZnSe nanobelts" *The 100th National Meeting of the Korean Chemical Society*, Daegu, Korea (**2007**).

3. Seol Ji Kim, **Jong-Yeob Kim**, and Du-Jeon Jang, "Laser fabrication and electrophoresis of platinum square nanoframes" *The 101st National Meeting of the Korean Chemical Society*, Goyang, Korea (**2008**).

4. **Jong-Yeob Kim**, Seol Ji Kim, and Du-Jeon Jang, "Laser-induced shape transformation and gel electrophoresis of silver nanoparticles" *The 101st National Meeting of the Korean Chemical Society*, Goyang, Korea (**2008**).

5. **Jong-Yeob Kim** and Du-Jeon Jang, "Solvothermally controlled length-to-width ratios of ZnSe nanobelts" *The 102nd National Meeting of the Korean Chemical Society*, Jeju, Korea (**2008**).

6. **Jong-Yeob Kim** and Du-Jeon Jang, "Electrophoretic analysis of the laser-induced shape transformation of silver nanoplates" *The 103rd National Meeting of the Korean Chemical Society*, Seoul, Korea (**2009**).

7. **Jong-Yeob Kim** and Du-Jeon Jang, "An approach to molecular electronic transport using bacteriorhodopsin" *The 104th National Meeting of the Korean Chemical Society*, Daegu, Korea (**2009**).

8. **Jong-Yeob Kim**, Chil Seong Ah, and Du-Jeon Jang, "Aspect ratios modification of gold nanorods in reduction-limited conditions" *The 105th National Meeting of the Korean Chemical Society*, Incheon, Korea (**2010**).

9. **Jong-Yeob Kim**, Hyeok Jeong, and Du-Jeon Jang, "Room-temperature ultraviolet emission of arrayed ZnO nanowires on Zn foil" *The 106th National Meeting of the Korean Chemical Society*, Daegu, Korea (**2010**).

10. **Jong-Yeob Kim** and Du-Jeon Jang, "Laser-induced synthesis of Au@CdS core-shell nanowires" *The 107th National Meeting of the Korean Chemical Society*, Jeju, Korea (**2011**).

11. Hyungbae Kim, **Jong-Yeob Kim**, and Du-Jeon Jang, "Synthesis and characterization of highly luminescent CdSe@ZnS core-shell nanorods" *The 107th National Meeting of the Korean Chemical Society*, Jeju, Korea (**2011**).

12. Yeonho Kim, **Jong-Yeob Kim**, and Du-Jeon Jang, "Facile hydrothermal growth control of highly luminescent ZnS nanobelts" *The 107th National Meeting of the Korean Chemical Society*, Jeju, Korea (**2011**).

13. Kyusik Han, **Jong-Yeob Kim**, and Du-Jeon Jang, "Catalytic properties of Pt nanoboxes synthesized via Galvanic replacement of Ag nanocubes" *The 108th National Meeting of the Korean Chemical Society*, Daejeon, Korea (**2011**).

14. Yeonho Kim, **Jong-Yeob Kim**, and Du-Jeon Jang, "Fabrication of $ZnS \cdot (EN)_{0.5}$ nanobelts via a solvothermal route and their characterization" *The 108th National Meeting of the Korean Chemical Society*, Daejeon, Korea (**2011**).

179

15. <u>Myounghee Son</u>, **Jong-Yeob Kim**, and Du-Jeon Jang, "Laser-induced nanowelding of gold and silver nanoparticles" *The 108th National Meeting of the Korean Chemical Society*, Daejeon, Korea (**2011**).

16. <u>Hyungbae Kim</u>, **Jong-Yeob Kim**, and Du-Jeon Jang, "Synthesis and characterization of photocatalytic CdSe-Pt composite nanorods" *The 108th National Meeting of the Korean Chemical Society*, Daejeon, Korea (**2011**).

17. <u>Myounghee Son</u>, **Jong-Yeob Kim**, and Du-Jeon Jang, "One-pot synthesis of Au@SiO$_2$ core-shell nanochains" *The 110th National Meeting of the Korean Chemical Society*, Busan, Korea (**2012**).

18. **<u>Jong-Yeob Kim</u>**, Yeonho Kim, and Du-Jeon Jang, "Fabrication and Characterization of Water-Soluble CdTe/CdS/ZnS Core-Shell-Shell Quantum Dots" *The 110th National Meeting of the Korean Chemical Society*, Busan, Korea (**2012**).

19. **Jong-Yeob Kim**, <u>Jae Won Lee</u>, and Du-Jeon Jang, "Laser Fabrication of Au@CdS One-Dimensional Nanocomposites" *The 110th National Meeting of the Korean Chemical Society*, Busan, Korea (**2012**).

20. <u>Yeonho Kim</u>, **Jong-Yeob Kim**, and Du-Jeon Jang, "Single-step hydrothermal synthesis of ZnS nanorods exhibiting enhanced band-edge emission" *The 110th National Meeting of the Korean Chemical Society*, Busan, Korea (**2012**).

Abstract (Korean)

독특한 광학적 성질을 갖고 있는 $ZnSe \cdot N_2H_4$ 나 ZnO 의 1 차원 나노구조체와 광촉매 및 광전성질을 갖고 있는 TiO_2 나노팝콘 그리고 $CdTe@CdS@ZnS$ 양자점을 수열적으로 간단하게 합성하고 그 나노재료의 구조적 특성과 광학적 특성을 체계적으로 연구하였다. 제조한 나노구조물의 특성은 전자 현미경 이미지와 전자 회절 패턴, 뿐만 아니라 자외선/가시광선 영역 흡수 및 형광방출 분광, X-ray 광전자, 라만 스펙트럼들을 분석함으로써 평가하였다. 또한 피코초 시간분해 형광분광학 장비를 이용하여 반도체 나노물질의 들뜬 상태에서의 전자 거동을 이해하였다. 1 장에서는 나노크기의 재료에서의 분광학적 특성평가와 나노입자의 제조방법에 대한 간략한 개요가 수록되어 있다. 독특한 광학적 성질을 갖는 나노입자를 다양한 방법을 통해 제조 및 구조제어하여 UV 레이저와 광촉매 장치 그리고 태양전지등에 응용하고 있다.

2 장에서 hydrazine hydrate 를 용매로 하여 $ZnSe \cdot N_2H_4$ 유무기 하이브리드 나노벨트를 수열적으로 제조하고 $ZnSe \cdot N_2H_4$ 나노벨트의 크기에 따라서 분광학적인 변화를 나타남 보여주었다. 비록 $ZnSe \cdot (diethylenetriamine)_{0.5}$ 나노벨트와 $ZnSe \cdot N_2H_4$ 마이크로막대에 관한 연구가 되어왔지만, $ZnSe \cdot N_2H_4$ 나노벨트의 제조 및 분광학적 특성파악에 대한 연구는 그동안 진행되지 않았다. $ZnSe \cdot N_2H_4$ 전구체 물질인 Se 과 $ZnCl_2$ 의 몰수 비가 증가할수록 광발광 스펙트럼이 점차 장파장으로 이동하였으며, 그 스펙트럼의 세기 또한 증가함을 알게 되었다. 또한 시간 분해능 분광학 실험을 통하여 Se 과 $ZnCl_2$ 의 몰수 비가

증가할수록 나노벨트의 들뜬 상태에서의 발광 평균 수명이 증가함으로 보여주면서 최적의 ZnSe·N₂H₄ 나노벨트 제조조건을 제시하였다.

3 장에서는 수열적 합성법을 통하여 ZnO 나노선을 Zn 포일 위에 직접 고르게 배열하여 성장시키고, 그 ZnO 나노선을 상온에서 거동 가능한 자외선 나노레이저의 성질을 보여준 연구에 대해 논하고 있다. ZnO 나노선은 열증착이나 금 촉매 기상증착과 같은 방법으로 제조해왔지만 에너지와 합성 장치에 대한 단점이 존재하였는데, 수열적 합성으로 간단하고 결정성이 좋은 상태에서 균일하게 배열되는 ZnO 나노선을 제조할 수 있음을 보여주었다. 또한, Zn 포일 위의 ZnO 나노선 집합체는 370-400 nm 파장대에서 25 kW cm^{-2} 의 전류 한계값을 얻었으며, 이것은 기존에 알려진 ZnO 나노막대 집합체의 전류 한계값보다 낮은 값을 보여준 것이다. 시간 분해능 분광학 연구로 나노선 집합체의 들뜬 상태에서 전자들이 free-exciton decay 와 bound-exciton decay 와 같은 두 개의 메커니즘에 의해 들뜬 전자가 이완되어 짐을 이해할 수 있었다.

4 장에서는 아나타제 TiO₂ 나노팝콘을 Ti 포일 위에 수열적 방법으로 직접 제조시킴으로써 다른 어닐링 과정 없이 광촉매 및 광전재료 물질로 응용한 연구를 서술하고 있다. H₂O₂ 및 HF과 H₂O의 부피비, VR(H₂O₂:HF:H₂O)를 변화하면서 TiO₂ 나노입자의 구조적 특성과 결정의 변화가 나타났으며, 그 중에서 VR(H₂O₂:HF:H₂O)이 1:1:1000 일 때의 TiO₂ 나노팝콘이 –Ti–O– 네트워크를 가장 잘 구성하고 있었으며 아나타제 결정성이 가장 좋았음을 확인하였다. VR(H₂O₂:HF:H₂O)이 1:1:1000으로 제조한 TiO₂ 나노팝콘의 3차원적 계층구조와 높은 아나타제 결정성 그리고 노출된 {001} 면에 의해 증강된 광촉매 활성을 보여주었으며, 이 TiO₂ 나노팝콘이 성장되어있는 Ti 포일을

작업전극으로 사용한 태양전지에서도 3.98%의 광전변환 효율을 얻게 되었다

마지막으로 5 장에서는 type-II 거동을 보이는 CdTe/CdS/ZnS 코어-쉘-쉘 양자점을 수용액 상태에서 Zn^{2+} 이온을 주입하여 간단하게 제조한 연구를 소개하고 있다. CdTe 와 ZnS 사이의 격자 부조합 정도가 높아서 CdS를 CdTe 와 ZnS 사이에 도입하여 격자의 부조합도를 낮추었다. 산성도와 반응온도, 그리고 Zn^{2+} 양을 조절하면서 흡광 및 발광과 같은 광학적 특성을 자유자재로 변화시킬 수 있었다. 특히 CdTe/CdS 양자점에서의 형광양자수율이 4% 가량 되었던 것이 CdTe/CdS/ZnS 양자점에서는 형광양자수율이 15%로 증가함으로 보여줌으로써 코어-쉘-쉘 구조에 있어서 ZnS 쉘에 대한 필요성 및 중요성을 강조하였다.

주요어: 코어-쉘-쉘, 수열적 합성, 나노벨트, 나노레이저, 나노선, 광발광, 양자점, 시간분해 분광학

학 번: 2006-20364

Acknowledgments

184